CRINC

THE UNIVERSITY OF KANSAS CENTER FOR RESEARCH, INC.
2291 Irving Hill Drive-Campus West
Lawrence, Kansas 66045

Theory of Wing Rock

by

Chung-Hao Hsu and C. Edward Lan

Technical Report CRINC-FRL-516-1

February 1984

Flight Research Laboratory
The University of Kansas Center for Research, Inc.
Lawrence, Kansas 66045

Prepared under NASA Grant NAG 1-134

for

Langley Research Center
National Aeronautics and Space Administration

Abstract

A theory is developed for predicting wing-rock characteristics. From available data, it can be concluded that wing rock is triggered by flow asymmetries, developed by negative or weakly positive roll damping, and sustained by nonlinear aerodynamic roll damping. A new nonlinear aerodynamic model that includes all essential aerodynamic nonlinearities is developed. The Beecham-Titchener method is applied to obtain approximate analytic solutions for the amplitude and frequency of the limit cycle based on the three-degree-of-freedom equations of motion. An iterative scheme is developed to calculate the average aerodynamic derivatives and dynamic characteristics at limit-cycle conditions. Good agreement between theoretical and experimental results is obtained.

Table of Contents

Table of Contents (continued)

List of Symbols

Regular Symbols

A	amplitude of the limit-cycle in roll oscillations, deg or rad
AR	wing aspect ratio, b^2/S
a	amplitude of roll oscillations, deg or rad
b	wing span, ft
C_{D_i}	induced drag coefficient
C_L	lift coefficient
C_ℓ	rolling moment coefficient
C_{ℓ_0}	rolling moment coefficient at zero sideslip
$\bar{C}_{\ell_p}$	$C_{\ell_p} + C_{\ell_\beta} \sin \alpha_s$
C_{ℓ_p}	roll damping coefficient based on body-fixed axes
$C_{\ell_{p0}}$	roll damping coefficient at zero sideslip
$C_{\ell_{pp}}$	dimensionless variation of roll damping derivative with roll rate, $\partial C_{\ell_p} / \partial \bar{p}$
$C_{\ell_{p\beta}}$	dimensionless variation of roll damping derivative with sideslip, $\partial C_{\ell_p} / \partial \beta$
$C_{\ell_{p_s}}$	roll damping coefficient based on stability axes
$C_{\ell_{pt}}$	total or effective roll damping coefficient
C_{ℓ_r}	variation of rolling moment coefficient with yaw rate based on body-fixed axes
$C_{\ell_{r_s}}$	variation of rolling moment coefficient with yaw rate based on stability axes
C_{ℓ_β}	variation of rolling moment coefficient with sideslip

$C_{\ell_{\dot{\beta}}}$	variation of rolling moment coefficient with rate of change of sideslip
$C_{\ell_{\delta_A}}$	variation of rolling moment coefficient with aileron angle
$C_{\ell_{\delta_R}}$	variation of rolling moment coefficient with rudder angle
C_m	pitching moment coefficient
C_n	yawing moment coefficient
C_{n_0}	yawing moment coefficient at zero sideslip
C_{n_p}	variation of yawing moment coefficient with roll rate
$C_{n_{p0}}$	variation of yawing moment coefficient with roll rate at zero sideslip
$C_{n_{pp}}$	$\partial C_{n_p} / \partial \bar{p}$
$C_{n_{p\beta}}$	$\partial C_{n_p} / \partial \beta$
C_{n_r}	variation of yawing moment coefficient with yaw rate
C_{n_β}	variation of yawing moment coefficient with sideslip
$C_{n_{\beta_{dyn}}}$	directional departure parameter, $C_{n_\beta} \cos \alpha - \frac{I_{zz}}{I_{xx}} C_{\ell_\beta} \sin \alpha$
$C_{n_{\dot{\beta}}}$	variation of yawing moment coefficient with rate of change of sideslip
$C_{n_{\delta_A}}$	variation of yawing moment coefficient with aileron angle
$C_{n_{\delta_R}}$	variation of yawing moment coefficient with rudder angle
C_Y	side-force coefficient
C_{Y_0}	side-force coefficient at zero sideslip
C_{Y_p}	variation of side-force coefficient with roll rate

C_{Y_r}	variation of side-force coefficient with yaw rate
C_{Y_β}	variation of side-force coefficient with sideslip
$C_{Y_{\delta_A}}$	variation of side-force coefficient with aileron angle
$C_{Y_{\delta_R}}$	variation of side-force coefficient with rudder angle
$\bar{c}$	mean aerodynamic (geometric) chord of a wing, ft
E	energy in roll oscillations, ft-lb
G	amplitude ratio of the β-mode to the ϕ-mode at limit-cycle conditions
g	acceleration of gravity, ft/sec/sec
H	amplitude ratio of the ψ-mode to the ϕ-mode at limit-cycle conditions
$\bar{I}$	$(1 - I_{xz}^2/I_{xx}I_{zz})^{-1}$
I_{xx}, I_{zz}	moments of inertia about the X-axis and Z-axis respectively, slug-ft^2
I_{xy}, I_{xz}, I_{yz}	products of inertia in the XYZ system, slug-ft^2
L_0	$\bar{q}Sb\ C_{\ell_0}/I_{xx}$, sec^{-2}
L_{p0}	$\bar{q}Sb^2C_{\ell_{p0}}/2I_{xx}V$, sec^{-1}
L_{pp}	$\bar{q}Sb^3\ C_{\ell_{pp}}/4\ I_{xx}V^2$, dimensionless
$L_{p\beta}$	$\bar{q}Sb^2\ C_{\ell_{p\beta}}/2I_{xx}V$, sec^{-1}
L_r	$(\bar{q}Sb^2C_{\ell_r}/2I_{xx}V)\cos\alpha_s$, sec^{-1}
L_{δ_A}	$\bar{q}Sb\ C_{\ell_{\delta_A}}/I_{xx}$, sec^{-2}
L_{δ_R}	$\bar{q}Sb\ C_{\ell_{\delta_R}}/I_{xx}$, sec^{-2}
K	system gain of a roll damper (aileron deflection per unit roll rate), deg/rad/sec
k	dimensionless reduced frequency, $\omega b/2V$

M_∞	free-stream Mach number
m	aircraft mass, slug
N_0	$\bar{q}Sb\ C_{n_0}/I_{zz}$, sec^{-2}
N_{p0}	$\bar{q}Sb^2\ C_{n_{p0}}/2I_{zz}V$, sec^{-1}
N_{pp}	$\bar{q}Sb^3C_{n_{pp}}/4\ I_{zz}V^2$, dimensionless
$N_{p\beta}$	$\bar{q}Sb^2\ C_{n_{p\beta}}/2\ I_{zz}V$, sec^{-1}
N_r	$(\bar{q}Sb^2C_{n_r}/2I_{zz}V)\cos\alpha_s$, sec^{-1}
N_β	$\bar{q}Sb\ C_{n_\beta}/I_{zz}$, sec^{-2}
N_{δ_A}	$\bar{q}Sb\ C_{n_{\delta_A}}/I_{zz}$, sec^{-2}
N_{δ_R}	$\bar{q}Sb\ C_{n_{\delta_R}}/I_{zz}$, sec^{-2}
P	period of the limit-cycle in roll oscillations, sec
$\bar{p}$	dimensionless reduced roll rate, pb/2V
p	roll rate about the X-axis, rad/sec
$\bar{q}$	flight dynamic pressure, lb/ft^2
q	pitch rate about the Y-axis, rad/sec
Re	Reynolds number
$\bar{r}$	dimensionless reduced yaw rate, rb/2V
r	yaw rate about the X-axis, rad/sec
S	wing area, ft^2
S_t	area of vertical tail, ft^2
t	time variable, sec
u,v,w	velocity components along X, Y, and Z axes respectively, ft/sec
V	magnitude of flight velocity, ft/sec
X,Y,Z	rectangular coordinates of body system, ft
X_{CG}	moment-center location, ft

Y_0	$\bar{q}S\ C_{Y_0}/mV$, sec^{-1}
Y_p	$\bar{q}Sb\ C_{Y_p}/2mV^2$, dimensionless
Y_r	$\bar{q}Sb\ C_{Y_r}/2mV^2$, dimensionless
Y_β	$\bar{q}S\ C_{Y_\beta}/mV$, sec^{-1}
Y_{δ_A}	$\bar{q}S\ C_{Y_{\delta_A}}/mV$, sec^{-1}
Y_{δ_R}	$\bar{q}S\ C_{Y_{\delta_R}}/mV$, sec^{-1}

Greek Symbols

α	angle of attack, deg or rad
α_{BD}	angle of attack for vortex breakdown at the trailing edge of a wing, deg or rad
α_{Onset}	angle of attack for wing-rock onset, deg or rad
α_s	steady-state angle of attack, deg or rad
β	sidslip angle,deg or rad
β_c	sideslip angle for zero total aerodynamic roll damping, deg or rad
Δ	net difference
δ	phase angle of the ψ mode, deg or rad
δ_A	aileron deflection angle, deg or rad
δ_d	differential tail deflection angle, deg or rad
δ_R	rudder deflection angle, deg or rad
ϵ	phase angle of the β mode, deg or rad
η	amplitude ratio of the ψ mode to the ϕ mode
θ	pitch attitude angle, deg or rad
Λ_{LE}	leading-edge sweep angle, deg or rad
λ	damping of amplitude envelope in roll oscillations, sec^{-1}

ν	argument of a sinusoidal function, deg or rad
ξ	amplitude ratio of the β mode to the ϕ mode
ρ	air density, slug/ft^3
ϕ	bank or Euler roll angle, deg or rad
ϕ_c	bank angle for zero total aerodynamic roll damping, deg or rad
ψ	heading angle, deg or rad
Ω	circular frequency of the limit-cycle in roll oscillations or angular velocity in a rotary test, rad/sec
ω	circular frequency of roll oscillations, rad/sec

Superscripts

$\cdot$	dot, derivative with respect to time
$'$	prime, derivative with respect to amplitude
$-$	bar, dimensional aerodynamic derivatives defined in equation (39)

Acronyms

AFCS	Automatic Flight Control System
DOF	Degree-of-Freedom
SAS	Stability Augmentation System
VORSTAB	a steady-flow aerodynamics computer code for predicting stability derivatives in edge-separated vortex flow

1. Introduction

Modern combat airplanes and tactical missiles have been designed to fly in the regime of high angles of attack to achieve higher maneuverability and a larger flight envelope. Flying at high angles of attack will often produce lateral-directional instabilities such as wing rock, wing drop, nose wander, and nose slice. The main topic here is wing rock.

In this study, a summary based on extensive data is presented to explain the basic mechanisms of wing rock. Nonlinear aerodynamic models for one- and three-degree-of-freedom (DOF) motions are developed to investigate the main aerodynamic nonlinearities causing wing rock. The Beecham-Titchener method (ref. 1) is applied and extended to determine the approximate analytic solutions for the one- and three-DOF equations of motion. Because the interaction between aerodynamics and dynamics of wing rock is strongly nonlinear, an iterative scheme is developed to obtain the average aerodynamic derivatives and limit-cycle characteristics.

2. Wing Rock Phenomenon

Wing rock is an uncommanded roll-yaw oscillation dominated by roll motion oscillating with a constant amplitude (fig. 1). Most flight records show that the amplitude of the limit cycle in roll is at least one order of magnitude higher than that of the oscillation in yaw or pitch (fig. 2). Since wing rock is mainly a result of aerodynamic nonlinearities at high angles of attack, the characteristic motion must be described through a nonlinear mathematical aerodynamic model. However, the response of a lightly damped Dutch roll can be adequately determined by a linear mathematical aerodynamic model. Therefore, both mathematically and physically, wing rock is significantly different from a lightly damped Dutch roll.

The severity of wing rock depends on the amplitude and period of the limit cycle. It may degrade weapon aiming accuracy (ref. 2), missile avoidance capability, and turning effectiveness. It may also cause safety problems during a landing approach or during a dogfight. To improve the air combat performance or handling qualities, the basic mechanisms of wing rock need to be understood.

Wing rock strongly depends on the details of the configuration geometry. It is caused by the intricate flow pattern (ref. 3) at high angles of attack that exists around an aircraft, especially the wing, and is very sensitive to small changes in aircraft geometry. For example, an F-4 when installed with leading edge slats (ref. 4) showed its onset of wing rock deferred to higher angles of attack and the amplitude buildup became much milder and more gradual, in contrast to a

basic configuration. The shark nose and wing-root leading-edge extension (ref. 5) on an F-5 were very effective in suppressing wing rock. As compared with the Gnat aircraft carrying no fuel tanks (fig. 3) those carrying fuel tanks closely under its wings (ref. 6) exhibited wing-rock onset at much higher angles of attack. The early versions of the Harrier (ref. 7) equipped with two close fences on the wing suffered from unacceptable wing rock; but a modified Harrier equipped with two well-spaced fences flew with excellent roll steadiness. Recent wind-tunnel results (fig. 1) disclosed that a delta wing with 80-degree leading-edge sweep (refs. 8 and 9) would indulge in self-excited wing rock. On the other hand, another delta wing with 76-degree leading-edge sweep (ref. 9) did not exhibit such motion at all.

Since the induced increment in angle of attack on a local wing panel varies periodically during wing rock, the flow pattern differs at different instants. For a moderately swept wing, unsteady turbulent boundary layers may alternately separate and reattach on the wing due to unsteady shock movement and boundary layer interaction. For a slender wing, leading-edge vortices may periodically vary their lateral and vertical positions (fig. 4). Furthermore, asymmetric forebody vortices (fig. 5) may interact with the wing in a nonsteady manner. As a result, the pressure field changes cyclically during wing rock. This in turn drives the aircraft to rock back and forth. Hence, the nonlinear interaction between the unsteady flow field and the aircraft motion is extremely important for wing rock.

Success of any attempt to control wing rock depends on the understanding of its dynamic and aerodynamic mechanisms. A unified theory is developed here to interpret the basic mechanisms of wing

rock. After examining a large amount of data, it is concluded that wing rock can be triggered by some asymmetric flow conditions, developed by the loss of roll damping, and sustained primarily by nonlinear roll damping. These are explained in the following.

2.1. Triggering Mechanisms

Wing rock may be initiated either during an asymmetric flight with a finite sideslip or during a zero-sideslip flight with some flow asymmetries over the aircraft.

An airplane in asymmetric flight at high angles of attack, such as uncoordinated turns, asymmetric firing of weapons, and other maneuver situations, is susceptible to the initiation of wing rock. In addition, poor lateral-directional stability and ineffective control power may also trigger wing rock. For example, wing rock may be triggered due to (1) rapid roll-yaw control input for the Gnat aircraft (ref. 10) and the F-5E (ref. 11), (2) zero Dutch roll damping of the Gnat aircraft (ref. 10) and the Handley Page 115 research aircraft (ref. 12), and (3) vanishing dynamic directional departure parameter ($C_{n_{\beta_{dyn}}}$) of the F-4 (refs. 4 and 13) and the F-5 (refs. 5 and 14).

Asymmetric flow occurring at zero-sideslip flight is a particular characteristic of many modern aircraft flying at high angles of attack. The primary causes are asymmetric forebody vortices, viscous flow separation of unswept and moderately swept wings, asymmetric leading-edge vortices of slender wings, and the strong interaction between aircraft aerodynamic components.

At high angles of attack, cross flow dominates for a long pointed nose so that asymmetric leeward vortices or wakes will be randomly shed

and give undesirable side force. Even small manufacturing asymmetries or nose misalignment (refs. 15 and 16) could cause a cross-flow boundary layer to separate unevenly. Such a nonzero side force or moment occurs not only on the fuselage alone but also on complete airplanes, such as a one-tenth scale F-5E complete-airplane wind-tunnel model (ref. 17).

Unsteady shock movement and shock boundary layer interaction could also cause the flow on the upper surface of the outboard section of the wings to separate first for aircraft with low to moderately sweptback wings, such as the F-4 (ref. 18), the F-5 (ref. 19), and the Gnat aircraft (ref. 10). Recent oil-flow studies of a single-engine general aviation research airplane model (ref. 20) clearly pointed out that asymmetric flow separation had progressed from wing-root trailing-edge forward and outboard of the rectangular wing. This resulted in the earlier stall of one wing compared to the other, consequently producing fluctuating pressure changes and yielding a rolling moment.

At high angles of attack, aircraft with highly swept wings can profit from vortex suction lift produced by a pair of strong vortex cores along the upper surface of the wing, if vortex breakdown or vortex-sheet contact does not happen on the wing. Once the vortex breaks down, the vortex pattern is very sensitive to sideslip, resulting in a large change of the rolling moment due to a small sideslip disturbance. There is yet another type of asymmetric vortex pattern without vortex bursting. Vortex sheets from both leading edges of a slender wing may contact each other at zero sideslip (fig. 6) so as to expel reattached flow out of the center area on the upper surface of a wing. Possibly because of hydrodynamic (inviscid) instability (ref. 21) in the vortex flow field, the initially symmetric vortices are trans-

formed into asymmetric vortex patterns such that one vortex slides up over the other to produce asymmetric loads. As sweep angles of delta wings increased from 78 to 84 degrees, induced rolling moment at zero sideslip was shown (ref. 22) to rise from near zero to a very high value. Delta wings with leading-edge sweep angles from 80 to 86.5 degrees (refs. 8, 23, and 24) also experienced some asymmetric vortex structures. Hence, delta wings with sweep angles greater than 78 degrees are prone to having an asymmetric flow field at zero sideslip.

Forebody vortices and shedding vortices from upstream high-lift devices such as strakes and canards will heavily affect the flow over the wing and tail. Nonzero side forces or moments due to the strong interaction between aircraft aerodynamic components are evident on the F-5 (refs. 11 and 14) and other configurations. Analysis of wing rock for these configurations should account for the whole aircraft rather than the wing alone.

2.2. Transient Development

Once asymmetric flow starts, a roll-oscillation amplitude will keep building up if the roll damping is weak or negative. For example, an F-4 encountered severe wing rock in flight (ref. 25). Wind-tunnel force-oscillation tests (ref. 26) later confirmed that the negative roll damping at small amplitude near the stall angle of attack was responsible for transient wing rock. Other configurations such as the Gnat aircraft (ref. 6), the F-5 (refs. 5 and 14), the F-14 (ref. 27), a recently proposed fighter configuration (ref. 2), a single-engine general aviation research aircraft (ref. 20), the X-29A forward-swept wing fighter (ref. 28), a series of flying wings with vertical tails

(ref. 29), and a delta wing of 80-degree sweep (ref. 8), all attributed wing rock development to the destablizing roll damping at high angles of attack. For the delta wing with 80-degree sweep, the asymmetric vortex pattern (fig. 4) became more pronounced when the wing rolled. The windward vortex appeared to diffuse and shift inboard while the leeward vortex remained strong and moved outboard, resulting in a propelling rolling moment at a small roll angle. The transient wing rock due to roll instability at low roll amplitude will grow gradually over some oscillation cycles. The decisive factor in developing transient wing rock is the loss of roll damping at low oscillation amplitude where the dihedral effect is almost powerless to counteract.

2.3. Sustaining of Limit Cycles

At high angles of attack, the magnitude and sign of roll damping derivatives may vary with oscillation amplitude, frequency and roll rate. Several sets of wind-tunnel data, including the F-4 (ref. 26), the F-5 (ref. 5), a recently proposed fighter configuration (ref. 2), and a delta wing with 80-degree sweep (ref. 8), showed that effective roll damping was negative at small roll amplitude but positive at large roll amplitude (fig. 7). For a delta wing with 80-degree sweep, one reason was that an asymmetric vortex pattern (fig. 4) at large sideslip during rolling would yield positive roll damping, because the leeward vortex was displaced above and finally off the wing. Force-oscillation tests of this delta wing showed only little dependency of roll damping on oscillation frequency. However, they were conducted at frequencies well below wing-rock frequencies observed in free-to-roll tests (fig. 8). On the other hand, the roll damping of the F-4 (refs. 26

and 30) deteriorated quickly as the oscillation frequency was reduced. Cubic variation of the rolling moment with roll rate seemed to correlate well with wing rock for the Gnat trainer (refs. 6 and 10). This implied that the roll damping was a function of roll rate. Other data showing nonlinear dependency of the rolling moment on roll rate in rotary tests (refs. 2, 3, and 8) also implied that the roll damping was a function of roll rate (fig. 9). Thus, nonlinear roll damping depending on amplitude, frequency, and roll rate probably plays the leading role in sustaining the limit cycle of wing rock.

From the viewpoint of basic fluid mechanics, the nonlinear roll damping probably results from various vortex asymmetries and time lags associated with the time history of fluid and induced mainly by the fluid viscosity. Convective lag is well known to exist because shedding vortices convect downstream at a finite speed equal to the local free-stream velocity and disturbances created at any point propagate at the local speed of sound. Because the vortex flow over a wing can not reach its steady-state strength and position at once in plunging motion (ref. 31), the so-called vortex lag is created. During a plunging motion, pressure changes on a wing for increasing angles of attack are not simply reversed when angles of attack are decreasing. It was theoretically demonstrated (ref. 32) that vortex lag would depend on motion frequency and create a phase lag between the wing motion and its leading-edge vortex strength buildup. Development of a turbulent boundary layer and wake must account for the infuence of upstream flow history on turbulent stresses (ref. 33). Since a finite time is required to establish or destroy a healthy flow, a time lag in separation or reattachment was recorded during a boundary-layer wind-

tunnel test (ref. 34). This test revealed that time lag seemed to be larger in reattachment than in separation under conditions of cyclically varying pressure gradient.

Though the roll damping is negative or weak over small oscillation amplitudes, it is positive at larger amplitudes for a sustained wing rock. Both the effective dihedral effect and positive roll damping (fig. 7) via aerodynamic nonlinearities at large roll amplitudes will gradually reduce the roll rate. As restoring moments become stronger, the aircraft will reach a threshold amplitude and finally reverse the rolling direction. Thus, wing rock is constrained to a finite amplitude through nonlinear roll damping.

3. Theoretical Development

The main difficulty in describing the relationship between instantaneous aerodynamic reactions and dynamic motion variables of an aircraft lies in the fact that this relationship is not solely determined by instantaneous values of motion variables but also determined by the time history of the motion up to the instant in question. A straightforward approach is to solve the unsteady flow-field equations simultaneously with the equations of motion of the aircraft. However, to avoid the need for solving both dynamic and aerodynamic equations at the same time, a proper aerodynamic model relating aerodynamic reactions and motion variables must be developed.

Currently, there are several aerodynamic models proposed to describe wing rocking. Besides some disadvantages, each of them is verified only for a particular configuration.

First, it was shown that by including a cubic term in the roll damping derivative of a Gnat aircraft (ref. 6), the angle of sideslip during wing rock could be fairly well predicted by reducing the three-DOF lateral-directional equations of motion to a fourth-order differential equation in β and by obtaining solutions from the application of the Beecham-Titchener method (ref. 1). When similar cubic terms were introduced in the static yawing moment derivative due to sideslip for the HP 115 research aircraft (refs. 12 and 35), the estimated amplitudes of limit cycles were about 40 percent greater than those obtained from six-DOF nonlinear simulations. However, using the nonlinear stiffness alone in a one-DOF model can not explain the existence of wing rock.

Second, nonzero static lateral-directional aerodynamic forces and moments at zero sideslip angle, together with aerodynamic hysteresis were used to reproduce the wing rock of an F-5E in a six-DOF digital computer simulation (ref. 11). The aerodynamic hysteresis of the rolling moment with sideslip was also assumed in a simple two-DOF model including rolling and yawing moments to demonstrate that roll hysteresis could be a potential cause of wing rock (ref. 36). Mathematically, such hysteresis (fig. 10) can be accounted for by including a function which can assign two possible values in the rolling moment for a given sideslip angle. A single-DOF model with a hysteresis loop is possible to yield the motion of wing rock. However, limit cycles are obtained only when an external disturbance is large enough to induce a sideslip angle to lie outside of the β-range in the hysteresis loop. Furtherore, the loop shape must be determined before solving the equation of motion.

Third, the variation of roll damping with sideslip angle (fig. 11a) such that damping was negative at small sideslip angles but positive at large sideslip angles could induce wing rock for a delta wing with 80-degree sweep (ref. 8). A one-DOF nonlinear simulation for this delta wing produced the motion of wing rock in close agreement with test results of a free-to-roll model. However, it was also shown that an approximate analytical solution of the one-DOF equation based on the Beecham-Titchener method by assuming a linear variation of roll damping with sideslip angle underestimated the amplitudes of wing rock by 15 percent for angles of attack between 25 and 35 degrees. Figure 11b indicated that in contrast to no hysteresis for static-force-test data, dynamic hysteresis was recorded during free-to-roll tests.

Fourth, by representing the time history effect by a lumped time lag (ref. 37), limit-cycle amplitudes were predicted by use of experimental static data (fig. 12). However, this one-DOF analysis could only predict the limit-cycle amplitude for delta wings with leading-edge sweep larger than 74°. Besides, the frequency must be known in advance.

Finally, the unsteady incompressible inviscid flow equations and the one-DOF equation of motion were simultaneously solved in reference 38. It resulted in dynamic hysteresis of rolling moment versus bank angles (fig. 13). However, it failed to predict the maximum limit-cycle amplitude for an 80-degree delta wing because the vortex breakdown effects were not taken into account. Further, this method could not provide any aerodynamic derivatives causing wing rock. In addition to some numerical simulation problems, it is very time-consuming.

To describe the wing-rock characteristics of any aircraft, the aerodynamic model developed here will be more general to include all the essential aerodynamic nonlinearities presented in the aforementioned current aerodynamic models. In the meantime, the nonlinear roll damping depending on amplitude, frequency, and roll rate may be a primary factor in sustaining wing rock and should be accounted for properly.

Since wing rock is dominated by the roll oscillation, three-DOF lateral-directional equations of motion will be used in the present investigation, instead of the general six-DOF equations of motion.

Accurate solutions can be achieved through numerical integrations. However, purely numerical solutions do not provide direct physical insight into the dynamic mechanisms of wing rock. A useful analytic approximation to the characteristic motion of wing rock is more suitable

for a parametric study of aerodynamic and dynamic causes. The Beecham-Titchener method (ref. 1) will be applied and extended here for this purpose.

3.1. One-Degree-of-Freedom Model

A one-DOF rolling equation is to be studied first to describe the idea. By ignoring any pitching or yawing effects, the principal motion variable in pure rolling motion is the Euler roll angle, ϕ. Flight path properties such as flight velocity, altitude, Mach number, Reynolds number,and mass distribution are all assumed to remain constant throughout the motion. Effects of elastic, gravitational, and propulsive forces are all excluded. For a rigid aircraft with the observer fixed in the geometric body-axis system (fig. 14) whose origin is at the aircraft center of mass, the equation of motion is given by

$$\frac{I_{xx}}{\bar{q}\ S\ b}\dot{p} = C_{\ell}\ (t) \tag{1}$$

where I_{xx} is the rolling moment of inertia, $\bar{q}$ is the dynamic pressure, S is the reference wing area, b is the wing span, t is the time variable, $\dot{p}$ is the angular acceleration about the longitudinal axis, and $C_{\ell}(t)$ is the total aerodynamic rolling moment coefficient. Equation (1) simply states that the inertial rolling moment is balanced by the time-dependent aerodynamic rolling moment. Since classical stability derivatives in Taylor series expansions alone are not adequate to account for the aerodynamic nonlinearities at high angles of attack, the concept of a simplified nonlinear functional (ref. 39) is used to describe the total aerodynamic rolling moment.

After examining the wind-tunnel data of a flat-plate delta wing with 80-degree sweep (ref. 8) subjected to static-force, forced-oscillation, rotary, and free-to-roll tests, the characteristic variables of $C_\ell(t)$ are selected to be α_s (the steady-state angle of attack), β (sideslip angle), $\bar{p}$ (the reduced rolling velocity about the X-axis), and δ_A (aileron deflection). Hence, the total aerodynamic rolling moment coefficient at fixed α_s can be expressed in the form of a functional as

$$C_\ell(t) = C_\ell(\alpha_s, \beta(t), \bar{p}(t), \delta_A(t)) \tag{2}$$

Practically, the functional will be replaced by a multivariable function which depends on a few characteristic parameters rather than on continuous functions. Furthermore, the multivariable function will be expanded into a form of component buildup as

$$C_\ell(t) = C_{\ell_0} + C_{\ell_\beta}\beta + C_{\ell_{pt}}\bar{p} + C_{\ell_{\delta_A}}\delta_A \tag{3}$$

where

$$C_{\ell_{pt}} = C_{\ell_{p0}} + C_{\ell_{p\beta}}|\beta| + C_{\ell_{pp}}|\bar{p}| \tag{4}$$

The total aerodynamic rolling moment coefficient in equation (3) is composed of (1) $C_{\ell_0}(\alpha_s, \beta = 0)$, the aerodynamic rolling moment coefficient arising from asymmetric flow at zero sideslip angle, being highly dependent on aircraft configurations; (2) $C_{\ell_\beta}(\alpha_s, \beta)$, the dihedral effect, being usually negative (statically stable), but possibly positive (statically unstable) for some configurations (refs. 40 and 41) at high angles of attack; (3) $C_{\ell_{pt}}(\alpha_s, \beta, \bar{p})$, the total or

effective aerodynamic roll damping coefficient, being a strong nonlinear function of α_s, β, and $\bar{p}$; and (4) $C_{\ell_{\delta_A}}(\alpha_s, \bar{\beta}, p, \delta_A)$, the aerodynamic roll derivative due to aileron deflection.

Equation (4) represents the present proposed aerodynamic model to describe the aforementioned aerodynamic nonlinearities. This expression is expected to give negative roll damping for small roll amplitudes and positive roll damping for large amplitudes in accord with experimental data. If C_{ℓ_p} is plotted against β or $\bar{p}$, the resulting curve is assumed to be symmetric with respect to $\beta = 0$ or $\bar{p} = 0$ respectively. The absolute signs in equation (4) will cause the values of $C_{\ell_{pt}}$ at different instants to be the same if $|\beta|$ or $|\bar{p}|$ have the same values at the corresponding instants in a limit-cycle oscillation. At a fixed β, C_ℓ may have two values if the sign of $\bar{p}$ is different. Furthermore, at a fixed $\bar{p}$, C_ℓ may also have two values if the sign of β is different. Thus, β- and $\bar{p}$-dependent roll damping is able to produce discontinuous and double-value rolling moments with respect to β or $\bar{p}$. In other words, it may result in a hysteresis loop of rolling moment with respect to β due to the cyclical change of total roll damping.

Equation (1) together with the kinematic relationships

$$p = \dot{\phi} \tag{5}$$

$$\beta = \sin^{-1}(\sin \alpha_s \sin \phi) \tag{6}$$

form a nonlinear second-order differential equiation in ϕ, with coefficients being also functions of time. To simplify equation (3), equation (6) is approximated by

$$\beta \cong \phi \sin \alpha_s \tag{7}$$

This is a good approximation, because β of equation (7) is about 1 degree higher than β of equation (6) for most cases of wing rock. Substituting equations (3), (4), (5), and (7) into (1) yields

$$\frac{I_{xx}}{\bar{q}Sb}\ddot{\phi} = C_{\ell_0} + C_{\ell_{\delta_A}}\delta_A + \sin\alpha_s\, C_{\ell_\beta}\,\phi + \left(C_{\ell_{p0}} + \sin\alpha_s\, C_{\ell_{p\beta}}\,|\phi| + C_{\ell_{pp}}\,|\frac{\dot{\phi}b}{2V}|\right)\frac{\dot{\phi}b}{2V} \tag{8}$$

For convenience, equation (8) is rewritten in terms of dimensional derivatives as

$$\ddot{\phi} = L_0 + L_{\delta_A}\delta_A + \sin\alpha_s L_\beta\,\phi + \left(L_{p0} + \sin\alpha_s\, L_{p\beta}\,|\phi| + L_{pp}\,|\dot{\phi}|\right)\dot{\phi} \tag{9}$$

where dimensional derivatives are defined by:

$$L_0 = \frac{\bar{q}\,S\,b}{I_{xx}}C_{\ell_0}\ (\sec^{-2}) \qquad L_{\delta_A} = \frac{\bar{q}\,S\,b}{I_{xx}}C_{\ell_{\delta_A}}\ (\sec^{-2})$$

$$L_\beta = \frac{\bar{q}\,S\,b}{I_{xx}}C_{\ell_\beta}\ (\sec^{-2}) \qquad L_{p0} = \frac{\bar{q}\,S\,b^2}{2\,V\,I_{xx}}C_{\ell_{p0}}\ (\sec^{-1}) \tag{10}$$

$$L_{p\beta} = \frac{\bar{q}\,S\,b^2}{2\,V\,I_{xx}}C_{\ell_{p\beta}}\ (\sec^{-1}) \qquad L_{pp} = \frac{\bar{q}\,S\,b^3}{4\,V^2\,I_{xx}}C_{\ell_{pp}}\ (\text{dimensionless})$$

Equation (9) is the nonlinear equation of motion to be solved for the one-DOF model.

3.2. Approximate Analytic Solutions of the One-Degree-of-Freedom Model

To solve equation (9) so that the amplitudes and periods of wing rock can be determined, the Beecham-Titchener method (ref. 1) appears to be the most appropriate. This method is basically an extension of the classical Krylov-Bogoliubov method. It is shown to be a combination of the averaging principle and the method of variation of parameters (ref. 42). For a damped linear system (ref. 1), the first-order approximation of the Beecham-Titchener method gives the exact solution. For such a system, the Krylov-Bogoliubov method yields an incorrect undamped natural frequency. Other examples (ref. 1) involving nonlinear terms are solved with excellent accuracy by using the Beecham-Titchener method. This method is also capable of obtaining the higher-order approximations. Therefore, this method is applied here to obtain an approximate analytic solution to equation (9).

By analogy with the solution for a linear second-order differential equation, the time-dependent solution of equation (9) is assumed to be

$$\phi(t) = a(t) \cos \nu(t) \tag{11}$$

That is, a product of an amplitude function $a(t)$ and a sinusoidal function in terms of an argument $\nu(t)$ is assumed. Both ω and λ are defined in such a way that

$$\omega = \dot{\nu} \tag{12}$$

$$\lambda = \dot{a}/a \tag{13}$$

To the first-order approximation (appendix A), equation (9) without control deflection is reduced to

$$\lambda^2 - \omega^2 = \sin \alpha_s \, L_\beta + \lambda L_{p0} + \frac{8}{3\pi} a\lambda \sin \alpha_s \, L_{p\beta} + \frac{8}{3\pi} a \, \lambda \, \omega \, L_{pp} \tag{14}$$

$$2\lambda\omega = \omega \, L_{p0} + \frac{4}{3\pi} a \, \omega \sin \alpha_s \, L_{p\beta} + \frac{4}{3\pi} a \, (\lambda^2 + 2\omega^2) \, L_{pp} \tag{15}$$

Equation (9), a formidable nonlinear second-order differential equation, is thus reduced to two coupled nonlinear first-order differential equations. Both λ and ω turn out to be functions of the amplitude. Equations (14) and (15) can be further integrated by a numerical technique. All the aerodynamic derivatives in equations (14) and (15) should be evaluated at some average conditions according to the Beecham-Titchener method.

If Ω, P, and A are the circular frequency, the period, and the amplitude respectively for a steady-state limit-cycle wing rock, then they can be obtained by setting λ to zero in equations (14) and (15). The closed-form solutions can be shown (appendix A) to be

$$\begin{aligned} \Omega &= (-\sin \alpha_s \, L_\beta)^{1/2} \\ &= \left(-\frac{\bar{q} \, S \, b}{I_{xx}} \sin \alpha_s \, C_{\ell_\beta}\right)^{1/2} \end{aligned} \tag{16}$$

$$P = \frac{2\pi}{\Omega} \tag{17}$$

$$A = -\frac{3\pi}{4} \frac{L_{p0}}{\sin \alpha_s L_{p\beta} + 2 \Omega L_{pp}} = -\frac{3\pi}{4} \frac{C_{\ell_{p0}}}{\sin \alpha_s C_{\ell_{p\beta}} + \frac{\Omega b}{V} C_{\ell_{pp}}} \tag{18}$$

They must be real and positive to be physically realistic. As can be seen from equations (16) and (17), other than inertial properties, the limit-cycle period depends only on C_{ℓ_β}. The limit-cycle amplitude is a function of $C_{\ell_{p0}}$, $C_{\ell_{p\beta}}$, and $C_{\ell_{pp}}$. Equation (18) can be reduced to the expression used in reference 8 if $C_{\ell_{pp}}$ is ignored.

3.3. Three-Degree-of-Freedom Model

To obtain a better understanding of wing rock, a three-DOF model will be developed. Since the angle of attack for a sustained wing rock remains essentially constant, the effects of the longitudinal mode on lateral-directional modes can be neglected in the theoretical analysis.

Most aircraft are symmetric with reference to a vertical plane (X-Z plane) aligned with the longitudinal axis (X-axis) so that $I_{xy} = 0$ and $I_{yz} = 0$ are satisfied. If inertial coupling moments associated with pq or qr are ignored, the equations of motion for three-DOF lateral-directional modes (ref. 43), based on body-fixed axes, are

$$\frac{m}{\bar{q}S}(\dot{v} - wp + ur - g \sin \phi \cos \theta) = C_Y(t) \tag{19}$$

$$\frac{I_{xx}}{\bar{q}Sb} \dot{p} - \frac{I_{xz}}{\bar{q}Sb} \dot{r} = C_\ell(t) \tag{20}$$

$$\frac{I_{zz}}{\bar{q}Sb}\dot{r} - \frac{I_{xz}}{\bar{q}Sb}\dot{p} = C_n(t) \tag{21}$$

where m is the airplane mass and g is the acceleration of gravity; u, v, and w are velocity components along X, Y, and Z axis; p and r are roll and yaw rates about X and Z axes respectively; θ is the pitch attitude angle; C_Y and C_n are the total aerodynamic side-force and yawing moment coefficients respectively. $C_Y(t)$, $C_\ell(t)$, and $C_n(t)$ can be written in forms of functional as

$$C_Y(t) = C_Y\ (\alpha_s,\ \beta(t),\ \bar{p}(t),\ \bar{r}(t),\ \delta_A(t),\ \delta_R(t)) \tag{22}$$

$$C_\ell(t) = C_\ell\ (\alpha_s,\ \beta(t),\ \bar{p}(t),\ \bar{r}(t),\ \delta_A(t),\ \delta_R(t)) \tag{23}$$

$$C_n(t) = C_n\ (\alpha_s,\ \beta(t),\ \bar{p}(t),\ \bar{r}(t),\ \delta_A(t),\ \delta_R(t)) \tag{24}$$

where $\bar{r}$ is the reduced yaw rate and δ_R is the rudder deflection angle. Similar to the one-DOF analysis, $C_Y(t)$, $C_\ell(t)$, and $C_n(t)$ are further expanded into forms of component buildup as

$$C_Y(t) = C_{Y_0} + C_{Y_\beta}\beta + C_{Y_p}\bar{p} + C_{Y_r}\bar{r} + C_{Y_{\delta_A}}\delta_A + C_{Y_{\delta_R}}\delta_R \tag{25}$$

$$C_\ell(t) = C_{\ell_0} + C_{\ell_\beta}\beta + (C_{\ell_{p0}} + C_{\ell_{p\beta}}|\beta| + C_{\ell_{pp}}|\bar{p}|)\bar{p} + C_{\ell_r}\bar{r} + C_{\ell_{\delta_A}}\delta_A + C_{\ell_{\delta_R}}\delta_R \tag{26}$$

$$C_n(t) = C_{n_0} + C_{n_\beta}\beta + (C_{n_{p0}} + C_{n_{p\beta}}|\beta| + C_{n_{pp}}|\bar{p}|)\bar{p} + C_{n_r}\bar{r} + C_{n_{\delta_A}}\delta_A + C_{n_{\delta_R}}\delta_R \tag{27}$$

Because the motion of wing rock is primarily rolling around the longitudinal body axis, the total aerodynamic yawing moment due to roll rate in equation (27) is expected to be as important as the total aerodynamic rolling moment due to roll rate in equation (26). Both roll and yaw damping terms associated with sideslip and roll rate are thus assumed to have similar forms.

To simplify the equations of motion, the following approximations are applied.

$$\begin{aligned} \sin\phi &\approx \phi \\ \cos\phi &\approx 1 \\ u/V &\approx \cos\alpha_s \\ v/V &\approx \beta \\ w/V &\approx \sin\alpha_s \end{aligned} \tag{28}$$

Equations (25) - (27) are now rewritten as

$$\dot{\beta} - p\sin\alpha_s + r\cos\alpha_s - \frac{g}{V}\phi\cos\theta = \frac{\bar{q}S}{mV}\left(C_{Y_0} + C_{Y_\beta}\beta + C_{Y_p}\bar{p} + C_{Y_r}\bar{r} + C_{Y_{\delta_A}}\delta_A + C_{Y_{\delta_R}}\delta_R\right) \tag{29}$$

$$\dot{p} - \frac{I_{xz}}{I_{xx}}\dot{r} = \frac{\bar{q}Sb}{I_{xx}}\left[C_{\ell_0} + C_{\ell_\beta}\beta + \left(C_{\ell_{p0}} + C_{\ell_{p\beta}}|\beta| + C_{\ell_{pp}}|\bar{p}|\right)\bar{p} + C_{\ell_r}\bar{r} + C_{\ell_{\delta_A}}\delta_A + C_{\ell_{\delta_R}}\delta_R\right] \tag{30}$$

$$\dot{r} - \frac{I_{xz}}{I_{zz}}\dot{p} = \frac{\bar{q}Sb}{I_{zz}}\left[C_{n_0} + C_{n_\beta}\beta + \left(C_{n_{p0}} + C_{n_{p\beta}}|\beta| + C_{n_{pp}}|\bar{p}|\right)\bar{p} + C_{n_r}\bar{r} + C_{n_{\delta_A}}\delta_A + C_{n_{\delta_R}}\delta_R\right] \tag{31}$$

Rewriting equations (29), (30), and (31) in terms of dimensional derivatives yields

$$\dot{\beta} - p \sin \alpha_s + r \cos \alpha_s - \frac{g}{V} \phi \cos \theta = Y_0 + Y_\beta \beta + Y_p p + Y_r r + Y_{\delta_A} \delta_A + Y_{\delta_R} \delta_R \quad (32)$$

$$\dot{p} - \frac{I_{xz}}{I_{xx}} \dot{r} = L_0 + L_\beta \beta + (L_{p0} + L_{p\beta} |\beta| + L_{pp} |p|)\, p + \frac{L_r r}{\cos \alpha_s} + L_{\delta_A} \delta_A + L_{\delta_R} \delta_R \quad (33)$$

$$\dot{r} - \frac{I_{xz}}{I_{zz}} \dot{p} = N_0 + N_\beta \beta + (N_{p0} + N_{p\beta} |\beta| + N_{pp} |p|) p + \frac{N_r r}{\cos \alpha_s} + N_{\delta_A} \delta_A + N_{\delta_R} \delta_R \quad (34)$$

where

$$Y_0 = \frac{\bar{q}S}{mV} C_{Y_0} \ (\sec^{-1}) \qquad Y_\beta = \frac{\bar{q}S}{mV} C_{Y\beta} \ (\sec^{-1})$$

$$Y_p = \frac{\bar{q}Sb}{2mV^2} C_{Y_p} \ \text{(dimensionless)} \qquad Y_r = \frac{\bar{q}Sb}{2mV^2} C_{Y_r} \ \text{(dimensionless)}$$

$$Y_{\delta_A} = \frac{\bar{q}S}{mV} C_{Y_{\delta_A}} \ (\sec^{-1}) \qquad Y_{\delta_R} = \frac{\bar{q}S}{mV} C_{Y_{\delta_R}} \ (\sec^{-1})$$

$$L_0 = \frac{\bar{q}Sb}{I_{xx}} C_{\ell_0} \ (\sec^{-2}) \qquad L_\beta = \frac{\bar{q}Sb}{I_{xx}} C_{\ell_\beta} \ (\sec^{-2})$$

$$L_{p0} = \frac{\bar{q}Sb^2}{2I_{xx}V} C_{\ell_{p0}} \ (\sec^{-1}) \qquad L_{p\beta} = \frac{\bar{q}Sb^2}{2I_{xx}V} C_{\ell_{p\beta}} \ (\sec^{-1}) \quad (35)$$

$$L_{pp} = \frac{\bar{q}Sb^3}{4I_{xx}V^2} C_{\ell_{pp}} \ \text{(dimensionless)} \qquad L_r = \frac{\bar{q}Sb^2}{2I_{xx}V} C_{\ell_r} \cos\alpha_s, (\sec^{-1})$$

$$L_{\delta_A} = \frac{\bar{q}Sb}{I_{xx}} C_{\ell_{\delta_A}} \ (\sec^{-2}) \qquad L_{\delta_R} = \frac{\bar{q}Sb}{I_{xx}} C_{\ell_{\delta_R}} \ (\sec^{-2})$$

$$N_0 = \frac{\bar{q}Sb}{I_{zz}} C_{n_0} \ (\sec^{-2}) \qquad N_\beta = \frac{\bar{q}Sb}{I_{zz}} C_{n_\beta} \ (\sec^{-2})$$

$$N_{p0} = \frac{\bar{q}Sb^2}{2I_{zz}V} C_{n_{p0}} \quad (\sec^{-1}) \qquad N_{p\beta} = \frac{\bar{q}Sb^2}{2I_{zz}V} C_{n_{p\beta}} \quad (\sec^{-1})$$

$$N_{pp} = \frac{\bar{q}Sb^3}{4I_{zz}V^2} C_{n_{pp}} \quad (\text{dimensionless}) \qquad N_r = \frac{\bar{q}Sb^2}{2I_{zz}V} C_{n_r} \cos \alpha_s \quad (\sec^{-1})$$

$$N_{\delta_A} = \frac{\bar{q}Sb}{I_{zz}} C_{n_{\delta_A}} \quad (\sec^{-2}) \qquad N_{\delta_R} = \frac{\bar{q}Sb}{I_{zz}} C_{n_{\delta_R}} \quad (\sec^{-2})$$

The equations of motion for the three-DOF model are finally obtained by rearranging equations (32) - (34) as

$$\dot{\beta} = \bar{Y}_0 + \bar{Y}_\beta \beta + \bar{Y}_p p + \bar{Y}_r r + \bar{Y}_\phi \phi + \bar{Y}_{\delta_A} \delta_A + \bar{Y}_{\delta_R} \delta_R \tag{36}$$

$$\dot{p} = \bar{L}_0 + \bar{L}_\beta \beta + (\bar{L}_{p0} + \bar{L}_{p\beta}|\beta| + \bar{L}_{pp}|p|)\, p + \frac{\bar{L}_r r}{\cos\alpha_s} + \bar{L}_{\delta_A} \delta_A + \bar{L}_{\delta_R} \delta_R \tag{37}$$

$$\dot{r} = \bar{N}_0 + \bar{N}_\beta \beta + (\bar{N}_{p0} + \bar{N}_{p\beta}|\beta| + \bar{N}_{pp}|p|)\, p + \frac{\bar{N}_r r}{\cos\alpha_s} + \bar{N}_{\delta_A} \delta_A + \bar{N}_{\delta_R} \delta_R \tag{38}$$

where

$$\bar{Y}_0 = Y_0 \qquad \bar{Y}_\beta = Y_\beta$$

$$\bar{Y}_p = Y_p + \sin \alpha_s \qquad \bar{Y}_r = (Y_r - \cos \alpha_s)\cos\alpha_s$$

$$\bar{Y}_\phi = \frac{g}{V} \cos \theta \qquad \bar{Y}_{\delta_A} = Y_{\delta_A}$$

$$\bar{Y}_{\delta_R} = Y_{\delta_R} \qquad \bar{I} = \left(1 - \frac{I_{xz}^2}{I_{xx}I_{zz}}\right)^{-1}$$

$$\bar{L}_0 = \bar{I}(L_0 + \frac{I_{xz}}{I_{xx}} N_0)$$

$$\bar{L}_{p0} = \bar{I}(L_{p0} + \frac{I_{xz}}{I_{xx}} N_{p0})$$

$$\bar{L}_{pp} = \bar{I}(L_{pp} + \frac{I_{xz}}{I_{xx}} N_{pp})$$

$$\bar{L}_{\delta_A} = \bar{I}(L_{\delta_A} + \frac{I_{xz}}{I_{xx}} N_{\delta_A})$$

$$\bar{N}_0 = \bar{I}(\frac{I_{xz}}{I_{zz}} L_0 + N_0)/\cos \alpha_s$$

$$\bar{N}_{p0} = \bar{I}(\frac{I_{xz}}{I_{zz}} L_{p0} + N_{p0})/\cos \alpha_s$$

$$\bar{N}_{pp} = \bar{I}(\frac{I_{xz}}{I_{zz}} L_{pp} + N_{pp})/\cos \alpha_s$$

$$\bar{N}_{\delta_A} = \bar{I}(\frac{I_{xz}}{I_{zz}} L_{\delta_A} + N_{\delta_A})$$

$$\bar{L}_\beta = \bar{I}(L_\beta + \frac{I_{xz}}{I_{xx}} N_\beta)$$

$$\bar{L}_{p\beta} = \bar{I}(L_{p\beta} + \frac{I_{xz}}{I_{xx}} N_{p\beta}) \qquad (39)$$

$$\bar{L}_r = \bar{I}(L_r + \frac{I_{xz}}{I_{xx}} N_r)$$

$$\bar{L}_{\delta_R} = \bar{I}(L_{\delta_R} + \frac{I_{xz}}{I_{xx}} N_{\delta_R})$$

$$\bar{N}_\beta = \bar{I}(\frac{I_{xz}}{I_{zz}} L_\beta + N_\beta)/\cos \alpha_s$$

$$\bar{N}_{p\beta} = \bar{I}(\frac{I_{xz}}{I_{zz}} L_{p\beta} + N_{p\beta})/\cos \alpha_s$$

$$\bar{N}_r = \bar{I}(\frac{I_{xz}}{I_{zz}} L_r + N_r)/\cos \alpha_s$$

$$\bar{N}_{\delta_R} = \bar{I}(\frac{I_{xz}}{I_{zz}} L_{\delta_R} + N_{\delta_R})$$

p and r are defined as

$$p \cong \dot{\phi}$$

and

$$r \cong \dot{\psi} \cos \alpha_s \qquad (40)$$

This is equivalent to assuming that $\dot{\psi}$ is small compared with $\dot{\phi}$ in the roll rate equation and $\dot{\theta}$ is negligible in the yaw rate equation (ref. 43). (41)

3.4. Approximate Analytic Solutions of the Three-Degree-of-Freedom Model

The Beecham-Titchener method was originally developed for a single nonlinear second-order differential equation only. This method will be extended here for the three-DOF equations of motion to obtain the approximate analytic solutions for wing rock. The solutions to equations (36) - (38) are assumed to be

$$\beta(t) = a(t)\, \xi\, (t) \cos\, [\nu(t) + \varepsilon(t)] \tag{42}$$

$$\phi(t) = a(t) \cos\, \nu(t) \tag{43}$$

$$\psi(t) = a(t)\, \eta(t) \cos\, [\nu(t) + \delta(t)] \tag{44}$$

where ξ and η are the instantaneous amplitude ratios of β and ψ modes to the ϕ mode and ε and δ are the phase angles of β and ψ modes with respect to the ϕ mode.

To the first-order approximation (appendix B), equations (36) - (38) without control deflections can be shown to be

$$\xi(\lambda\cos\varepsilon - \omega\sin\varepsilon) = \bar{Y}_\beta\, \xi\cos\varepsilon + \bar{Y}_p\lambda + \bar{Y}_r\eta\, (\lambda\cos\delta - \omega\sin\delta) + \bar{Y}_\phi \tag{45}$$

$$\xi(\lambda\sin\varepsilon + \omega\cos\varepsilon) = \bar{Y}_\beta\, \xi\sin\varepsilon + \bar{Y}_p\omega + \bar{Y}_r\eta\, (\lambda\sin\delta + \omega\cos\delta) \tag{46}$$

$$\lambda^2 - \omega^2 = \bar{L}_\beta\, \xi\cos\varepsilon + \bar{L}_{p0}\lambda + \frac{8}{3\pi}\bar{L}_{p\beta}\, a\xi\lambda + \frac{8}{3\pi}\bar{L}_{pp}\, a\lambda\omega$$

$$+ \bar{L}_r\eta\, (\lambda\cos\delta - \omega\sin\delta) \tag{47}$$

$$2\lambda\omega = \bar{L}_\beta\ \xi\sin\varepsilon + \bar{L}_{p0}\omega + \frac{4}{3\pi}\bar{L}_{p\beta}\ a\xi\omega + \frac{4}{3\pi}\bar{L}_{pp}\ a(\lambda^2 + 2\omega^2)$$

$$+ \bar{L}_r\eta\ (\lambda\sin\delta + \omega\cos\delta) \tag{48}$$

$$\eta[(\lambda^2-\omega^2)\ \cos\ \delta\ -\ 2\lambda\omega\sin\delta] = \bar{N}_\beta\ \xi\cos\varepsilon + \bar{N}_{p0}\lambda + \frac{8}{3\pi}\bar{N}_{p\beta}\ a\xi\lambda$$

$$+ \frac{8}{3\pi}\bar{N}_{pp}\ a\lambda\omega + \bar{N}_r\eta(\lambda\cos\delta - \omega\sin\delta) \tag{49}$$

$$\eta[(\lambda^2 - \omega^2)\ \sin\delta + 2\lambda\omega\cos\delta] = \bar{N}_\beta\ \xi\sin\varepsilon + \bar{N}_{p0}\omega + \frac{4}{3\pi}\bar{N}_{p\beta}\ a\xi\omega$$

$$+ \frac{4}{3\pi}\bar{N}_{pp}\ a(\lambda^2 + 2\omega^2) + \bar{N}_r\eta\ (\lambda\sin\delta + \omega\cos\delta) \tag{50}$$

Again, all the aerodynamic derivatives in equations (45) - (50) should be evaluated at some average conditions according to the Beecham-Titchener method. These six coupled nonlinear first-order differential equations can be integrated numerically to find a, ξ, η, ε, ν,and δ as functions of t for known initial conditions.

To suppress the wing rock effectively, the main aerodynamic nonlinearities causing the self-induced limit cycle must be understood and justified first. An approximate theory, such as the one developed here, is an efficient tool for recognizing the aerodynamic nonlinearities important to the amplitude and frequency of a limit cycle. The amplitude of a limit cycle is the primary concern as a handling-quality or safety problem. Therefore, the main effort here is to find out the effects of amplitudes of β and ψ modes on that of the ϕ mode for a steady-state limit-cycle oscillation.

To obtain the limit-cycle amplitude of a sustained wing rock, λ is set to zero. In addition, the phase angles, ε and δ, are ignored since they are found numerically to be insignificant for a steady-state constant-amplitude wing rock. Equations (45) - (50) are then reduced to

$$0 \approx \bar{Y}_{\beta} G + \bar{Y}_{\phi} \tag{51}$$

$$G \approx \bar{Y}_{p} + \bar{Y}_{r} H \tag{52}$$

$$\Omega^2 = -\bar{L}_{\beta} G \tag{53}$$

$$0 \approx \bar{L}_{p0} + \frac{4}{3\pi} \bar{L}_{p\beta} AG + \frac{8}{3\pi} \bar{L}_{pp} A\Omega + \bar{L}_{r} H \tag{54}$$

$$H\Omega^2 = -\bar{N}_{\beta} G \tag{55}$$

$$0 \approx \bar{N}_{p0} + \frac{4}{3\pi} \bar{N}_{p\beta} AG + \frac{8}{3\pi} \bar{N}_{pp} A\Omega + \bar{N}_{r} H \tag{56}$$

where G and H are the amplitude ratios of β and ψ modes to the ϕ mode at limit-cycle conditions.

It is assumed that the frequencies of ϕ, β,and ψ modes are the same in equations (45) - (50). Because equations (51) and (55) are related to the frequencies of β and ψ modes respectively, they can be ignored in order to find the effects of β-ψ amplitudes on the ϕ amplitude for a steady-state wing rock. The limit-cycle conditions are then obtained in appendix B by rearranging equations (52), (53), (54), and (56) into the forms

$$A = -\frac{3\pi}{4}\frac{\bar{L}_{p0} + H\bar{L}_r}{G\bar{L}_{p\beta} + 2\Omega\bar{L}_{pp}}$$

$$= -\frac{3\pi}{4}\frac{gC_{\ell_{p0}} + fC_{n_{p0}}}{G(gC_{\ell_{p\beta}} + fC_{n_{p\beta}}) + \frac{\Omega b}{V}(gC_{\ell_{pp}} + fC_{n_{pp}})} \tag{57}$$

where

$$h = \frac{I_{zz}\,C_{\ell_r} + I_{xz}\,C_{n_r}}{I_{xz}\,C_{\ell_r} + I_{xx}\,C_{n_r}}$$

$$g = 1 - h\frac{I_{xz}}{I_{zz}}$$

$$f = \frac{I_{xx}}{I_{zz}}\left(\frac{I_{xz}}{I_{xx}} - h\right)$$

$$\Omega^2 = -G\bar{L}_\beta$$

$$= -G\bar{q}Sb\frac{I_{zz}\,C_{\ell_\beta} + I_{xz}C_{n_\beta}}{I_{xx}I_{zz} - I_{xz}^2} \tag{58}$$

$$G = \bar{Y}_p + H\bar{Y}_r$$

$$= \sin\alpha_s - H\cos^2\alpha_s + \frac{\bar{q}Sb}{2mV^2}C_{Y_p} + H\frac{\bar{q}Sb}{2mV^2}C_{Y_r}\cos\alpha_s \tag{59}$$

$$H = -\frac{1}{\bar{N}_r}\left[\bar{N}_{p0} + \frac{4}{3\pi}A\,(G\,\bar{N}_{p\beta} + 2\Omega\,\bar{N}_{pp}\right)$$

$$= -\frac{I_{xz}C_{\ell_{p0}} + I_{xx}C_{n_{p0}} + \frac{4}{3\pi}A[G(I_{xz}C_{\ell_{p\beta}} + I_{xx}C_{n_{p\beta}}) + \frac{b\Omega}{V}(I_{xz}C_{\ell_{pp}} + I_{xx}C_{n_{pp}})]}{(I_{xz}C_{\ell_r} + I_{xx}C_{n_r})\cos\alpha_s} \tag{60}$$

The roll amplitude of a limit cycle is affected not only by C_{ℓ_β}, $C_{\ell_{p0}}$, $C_{\ell_{p\beta}}$, and $C_{\ell_{pp}}$ as in the one-DOF model but also by C_{n_β}, C_{Y_p}, C_{Y_r}, $C_{n_{p0}}$, $C_{n_{p\beta}}$, $C_{n_{pp}}$, C_{ℓ_r}, and C_{n_r} as shown in equation (57). Equations (57) - (60) are coupled nonlinear algebraic equations in terms of A, G, H, and Ω. They can be solved through simple iterations started with G = $\sin \alpha_s$. For a steady-state wing rock, all solutions must be real and positive.

4. Numerical Results and Discussions

It would be of great interest if the predictions of the present theoretical results could be shown to agree with measured wing-rock characteristics of aircraft, such as the F-4, F-5, F-14, X-29A, Gnat, Harrier, HP 115, and some reentry vehicles. Unfortunately, not all aerodynamic derivatives needed in equations (57) - (60) are available. In addition, it is difficult to estimate the high-α aerodynamic derivatives for a full-scale airplane especially when effects of vortex breakdown, viscous flow separation, and the aerodynamic hysteresis on the wing become significant.

A recent theoretical study of slender wings (ref. 44) based on the quasi-vortex-lattice method (ref. 45) and the suction analogy (ref. 46) showed that the longitudinal and lateral-directional aerodynamics with vortex-breakdown effects at high α can be reasonably well predicted. Therefore, the updated steady-flow aerodynamics computer code (VORSTAB)** based on reference 44 will be used here to calculate all required aerodynamic derivatives for slender wings for the present purpose.

To test the one-DOF theory, a delta wing with 80° leading-edge sweep (ref. 8) is chosen. To verify the three-DOF theory, eight flying wings with vertical tails (ref. 29) are selected.

Having formulated the mathematical model on body-fixed axes, $\dot{\beta}$ derivatives must be included in all p and r derivatives. However, no existing theoretical methods are available for predicting $\dot{\beta}$ derivatives.

**The VORSTAB computer code is available through the NASA Langley Research Center.

Since the aerodynamic nonlinearities of wing rock mainly arise from the nonlinear roll damping of the wing, it is decided to correlate the roll damping derivatives ($C_{\ell_{p_s}}$) based on stability axes and calculated from the VORSTAB code with the roll damping derivatives ($C_{\ell_p} + C_{\ell_\beta} \cdot \sin \alpha_s$) based on body axes and obtained in forced-oscillation tests. The reason is that the effect of $C_{\ell_\beta} \cdot$ on C_{ℓ_p} based on body axes is similar to that of $C_{\ell_{r_s}}$ on $C_{\ell_{p_s}}$ based on stability axes. The results of four delta wings with 80°, 76°, 74°, and 60° leading-edge sweep (refs. 8, 22, 47,48, and 49) are presented in figures 15-18, Two conclusions can be made with regard to comparison between the calculated $C_{\ell_{p_s}}$ and data of $C_{\ell_p} + C_{\ell_\beta} \cdot \sin \alpha_s$. First, the agreement is reasonably good if the amplitude in forced-oscillation test is not too small and the vortex-breakdown effect is not significant. Second, the agreement is better if data of the forced-oscillation technique are compared instead of those of the free-to-damp-oscillation method.

To simulate a one-DOF free-to-roll test or forced-oscillation test based on body axes, an appropriate location of moment center must be chosen if the VORSTAB code is to be used to calculate the aerodynamic derivatives on stability axes. It should be noted that the VORSTAB code is to simulate the rotary-test results. The moment-center locations used in the present study are set at the aerodynamic-center location taken from wind-tunnel data (refs. 22 and 47). Figures 15-18 confirm that the aerodynamic-center location is a good choice for the moment

center if the aerodynamic derivatives are to be calculated on stability axes. Furthermore, numerical results also show that the aerodynamic derivatives change very little if the moment-center location moves ± 0.10 $\bar{c}$ from the aerodynamic-center location.

Knowing that the roll-dominated wing rock is mainly a lateral problem caused by the wing, the VORSTAB code is now used to calculate $C_{\ell_{p_s}}$ and $C_{\ell_{r_s}}$ for C_{ℓ_p} (actually $C_{\ell_p} + C_{\ell_\beta} \cdot \sin \alpha_s$) and C_{ℓ_r} (actually $C_{\ell_r} - C_{n_\beta} \cdot \cos \alpha_s$) respectively. The other aerodynamic derivatives are calculated on body axes.

4.1. One-Degree-of-Freedom solutions

To verify the one-DOF theory, a flat-plate delta wing with 80° leading-edge sweep is chosen because its wind-tunnel data of static-force, forced-oscillation, rotary, and free-to-roll tests have been well conducted and published (ref. 8).

According to the Beecham-Titchener method, all aerodynamic derivatives should be evaluated at some average dynamic conditions. Since the interaction between aerodynamics and dynamics in wing rock is strongly nonlinear, an iterative scheme (appendix C) is developed to calculate the average aerodynamic derivatives and dynamic characteristics for a steady-state self-induced limit cycle. In other words, the aerodynamic derivatives are calculated at some average dynamic conditions (i.e. certain average values of β and $\bar{p}$) which in turn depend on the aerodynamic characteristics.

The calculated longitudinal aerodynamic derivatives of the test configuration are presented in figure 19. The predicted results agree quite well with wind-tunnel data even at α beyond α_{BD} (α_{BD} = 38°).

The limit-cycle amplitude is the main concern in studying the wing-rock problem. The calculated results are plotted in figure 20. To the first-order approximation, the prediction is generally good up to α of 38°. Beyond that α, a converged solution is difficult to obtain. Besides the strong vortex breakdown effects at higher α, the viscous flow separation will probably also become important. The latter effect is not included in the VORSTAB code. The predicted limit-cycle period is reasonably good as shown in figure 21.

For a limit-cycle oscillation, the values of $C_{\ell_{p0}}$ are positive and those of $C_{\ell_{p\beta}}$ are negative; while those of $C_{\ell_{pp}}$ may be either positive or negative (fig. 22). The effect of $C_{\ell_{pp}}$ is to decrease the predicted limit-cycle amplitudes for α below 30° and above 36°; while it increases the predicted amplitudes for α in between. Without $C_{\ell_{pp}}$, the predicted amplitude is 54.4° (overestimated) at α of 25° and is 31.1° (underestimated) at α of 32°. The predicted maximum amplitude with $C_{\ell_{pp}}$ is 40.7° at α of 32° and is very reasonable when compared with available data (fig. 20). Thus, the roll-rate dependency of roll damping plays an important role in determining the limit-cycle amplitude.

The theoretical variations of all terms in equation (4) for α = 27° and 32° are plotted in figures 23 and 24 respectively. It is seen that magnitudes of $C_{\ell_{p0}}$ and $C_{\ell_{pp}}|\bar{p}|$ are much higher than those of $C_{\ell_{p\beta}}|\beta|$ at lower bank angles while $C_{\ell_{p\beta}}|\beta|$ is dominating at higher bank angles. The shape of $C_{\ell_{pt}}$ and its values are affected by the sign of $C_{\ell_{pp}}$.

The histograms of C_ℓ versus ϕ for one limit cycle of wing rock based on equations (3) and (4) without C_{ℓ_0} or the control term at α of 27° and 32° are presented in figures 25 and 26 respectively. The loops give evidence of dynamic hysteresis during the wing rocking. Agreement of theoretical contours with the data derived from free-to-roll tests (ref. 8) is reasonable. The theoretical loops are symmetric against positive and negative bank angles, but the experimental loops depict some asymmetries.

To understand the loop asymmetries, it is known that the induced rolling moment at zero sideslip C_{ℓ_0} increases with increasing α for a highly swept delta wing. The existing data of C_{ℓ_0} (refs. 8, 9, and 22) vary with the model and the wind tunnel used in the static-force tests for a delta wing with 80° sweep. The vortex asymmetry is the main factor to cause the induced rolling moment at zero sideslip. The net difference of experimental C_{ℓ_0} between clockwise and counterclockwise loops (i.e. ΔC_ℓ at ϕ of 0°) determines which direction the wing will tilt and how the dynamic loop will shift with respect to the theoretical prediction. The VORSTAB code can not predict C_{ℓ_0}. At α of 27°, ΔC_{ℓ_0} is +0.01 (fig. 25). The dynamic loops shift up. The positive amplitude is 5° greater than the negative amplitude. At α of 32°, ΔC_{ℓ_0} is -0.05 (fig. 26). The dynamic loops rotate counter-clockwise. The positive amplitude is 5° less than the negative amplitude. In addition, during the oscillation the effect of time lags strongly affects the vortex patterns, causing the dynamic hysteresis. It is the combination of vortex asymmetry and time lag which produces the asymmetrical histogram in experiment.

The total aerodynamic energy exchanged over a limit-cycle oscillation is given by

$$\Delta E = \bar{q}Sb \int_{C(t)} C_\ell(t)\, \dot{\phi}(t)\, dt \tag{61}$$

or

$$\Delta E = \bar{q}Sb \int_{C(\phi)} C_\ell(\phi)\, d\phi \tag{62}$$

where $C(t)$ and $C(\phi)$ are the contours obtained by plotting C_ℓ versus t and ϕ respectively. For a steady-state wing rock, $C(\phi)$ is a closed curve over one oscillation cycle as shown in figures 25 and 26, where the arrows indicate the direction of increasing time. As derived in appendix D, equation (62) can be reduced to

$$\Delta E = 2\bar{q}Sb^2\Omega/V \int_0^A C_{\ell_{pt}} (A^2 - \phi^2)^{1/2}\, d\phi \tag{63}$$

This equation points out that the net energy transferred is exclusively determined by the total aerodynamic roll damping. In other words, to the first-order approximation it has nothing to do with C_{ℓ_0} and C_{ℓ_β}. The areas within the clockwise loops are positive or dynamically undamped due to a positive $C_{\ell_{pt}}$ so that energy is added to the aircraft. On the other hand, the areas within the counterclockwise loops are negative or dynamically damped due to a negative $C_{\ell_{pt}}$ so that energy is consumed by the aircraft. It is shown in appendix D that ΔE is theoretically zero, or the area of the destabilizing loops equals that of the stabilizing loops. Therefore, the net aerodynamic energy added to the aircraft and extracted from it is theoretically zero over an ideal limit-cycle oscillation. Numerical results (figs. 25 and 26)

further testify that the energy balance between the work input and the energy consumed is required to sustain a steady-state wing rock.

The intersection of stabilizing and destabilizing loops represents a turning point of roll damping because $C_{\ell_{pt}}$ is zero at that point. The critical bank and sideslip angles, ϕ_c and β_c, are defined as the angles of zero total aerodynamic roll damping. The aircraft is dynamically undamped below ϕ_c and damped above ϕ_c. The solutions of ϕ_c are (appendix D)

$$
\begin{aligned}
|\phi_c| &= \frac{1}{2r}\left[-s + (s^2 - 4rd)^{1/2}\right] && \text{if } C_{\ell_{pp}} > 0 \\
|\phi_c| &= -\frac{s}{2r} = -\frac{C_{\ell_{p0}}}{\sin\alpha_s\, C_{\ell_{p\beta}}} && \text{if } C_{\ell_{pp}} = 0 \\
|\phi_c| &= \frac{1}{2r}\left[-s - (s^2 - 4rd)^{1/2}\right] && \text{if } C_{\ell_{pp}} < 0
\end{aligned}
\tag{64}
$$

where

$$
\begin{aligned}
r &= (\sin\alpha_s\, C_{\ell_{p\beta}})^2 + \left(\frac{b\Omega}{2V} C_{\ell_{pp}}\right)^2 \\
s &= 2\sin\alpha_s\, C_{\ell_{p0}}\, C_{\ell_{p\beta}} \\
d &= C_{\ell_{p0}}^2 - \left(\frac{b\Omega}{2V} A\, C_{\ell_{pp}}\right)^2
\end{aligned}
\tag{65}
$$

The predicted ϕ_c and β_c are shown in figure 27. It is fairly good as compared with the available data (ref. 8).

4.2. Three-Degree-of-Freedom Solutions

Simple flying wings with a vertical tail but without a horizontal tail or fuselage were extensively tested in the NACA Langley free-flight tunnel (ref. 29). Four models having delta wings with 53°, 63.5°, 76°, and 82.9° leading-edge sweep and four cropped delta wings with a taper ratio of 0.5 are used in verification of the three-DOF theory.

The iterative scheme used in the one-DOF theory (appendix C) is also applicable here. The theoretical results of two flying wings are presented in figures 28 and 29. For both configurations, a 76°-delta wing and a 76°-cropped-delta wing with a vertical tail, the predicted lift coefficients agree well with data up to α of 30°.

The three-DOF theory overpredicts the starting α of wing rock by about 5° as shown in figures 28 and 29. The shaded areas in both figures represent the approximate α range in which the steady-state wing rock was observed. Both α ranges extend over 5° of α approximately. At α below that range, no wing rock was observed. At α above that range, a constant-amplitude roll oscillation kept increasing rapidly as α was increased further. As a result, the flying model rolled completely over out of control. The predicted α ranges of wing rock for both configurations are less than 10° of α. The solid lines in both figures can not be extended to higher-α values because the iterative scheme (appendix C) yields no converged solutions or equations (57) - (60) gives negative amplitudes or imaginary frequencies. Since no limit-cycle amplitudes had been recorded during the flying tests, it is impossible to verify the theoretical amplitudes for both flying models.

Before the flying model reached the α of maximum limit-cycle amplitude, it had probably rolled off because of the great reduction in

the elevon effectiveness at high α. Furthermore, the above theoretical results are calculated for free oscillations without control deflection while the elevons had been used during the free-flight-tunnel tests. At any rate, additional data on these configurations are needed to ascertain the accuracy of the present theory.

Only five flying models with an aspect ratio equal to or less than 1 were reported to exhibit wing rock. The theoretical prediction (fig. 30) has confirmed the same trend. Agreement between the predicted onset α of limit cycle and data is within $\pm 5°$. Since the free-flight-tunnel models simulate the more realistic cases as compared to one-DOF free-to-roll models, figure 30 can serve as a preliminary design guide for aircraft design engineers.

The predicted period of a limit cycle decreases as α increases. The calculated limit-cycle periods are generally greater than four seconds for those five flying models exhibiting wing rock. No data of frequency or period were reported. Hence, no comparison is made.

The amplitude ratio of β to ϕ modes at the limit-cycle condition G varies from 0.01 to 0.30 for the above five flying models at different α. On the other hand, the amplitude ratio of ψ to ϕ modes at the limit-cycle condition H remains approximately 0.11 for most cases. Therefore, β and ψ modes have some effects on the roll amplitude of limit cycle in the three-DOF theory.

It is found in the above numerical analyses that in determining the wing-rock characteristics the importance of C_{ℓ_r}, $C_{n_{p0}}$, and C_{n_r} is next to that of $C_{\ell_{p0}}$, $C_{\ell_{p\beta}}$, and $C_{\ell_{pp}}$; while the effects of C_{Y_p}, C_{Y_r}, $C_{n_{p\beta}}$, and $C_{n_{pp}}$ are almost negligible. In the one-DOF theory, it is required that $C_{\ell_{p0}}$ be positive (undamped) to cause a limit-cycle motion. In

contrast to the one-DOF theory, wing rock is possible in the three-DOF theory even if $C_{\ell_{p0}}$ is negative (damped) but weak. The reason is that the combined effects of C_{ℓ_r}, $C_{n_{p0}}$, and C_{n_r} may make the aircraft more unstable in roll oscillations.

In general, there are three possible approaches to suppress or prevent wing rock: (1) airframe reshaping, (2) maneuver limiting, and (3) employing a stability augmentation system (SAS) or an automatic flight control system (AFCS). The first approach requires the detailed aerodynamic reshaping of the basic airframe configuration to provide inherently wing-rock-free capability. The second approach gives a fast solution eliminating wing rock by simply adopting an α-limiter. However, it may degrade usable maneuverability. Thanks to tremendous advances in avionic technology, the third approach employing SAS or AFCS has become the most effective method for attaining strong resistance to wing rock without degrading high maneuverability.

Because wing rock is mainly due to the loss of roll damping at high α, it can be effectively suppressed by using a roll damper SAS to artificially augment roll damping. For example, a 76°-delta wing with a vertical tail is predicted to exhibit a limit-cycle amplitude of 50° at α of 20°, but the limit cycle of this flying wing can be eliminated completely by incorporating an ideal roll damper as shown in appendix E.

5. Conclusions and Recommendations

5.1. Conclusions

A unified theory based on extensive experimental data is proposed to elucidate the basic mechanisms of wing rock. It is concluded that wing rock is triggered by flow asymmetries, developed by negative or weakly positive roll damping, and sustained by nonlinear aerodynamic roll damping.

A new and more general nonlinear aerodynamic model that includes all essential aerodynamic nonlinearities causing wing rock has been developed. The key element is the total aerodynamic roll damping which depends on oscillation amplitude and roll rate and is formulated to encompass the aerodynamic hysteresis implicitly.

The Beecham-Titchener method has been applied and extended to solve the one- and three-DOF equations of motion. To the first-order approximation, the equations of motion are reduced to coupled nonlinear algebraic equations at limit-cycle conditions. These equations are then solved through iterations for the limit-cycle amplitude and frequency. On the other hand, closed-form solutions are obtained for the one-DOF theory.

To determine the numerical values of the limit-cycle amplitude and frequency, the important aerodynamic derivatives such as $C_{\ell_{p0}}$, $C_{\ell_{p\beta}}$, $C_{\ell_{pp}}$, C_{ℓ_r}, $C_{n_{p0}}$, C_{n_r}, C_{ℓ_β}, and C_{n_β}, are required. Because of the strong interaction between aerodynamics and dynamics during wing rocking, these derivatives are evaluated with a steady-flow aerodynamics computer code at some average dynamic conditions in an iterative manner.

Theoretical results show that to sustain a steady-state wing rock, the total aerodynamic roll damping must be negative at small bank angles

in the one-DOF case but it may be negative or weakly positive in the three-DOF case. On the other hand, at larger bank angles it must be positive in both cases. Furthermore, the one-DOF theory indicates that the energy balance between the work input and the energy consumed during motion is another reason for a self-induced wing rock.

Good agreement between theoretical and experimental results has been obtained for many slender wings, of which all but one are equipped with a vertical tail.

5.2. Recommendations

Good comparison of theoretical results with data has been shown for some simple aerodynamic configurations. However, additional comparisons should be done for more configurations if data are available.

More experiments should be conducted to understand some fundamental dynamic phenomena. First, systematic forced-oscillation and rotary tests should be made to investigate the effects of amplitude, frequency, and roll rate on the roll damping for simple configurations at high angles of attack. Second, curved-flow and rolling-flow and pure lateral-translation-oscillation techniques should be applied to determining the pure derivatives such as C_{ℓ_p}, C_{ℓ_r}, C_{n_p}, C_{n_r}, $C_{\ell_{\dot{\beta}}}$, and $C_{n_{\dot{\beta}}}$. Finally, since the one-DOF free-to-roll test seems inadequate to predict wing-rock characteristics in free flight, more free-flight tests should be conducted.

At present, it is very difficult to predict theoretically the high-α aerodynamic derivatives for a complete airplane. The effects of fluid viscosity, time lag, asymmetric forebody vortices, asymmetric leading-edge vortices, viscous flow separation, shock boundary layer

interaction, and other unsteady aerodynamic interferences should be somehow accounted for. At least, a theoretical method for predicting the important $\dot{\beta}$-derivatives for slender wings should be developed.

It is shown that wing rock can be effectively suppressed if a roll damper SAS is incorporated to augment roll damping. However, more research should be done on high-α control law to provide a fast and reliable AFCS for future fighters.

6. References

(1) Beecham, L.J., and Titchener, I.M., "Some Notes on an Approximate Solution for the Free Oscillation Characteristics of Non-Linear Systems Typified by $\ddot{x} + F(x,\dot{x}) = 0$," British Aeronautical Research Council, R & M No. 3651, Aug. 1969.

(2) Chambers, J.R., Gilbert, W.P., and Nguyen, L.T., "Results of Piloted Simulator Studies of Fighter Aircraft at High Angles of Attack," Paper 33, AGARD-CP-235, May 1978.

(3) Orlik-Rückemann, K.J., "Aerodynamic Aspects of Aircraft Dynamics at High Angle of Attack," Journal of Aircraft, Vol. 20, Sept. 1983, pp. 737-752.

(4) Burris, W.R. and Lawrence, J.T., "Aerodynamic Design and Flight Test of U.S. Navy Aircraft at High Angles of Attack," Paper 25, AGARD-CP-102, Apr. 1972.

(5) Skow, A.M. and Titiriga, A., Jr., "A Survey of Analytical and Experimental Techniques to Predict Aircraft Dynamic Characteristics at High Angles of Attack," Paper 19, AGARD-CP-235, May 1978.

(6) Ross, A.J., "Lateral Stability at High Angles of Attack, Particularly Wing Rock," Paper 10, AGARD-CP-260, Sept. 1978.

(7) Bore, C.L., "Post Stall Aerodynamics of the Harrier GR1," Paper 19, AGARD-CP-102, Apr . 1972.

(8) Nguyen, L.T., Yip, L.P., and Chambers, J.R., "Self-Induced Wing Rock of Slender Delta Wings," AIAA Paper 81-1883, Aug. 1981.

(9) Levin, D. and Katz, J., "Dynamic Load Measurements with Delta Wings Undergoing Self-Induced Roll-Oscillation," Journal of Aircraft, Vol. 21, Jan. 1984, pp. 30-36.

(10) Ross, A.J., "Flying Aeroplanes in Buffet," Aeronautical Journal, Vol. 81, Oct. 1977, pp. 427-436.

(11) Cord, T., "Hysteresis-Induced Wing Rock," AFFDL-TM-75-76-FGC, June 1975.

(12) Ross, A.J., "Investigation of Nonlinear Motion Experienced on a Slender-Wing Research Aircraft," Journal of Aircraft, Vol. 9, Sept. 1972, pp. 625-631.

(13) Johnston, D.E., "Identification of Key Maneuver-Limiting Factors in High Angle of Attack Flight," Paper 36, AGARD-CP-235, May 1978.

(14) Titiriga, A., Jr., Ackerman, J.S., and Skow, A.M., "Design Technology for Departure Resistance of Fighter Aircraft," Paper 5, AGARD-CP-199, Nov. 1975.

(15) Fidler, J.E., Schwind, R.G., and Nielsen, J.N., "Investigation of Slender Body Vortices," AIAA Journal, Vol. 15, Oct. 1977, pp. 427-436.

(16) Clark, W.H., Peoples, J.R., "Occurrence and Inhibition of Large Yawing Moments during High Incidence Flight of Slender Missile Configuration," Journal of Spacecraft and Rockets, Vol. 10, Aug. 1973, pp. 510-519.

(17) Kao, H.C., "Side Forces on Unyawed Slender Inclined Aerodynamic Bodies," Journal of Aircraft, Vol. 12, Mar. 1975, pp. 142-150.

(18) Ray, E.J., McKinney, L.W., and Carmichael, J.G., "Maneuver and Buffet Characteristics of Fighter Aircraft," Paper 24, AGARD-CP-102, Apr. 1972.

(19) Hwang, C. and Pi, W.S., "Some Observations on the Mechanism of Aircraft Wing Rock," Journal of Aircraft, Vol. 16, June 1979, pp. 366-373.

(20) Chambers, J.R., DiCarlo, D.J., and Johnson, J.L., Jr., "Applications of Dynamic Stability Parameters to Problems in Aircraft Dynamics," Lecture 17, AGARD-LS-114, Mar. 1981.

(21) Keener, E.R. and Chapman, G.T., "Similarity in Vortex Asymmetries over Slender Bodies and Wings," AIAA Journal, Vol. 15, Sept. 1977, pp. 1370-1372.

(22) Shanks, R.E., "Low-Subsonic Measurements of Static and Dynamic Stability Derivatives of Six Flat-Plate Wings Having Leading-Edge Sweep Angles of 70° to 84°," NASA TN D-1822, 1963.

(23) Wentz, W.H., Jr. and Kohlman, D.L., "Vortex Breakdown on Slender Sharp-Edged Wings," Journal of Aircraft, Vol. 8, Mar. 1971, pp. 156-161.

(24) Bird, J.D., "Tuft-Grid Surveys at Low Speed for Delta Wings," NASA TN D-5045, Feb. 1969.

(25) Chambers, J.R. and Anglin, E.L., "Analysis of Lateral-Directional Stability Characteristics of a Twin-Jet Fighter Airplane at High Angles of Attack," NASA TN D-5361, Aug. 1969.

(26) Grafton, S.B. and Libbey, C.E., "Dynamic Stability Derivatives of a Twin-Jet Fighter Model at Angles of Attack from -10° to 110°," NASA TN D-6091, Jan. 1971.

(27) Nguyen, L.T. and Gilbert, W.P., "Application of High - α Control System Concepts to a Variable-Sweep Fighter Airplane," AIAA Paper 80-1582, Aug. 1980.

(28) Murri, D.G., Croom, M.A., and Nguyen, L.T., "High Angle-of-Attack Flight Dynamics of a Forward-Swept Wing Fighter Configuration," AIAA Paper 83-1837, July 1983.

(29) McKinney, M.O., Jr., and Drake, H.M., "Flight Characteristics at Low Speed of Delta-Wing Models," NACA RM L7K07, Jan. 1948.

(30) Schiff, L.B. and Tobak, M., "Some Applications of Aerodynamic Formulations to Problems in Aircraft Dynamics," Lecture 16, AGARD-LS-114, Mar. 1981.

(31) Lambourne, N.C., Bryer, D.W., and Maybrey, J.F.M., "The Behavior of the Leading-Edge Vortices over a Delta Wing Following a Sudden Change of Incidence," British Aeronautical Research Council, R & M No. 3645, Mar. 1969.

(32) Lan, C.E., "The Unsteady Suction Analogy and Applications," AIAA Journal, Vol. 20, Dec. 1982, pp. 1647-1656.

(33) Green, J.E., Weeks, D.J., and Brooman, J.W.F., "Prediction of Turbulent Boundary Layers and Wakes in Compressible Flow by a Lag-Entrainment Method," British Aeronautical Research Council, R & M No. 3791, Jan. 1973.

(34) DePonte, S. and Baron, A., "Experiments on a Turbulent Unsteady Boundary Layer with Separation," Paper 12, AGARD-CP-296, Sept. 1980.

(35) Ross, A.J., and Beecham, L.J., "An Approximate Analysis of the Non-Linear Lateral Motion of a Slender Aircraft (HP 115) at Low Speeds," British Aeronautical Research Council, R & M No. 3674, May 1970.

(36) Schmidt, L.V., "Wing Rock due to Aerodynamic Hysteresis," Journal of Aircraft, Vol. 16, Mar. 1979, pp. 129-133.

(37) Ericsson, L.E., "The Fluid Mechanics of Slender Wing Rock," AIAA Paper 83-1810, July 1983.

(38) Konstadinopoulos, P., Mook, D.T., and Nayfeh, A.H., "Numerical Simulation of the Subsonic Wing-Rock Phenomenon," AIAA Paper 83-2115, Aug. 1983.

(39) Tobak, M. and Schiff, L.B., "Aerodynamic Mathematical Modeling - Basic Concepts," Lecture 1, AGARD-LS-114, Mar. 1981.

(40) Skow, A.M., Titiriga, A., Jr., and Moore, W.A., "Forebody-Wing Vortex Interactions and Their Influence on Departure and Spin Resistance," Paper 6, AGARD-CP-247, Oct. 1978.

(41) Johnson, J.L., Jr., Grafton, S.B., and Yip, L.P., "Exploratory Investigation of the Effects of Vortex Bursting on the High-Angle-of-Attack Lateral-Directional Stability Characteristics of Highly-Swept Wings," AIAA Paper 80-0463, Mar. 1980.

(42) Simpson, A., "An Algorithm for Autonomous Nonlinear Dynamical Equations," Aeronautical Quarterly, Aug. 1977, pp. 211-234.

(43) Roskam, J, "Airplane Flight Dynamics and Automatic Flight Controls," Roskam Aviation and Engineering Corporation, Lawrence,Kansas, 1979, Chapter 2.

(44) Lan, C.E. and Hsu, C.H., "Effects of Vortex Breakdown on Longitudinal and Lateral-Directional Aerodynamics of Slender Wings by the Suction Analogy," AIAA Paper 82-1385, Aug. 1982.

(45) Lan, C.E., "A Quasi-Vortex-Lattice Method in Thin Wing Theory," Journal of Aircraft, Vol. 11, Sept. 1974, pp. 518-527.

(46) Polhamus, E.C., "Prediction of Vortex-Lift Characteristics by a Leading-Edge Suction Analogy," Journal of Aircraft, Vol. 8, Apr. 1971, pp. 193-199.

(47) Tosti, L.P., "Low Speed Static Stability and Damping-in-Roll Characteristics of Some Swept and Unswept Low-Aspect-Ratio Wings," NACA TN 1468, Oct. 1947.

(48) Boyden, R.P., "Effects of Leading-Edge Vortex Flow on the Roll Damping of Slender Wings," Journal of Aircraft, Vol. 8, July 1971, pp. 543-547.

(49) Johnson, J. L., Jr., "Low-Speed Measurements of Static Stability, Damping in Yaw, and Damping in Roll of a Delta, a Swept, and an Unswept Wing for Angles of Attack from 0° to 90°," NACA RM L56B01, Apr. 1956.

Appendix A. Derivation of Approximate Analytic Solutions of the One-Degree-of-Freedom Model

The Beecham-Titchener method (ref. 1) is basically an extension of the Krylov-Bogoliubov asymptotic method. This method is shown to be a combination of the averaging principle and the method of variation of parameters (ref. 42). For a damped linear system (ref. 1), the first-order approximation of the Beecham-Titchener method gives the exact solution. For such a system, the Krylov-Bogoliubov method yields an incorrect undamped natural frequency. Other examples (ref. 1) involving nonlinear terms are solved with excellent accuracy by using the Beecham-Titchener method. This method is also capable of obtaining the higher-order approximations. Therefore, this method is applied here.

Equation (9) is rewritten as

$$\ddot{\phi} = L_0 + L_{\delta_A} \delta_A + \sin \alpha_s \, L_\beta \, \phi + (L_{p0} + \sin \alpha_s \, L_{p\beta} |\phi| + L_{pp} |\dot{\phi}|) \, \dot{\phi} \qquad (A.1)$$

The solution of equation (A.1) is assumed to be

$$\phi(t) = a(t) \cos \nu(t) \qquad (A.2)$$

ω and λ are defined as

$$\omega = \dot{\nu} \qquad (A.3)$$

$$\lambda = \dot{a}/a \qquad (A.4)$$

where the superscript dot means a time derivative. In addition, let differentiation with respect to the amplitude a be denoted by a superscript prime. Then $\dot{\omega}$, $\dot{\lambda}$, and $\ddot{a}$ can be expressed as

$$\dot{\omega} = a\,\lambda\,\omega' \tag{A.5}$$

$$\dot{\lambda} = a\,\lambda\,\lambda' \tag{A.6}$$

$$\ddot{a} = a\,\lambda(a\,\lambda' + \lambda) \tag{A.7}$$

On differentiating equation (A.2) with respect to time, one obtains

$$\dot{\phi} = a(\lambda\,\cos\,\nu - \omega\,\sin\,\nu) \tag{A.8}$$

$$\ddot{\phi} = a\,\{[\lambda(a\,\lambda' + \lambda) - \omega^2]\,\cos\,\nu - \lambda(a\omega' + 2\omega)\,\sin\,\nu\} \tag{A.9}$$

The Beecham-Titchener method assumes that ω and λ do not vary greatly during one cycle of oscillation. In other words, a, λ, ω, and amplitude derivatives are interpreted as having fixed values and are assigned the values at midcycles. Equation (A.1) without the control deflection term is rewritten as

$$\begin{aligned}\ddot{\phi} &= L_0 + \sin\,\alpha_s L_\beta\; a\,\cos\,\nu + [L_{p0} + \sin\,\alpha_s L_{p\beta}\;\mathrm{sgn}\,(\phi)\; a\,\cos\,\nu \\ &\quad + L_{pp}\;\mathrm{sgn}\,(\dot{\phi})\; a(\lambda\cos\nu - \omega\sin\nu)]\; a(\lambda\cos\nu - \omega\sin\nu) \\ &= F\,(\nu)\end{aligned} \tag{A.10}$$

Equations (A.9) and (A.10) are combined into

$$F(\nu) = a[\lambda(a\lambda' + \lambda) - \omega^2] \cos \nu - a\lambda(a\omega' + 2\omega) \sin \nu \qquad (A.11)$$

Regarding equation (A.11) as a Fourier expansion for $F(\nu)$, the Fourier coefficients can be determined to be

$$\lambda(a\lambda' + \lambda) - \omega^2 = \frac{1}{\pi a} \int_0^{2\pi} F(\nu) \cos \nu \, d\nu \qquad (A.12)$$

$$\lambda(a\omega' + 2\omega) = - \frac{1}{\pi a} \int_0^{2\pi} F(\nu) \sin \nu \, d\nu \qquad (A.13)$$

Equations (A.12) and (A.13) embody the averaging principle. They are similar in form to the Krylov-Bogoliubov first-order-approximation equations, but include new terms in λ^2 and amplitude-derivatives. The amplitude derivatives are neglected in the first-order approximation. Mathematically, this is in accord with the method of variation of parameters (ref. 42).

Before equations (A.12) and (A.13) can be evaluated, the following three groups of nonzero integrals have to be estimated in advance.

Group 1

$$\int_0^{2\pi} \sin \nu \sin \nu \, d\nu = \pi$$

$$\int_0^{2\pi} \cos \nu \cos \nu \, d\nu = \pi$$

$$\int_0^{2\pi} \sin^3\nu \sin\nu \, d\nu = \frac{3}{4}\pi \tag{A.14}$$

$$\int_0^{2\pi} \cos^3\nu \cos\nu \, d\nu = \frac{3}{4}\pi$$

$$\int_0^{2\pi} \sin^2\nu \cos^2\nu \, d\nu = \frac{1}{4}\pi$$

Group 2

$$\int_0^{2\pi} \text{sgn}(\phi) \cos\nu \, d\nu = 4$$

$$\int_0^{2\pi} \text{sgn}(\phi) \sin^2\nu \cos\nu \, d\nu = \frac{4}{3} \tag{A.15}$$

$$\int_0^{2\pi} \text{sgn}(\phi) \cos^2\nu \cos\nu \, d\nu = \frac{8}{3}$$

Group 3

$$\int_0^{2\pi} \text{sgn}(\dot{\phi}) \sin\nu \, d\nu = -4$$

$$\int_0^{2\pi} \text{sgn}(\dot{\phi}) \sin^2\nu \sin\nu \, d\nu = -\frac{8}{3} \tag{A.16}$$

$$\int_0^{2\pi} \text{sgn}(\dot{\phi}) \cos^2\nu \sin\nu \, d\nu = -\frac{4}{3}$$

After lengthy integration, equations (A.12) and (A.13) are reduced to

$$\lambda^2 - \omega^2 \approx \sin\alpha_s \, L_\beta + \lambda \, L_{p0} + \frac{8}{3\pi} a\lambda \sin\alpha_s \, L_{p\beta} + \frac{8}{3\pi} a\lambda \, \omega \, L_{pp} \tag{A.18}$$

$$2\lambda\omega \approx \omega\, L_{p0} + \frac{4}{3\pi}\, a\, \omega \sin\alpha_s\, L_{p\beta} + \frac{4}{3\pi}\, a(\lambda^2 + 2\omega^2)\, L_{pp} \tag{A.19}$$

All the aerodynamic derivatives in equations (A.18) and (A.19) should then be evaluated at some average conditions.

Equation (A.1), a nonlinear second-order differential equation is then converted into two coupled nonlinear first-order differential equations. Ω and A are defined as the circular frequency and amplitude for a steady-state wing rock. Limit-cycle characteristics are obtained by setting λ to zero in equations (A.18) and (A.19). Equations (A.18) and (A.19) are then reduced to

$$-\Omega^2 = \sin\alpha_s\, L_\beta \tag{A.20}$$

and

$$0 = \Omega\, L_{p0} + \frac{4}{3\pi}\, A\, \Omega\, (\sin\alpha_s\, L_{p\beta} + 2\Omega\, L_{pp}) \tag{A.21}$$

The closed-form solutions of Ω and A are

$$\Omega = (-\sin\alpha_s\, L_\beta)^{1/2}$$

$$= \left(-\frac{\bar{q}Sb}{I_{xx}} \sin\alpha_s\, C_{\ell_\beta}\right)^{1/2} \tag{A.22}$$

$$A = -\frac{3\pi}{4}\, \frac{L_{p0}}{\sin\alpha_s\, L_{p\beta} + 2\Omega\, L_{pp}}$$

$$= -\frac{3\pi}{4}\, \frac{C_{\ell_{p0}}}{\sin\alpha_s\, C_{\ell_{p\beta}} + \frac{\Omega b}{V}\, C_{\ell_{pp}}} \tag{A.23}$$

It is noted that at limit-cycle conditions equations (A.18) and (A.19) have been reduced to the frequency and the amplitude equations respectively.

Appendix B. Derivation of Approximate Analytic Solutions of the Three-Degree-of-Freedom Model

The equations of motion, equations (36), (37), (38), (40), and (41) are rewritten without control-deflection terms as

$$\dot{\beta} = \bar{Y}_0 + \bar{Y}_\beta \beta + \bar{Y}_p p + \bar{Y}_r r + \bar{Y}_\phi \phi \tag{B.1}$$

$$\dot{p} = \bar{L}_0 + \bar{L}_\beta \beta + (\bar{L}_{p0} + \bar{L}_{p\beta}|\beta| + \bar{L}_{pp}|p|)\, p + \bar{L}_r r \tag{B.2}$$

$$\dot{r} = \bar{N}_0 + \bar{N}_\beta \beta + (\bar{N}_{p0} + \bar{N}_{p\beta}|\beta| + \bar{N}_{pp}|p|)\, p + \bar{N}_r r \tag{B.3}$$

$$\dot{p} = \ddot{\phi} \tag{B.4}$$

$$r = \dot{\psi} \tag{B.5}$$

Solutions to the above equations are assumed to be

$$\beta(t) = a(t)\, \xi(t) \cos [\, \nu(t) + \varepsilon(t)] \tag{B.6}$$

$$\phi(t) = a(t) \cos \nu(t) \tag{B.7}$$

$$\psi(t) = a(t)\, \eta(t) \cos [\nu(t) + \delta(t)] \tag{B.8}$$

Again, let ω and λ be defined as

$$\omega = \dot{\nu} \tag{B.9}$$

$$\lambda = \dot{a}/a$$

Also, all time derivatives are to be expressed in terms of amplitude derivatives as

$$\begin{aligned}
\dot{\omega} &= a\,\lambda\,\omega' \\
\dot{\lambda} &= a\,\lambda\,\lambda' \\
\ddot{a} &= a\,\lambda\,(a\,\lambda' + \lambda) \\
\dot{\eta} &= a\,\eta'\,\lambda \\
\ddot{\eta} &= a\,\lambda(a\eta''\lambda + a\eta'\lambda' + \eta'\lambda) \\
\dot{\xi} &= a\,\xi'\,\lambda \\
\ddot{\xi} &= a\lambda(a\xi''\lambda + a\xi'\lambda' + \xi'\lambda)
\end{aligned} \tag{B.10}$$

Because the oscillation frequencies of ϕ, ψ, and β modes are assumed to be the same, ε and δ are virtually independent of time. To the first-order approximation, the amplitude derivatives are all neglected in equation (B.10). It follows that the time derivatives of equations (B.6) - (B.8) can be shown to be

$$\dot{\beta} \approx a\,\xi\,[(\lambda\cos\varepsilon - \omega\sin\varepsilon)\cos\nu - (\lambda\sin\varepsilon + \omega\cos\varepsilon)\sin\nu] \tag{B.11}$$

$$\dot{\phi} \approx a(\lambda\cos\nu - \omega\sin\nu) \tag{B.12}$$

$$\ddot{\phi} \approx a[(\lambda^2 - \omega^2)\cos\nu - 2\lambda\omega\sin\nu] \tag{B.13}$$

$$\dot{\psi} \approx a\eta[(\lambda\cos\delta - \omega\sin\delta)\cos\nu - (\lambda\sin\delta + \omega\cos\delta)\sin\nu] \tag{B.14}$$

$$\begin{aligned}
\ddot{\psi} \approx a\eta\{&[\lambda^2 - \omega^2)\cos\delta - 2\lambda\omega\sin\delta]\cos\nu \\
&- [(\lambda^2 - \omega^2)\sin\delta + 2\lambda\omega\cos\delta]\sin\nu\}
\end{aligned} \tag{B.15}$$

Substituting equations (B.4) - (B.15) into (B.1) - (B.3) and averaging over one oscillation cycle according to Beecham-Titchener technique

yield the following first-order-approximation equations without control deflections as

$$\xi(\lambda\cos\varepsilon - \omega\sin\varepsilon) \approx \bar{Y}_\beta\ \xi\ \cos\varepsilon + \bar{Y}_p\lambda + \bar{Y}_r\eta\ (\lambda\cos\delta - \omega\sin\delta) + \bar{Y}_\phi \tag{B.16}$$

$$\xi(\lambda\sin\varepsilon + \omega\cos\varepsilon) \approx \bar{Y}_\beta\ \xi\ \sin\varepsilon + \bar{Y}_p\omega + \bar{Y}_r\eta\ (\lambda\sin\delta + \omega\cos\delta) \tag{B.17}$$

$$\lambda^2-\omega^2 \approx \bar{L}_\beta\xi\cos\varepsilon+\bar{L}_{p0}\lambda + \frac{8}{3\pi}\bar{L}_{p\beta}a\xi\lambda + \frac{8}{3\pi}\bar{L}_{pp}a\lambda\omega+\bar{L}_r\eta(\lambda\cos\delta-\omega\sin\delta) \tag{B.18}$$

$$2\lambda\omega\approx\bar{L}_\beta\ \xi\sin\varepsilon + \bar{L}_{p0}\omega + \frac{4}{3\pi}\bar{L}_{p\beta}\ a\xi\omega + \frac{4}{3\pi}\bar{L}_{pp}\ a\lambda^2 + \frac{8}{3\pi}\bar{L}_{pp}\ a\omega^2$$

$$+ \bar{L}_r\ \eta\ (\lambda\sin\delta + \omega\cos\delta) \tag{B.19}$$

$$\eta[(\lambda^2-\omega^2)\cos\delta - 2\lambda\omega\sin\delta] \approx \bar{N}_\beta\ \xi\ \cos\varepsilon + \bar{N}_{p0}\ \lambda + \frac{8}{3\pi}\bar{N}_{p\beta}\ a\xi\lambda$$

$$+ \frac{8}{3\pi}\bar{N}_{pp}\ a\lambda\omega + \bar{N}_r\eta(\lambda\cos\delta - \omega\sin\delta) \tag{B.20}$$

$$\eta[(\lambda^2-\omega^2)\sin\delta + 2\lambda\omega\cos\delta] \approx \bar{N}_\beta\ \xi\sin\varepsilon + \bar{N}_{p0}\omega + \frac{4}{3\pi}\bar{N}_{p\beta}\ a\xi\omega$$

$$+ \frac{4}{3\pi}\bar{N}_{pp}\ a\lambda^2 + \frac{8}{3\pi}\bar{N}_{pp}\ a\omega^2 + \bar{N}_r\eta\ (\lambda\sin\delta + \omega\cos\delta) \tag{B.21}$$

During this integration process, a, ξ, η, λ, ω, ε, and δ assume fixed-values at midcycles for slowly varying motions. In the meantime, $|\beta|$ is approximated by $|\xi\phi|$ because ϕ and β modes are in phase in most cases. Again, all the aerodynamic derivatives should then be calculated at some average conditions.

Define G and H as the amplitude ratios of the β and ψ modes to the ϕ mode at limit-cycle conditions. The phase angles, ε and δ, are numerically negligible at limit-cycle conditions. In addition, λ is zero for a steady-state wing rock. Equations (B.16) - (B.21) are thus reduced to

$$0 = \bar{Y}_\beta G + \bar{Y}_\phi \tag{B.22}$$

$$G = \bar{Y}_p + \bar{Y}_r H \tag{B.23}$$

$$\Omega^2 = - \bar{L}_\beta G \tag{B.24}$$

$$0 = \bar{L}_{p0} + \frac{4}{3\pi} \bar{L}_{p\beta} AG + \frac{8}{3\pi} \bar{L}_{pp} A\Omega + \bar{L}_r H \tag{B.25}$$

$$-H\Omega^2 = -\bar{N}_\beta G \tag{B.26}$$

$$0 = \bar{N}_{p0} + \frac{4}{3\pi} \bar{N}_{p\beta} AG + \frac{8}{3\pi} \bar{N}_{pp} A\Omega + \bar{N}_r H \tag{B.27}$$

It is implied that the frequencies of ϕ, β, and ψ modes are the same in equations (B.16) - (B.21). Because equations (B.22) and (B.26) are related to the frequencies of β and ψ modes respectively, they will be ignored in determining the effects of β - ψ amplitudes on the ϕ-amplitude for a steady-state wing rock. Thus, equations (B.23), (B.24), (B.25), and (B.27) are reduced to

$$\begin{aligned} G &= \bar{Y}_p + \bar{Y}_r H \\ &= \sin \alpha_s - H \cos^2 \alpha_s + \frac{\bar{q}Sb}{2mV^2} C_{Y_p} + H \frac{\bar{q}Sb}{2mV^2} C_{Y_r} \cos \alpha_s \end{aligned} \tag{B.28}$$

$$\begin{aligned} \Omega^2 &= - \bar{L}_\beta G \\ &= - G \bar{q}Sb \frac{I_{zz} C_{\ell_\beta} + I_{xz} C_{n_\beta}}{I_{xx} I_{zz} - I_{xz}^2} \end{aligned} \tag{B.29}$$

$$A = -\frac{3\pi}{4}\frac{\bar{L}_{p0} + H\bar{L}_r}{G\,\bar{L}_{p\beta} + 2\Omega\,\bar{L}_{pp}}$$

$$= -\frac{3\pi}{4}\frac{g\,C_{\ell_{p0}} + f\,C_{n_{p0}}}{G(g\,C_{\ell_{p\beta}} + f\,C_{n_{p\beta}}) + \frac{\Omega b}{V}(g\,C_{\ell_{pp}} + f\,C_{n_{pp}})} \qquad (B.30)$$

where

$$h = \frac{I_{zz}\,C_{\ell_r} + I_{xz}\,C_{n_r}}{I_{xz}\,C_{\ell_r} + I_{xx}\,C_{n_r}}$$

$$g = 1 - h\,\frac{I_{xz}}{I_{zz}}$$

$$f = \frac{I_{xx}}{I_{zz}}\left(\frac{I_{xz}}{I_{xx}} - h\right)$$

and

$$H = -\frac{1}{\bar{N}_r}\left[\bar{N}_{p0} + \frac{4}{3\pi}A(G\,\bar{N}_{p\beta} + 2\Omega\,\bar{N}_{pp})\right]$$

$$= -\frac{I_{xz}C_{\ell_{p0}} + I_{xx}C_{n_{p0}} + \frac{4}{3\pi}A[G(I_{xz}C_{\ell_{p\beta}} + I_{xx}C_{n_{p\beta}}) + \frac{b\Omega}{V}(I_{xz}C_{\ell_{pp}} + I_{xx}C_{n_{pp}})]}{(I_{xz}\,C_{\ell_r} + I_{xx}\,C_{n_r})\cos\alpha_s} \qquad (B.31)$$

Appendix C. An Iterative Scheme for Calculating Average Aerodynamic Derivatives and Limit-Cycle Characteristics

For a given angle of attack, it is necessary to calculate three values of C_{ℓ_p} at different β and $\bar{p}$ in order to determine $C_{\ell_{p\beta}}$ and $C_{\ell_{pp}}$ by the VORSTAB code. The three values of C_{ℓ_p} are called $C_{\ell_{p0}}$, $C_{\ell_{p1}}$ and $C_{\ell_{p2}}$ respectively. Due to the nature of nonlinear interaction between aerodynamics and dynamics, the most suitable β and $\bar{p}$ for calculating $C_{\ell_{p0}}$, $C_{\ell_{p1}}$ and $C_{\ell_{p2}}$ are obtained through iterations.

ϕ and $\dot{\phi}$ are defined as

$$\phi = a \cos \nu \tag{C.1}$$

and

$$\dot{\phi} = \dot{a} \cos \nu - a\omega \sin \nu = a(\lambda \cos\nu - \omega \sin\nu) \tag{C.2}$$

By applying the limit-cycle condition ($\lambda = 0$) or for slow-varying amplitude with $\dot{a} \approx 0$, equations (C.1) and (C.2) can be combined into

$$\phi^2 + \frac{\dot{\phi}^2}{\Omega^2} = A^2 \tag{C.3}$$

or

$$|\dot{\phi}| = \Omega(A^2 - \phi^2)^{1/2} \tag{C.4}$$

where A and Ω are the limit-cycle amplitude of bank angle and circular frequency respectively.

Equation (C.3) represents the larger ellipse in the phase plane as shown in figure C.1. The smaller ellipse in figure C.1 having one half of the limit-cycle amplitude of the larger ellipse can be defined by

$$\phi^2 + \frac{\dot{\phi}^2}{\Omega^2} = \frac{1}{4} A^2 \tag{C.5}$$

From equation (C.4), the maximum roll rate is

$$p_{max} = |\dot{\phi}_{max}| = \Omega A \tag{C.6}$$

The average bank angle ϕ_{ave} and the average roll rate p_{ave} are calculated from equation (C.5) to be

$$\phi_{ave} = \frac{1}{2} A \tag{C.7}$$

and

$$p_{ave} = \dot{\phi}_{ave} = \frac{1}{2} \Omega A = \frac{1}{2} p_{max} \tag{C.8}$$

The maximum and average sideslip angles, β_{max} and β_{ave}, are obtained as

$$\beta_{max} = A \sin \alpha_s \tag{C.9}$$

and

$$\beta_{ave} = \phi_{ave} \sin \alpha_s = \frac{1}{2} A \sin \alpha_s \tag{C.10}$$

The dimensionless maximum and average roll rates are defined by

$$\tilde{p}_{max} = p_{max} \frac{b}{2V} \tag{C.11}$$

and

$$\bar{p}_{ave} = p_{ave} \frac{b}{2V} \tag{C.12}$$

Now $C_{\ell_{p0}}$ is calculated at $\beta = 0$ and $\bar{p} = \bar{p}_{ave}$. $C_{\ell_{p1}}$, is calculated at $\beta = \beta_{ave}$ and $\bar{p} = 0$. In actual calculation, this is taken to be at $\bar{p} = 0.05$. $C_{\ell_{p2}}$ is calculated at $\beta = \beta_{ave}$ and $\bar{p} = \bar{p}_{max}$. Finally, $C_{\ell_{p\beta}}$ and $C_{\ell_{pp}}$ are calculated by

$$C_{\ell_{p\beta}} = \frac{C_{\ell_{p1}} - C_{\ell_{p0}}}{\beta_{ave}} \tag{C.13}$$

and

$$C_{\ell_{pp}} = \frac{C_{\ell_{p2}} - C_{\ell_{p1}}}{\bar{p}_{max}} \tag{C.14}$$

After $C_{\ell_{p0}}$, $C_{\ell_{p\beta}}$, and $C_{\ell_{pp}}$ are obtained, the roll amplitude of wing rock based on the one-DOF model has been shown (eq. (18)) to be

$$A_f = -\frac{3\pi}{4} \frac{C_{\ell_{p0}}}{\sin \alpha_s \, C_{\ell_{p\beta}} + \frac{b\Omega}{V} C_{\ell_{pp}}} \tag{C.15}$$

Define β_f and $\bar{p}_f$ as

$$\beta_f = A_f \sin \alpha_s \tag{C.16}$$

and

$$\bar{p}_f = \Omega A_f b/2V \tag{C.17}$$

To start the iteration (figure C.2), a proper value of β_{ave} is chosen, say 10 degrees. The corresponding $\bar{p}_{ave}$ and $\bar{p}_{max}$ are calculated from equations (C.6) - (C.12). Ω is obtained from equation (16). $C_{\ell_{p0}}$, $C_{\ell_{p\beta}}$, and $C_{\ell_{pp}}$ are then properly calculated by using the VORSTAB code. The predicted C_{ℓ_β}, $C_{\ell_{p0}}$, $C_{\ell_{p\beta}}$, and $C_{\ell_{pp}}$ are used to find A_f, β_f, and $\bar{p}_f$. If β_f and β_{max} (or $\bar{p}_f$ and $\bar{p}_{max}$) do not agree within a required accuracy, say 0.5 degrees, a second β_{max} is selected to be the average of the first β_{max} and β_f. Two or three iterations are normally needed to get a final converged solution.

In case that $\bar{p}_{ave}$ is less than 0.05, $C_{\ell_{p0}}$ will be calculated at $\beta = 0$ and $\bar{p}_{ave} = 0.05$ and $C_{\ell_{p2}}$ will be calculated at $\beta = \beta_{ave}$ and $\bar{p}_{max} = 0.10$. In this case, only β_f and β_{max} are iterated to be within the required accuracy.

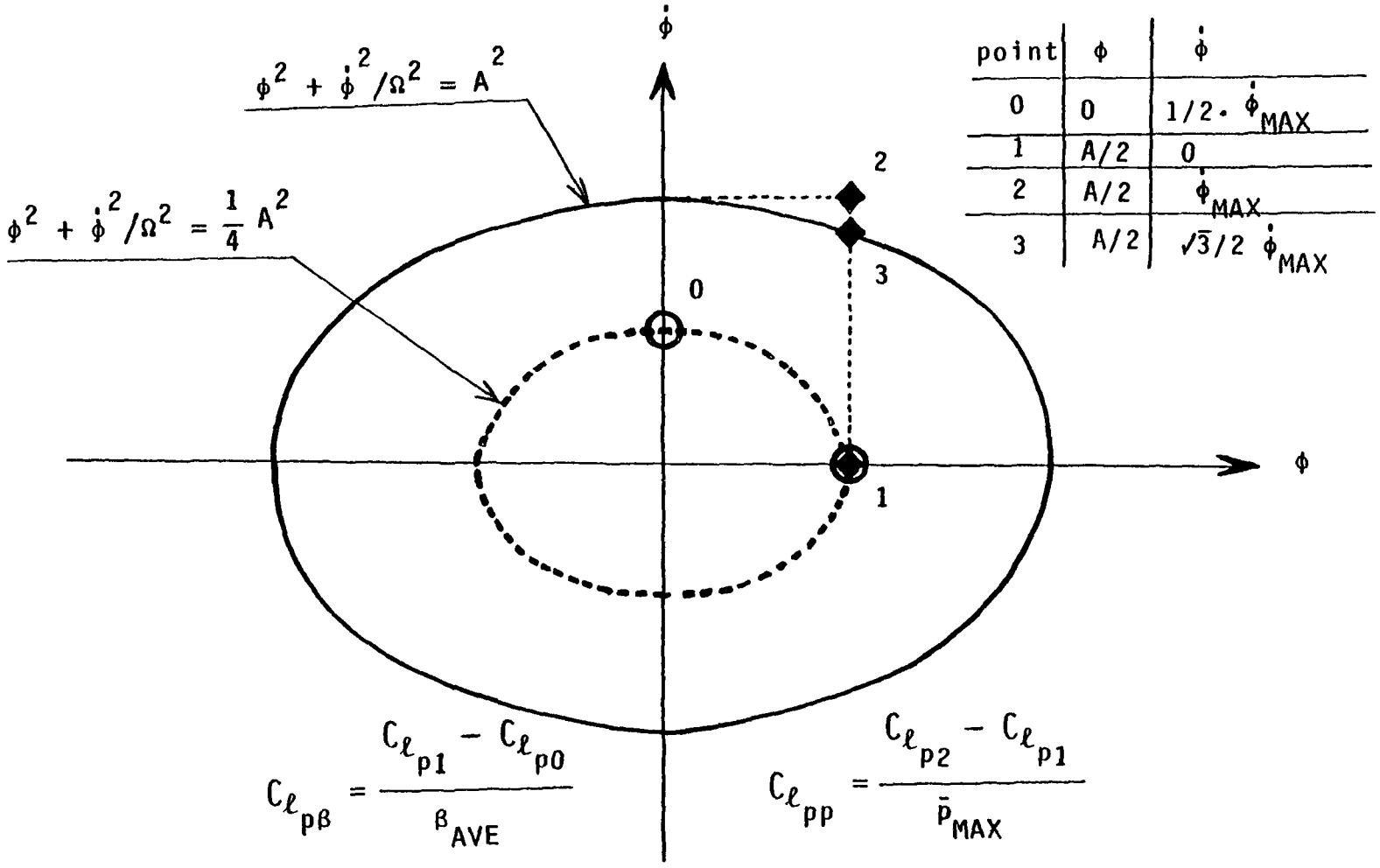

point	ϕ	$\dot{\phi}$
0	0	$1/2 \cdot \dot{\phi}_{MAX}$
1	A/2	0
2	A/2	$\dot{\phi}_{MAX}$
3	A/2	$\sqrt{3}/2\ \dot{\phi}_{MAX}$

Figure C.1. A Typical Phase Plane

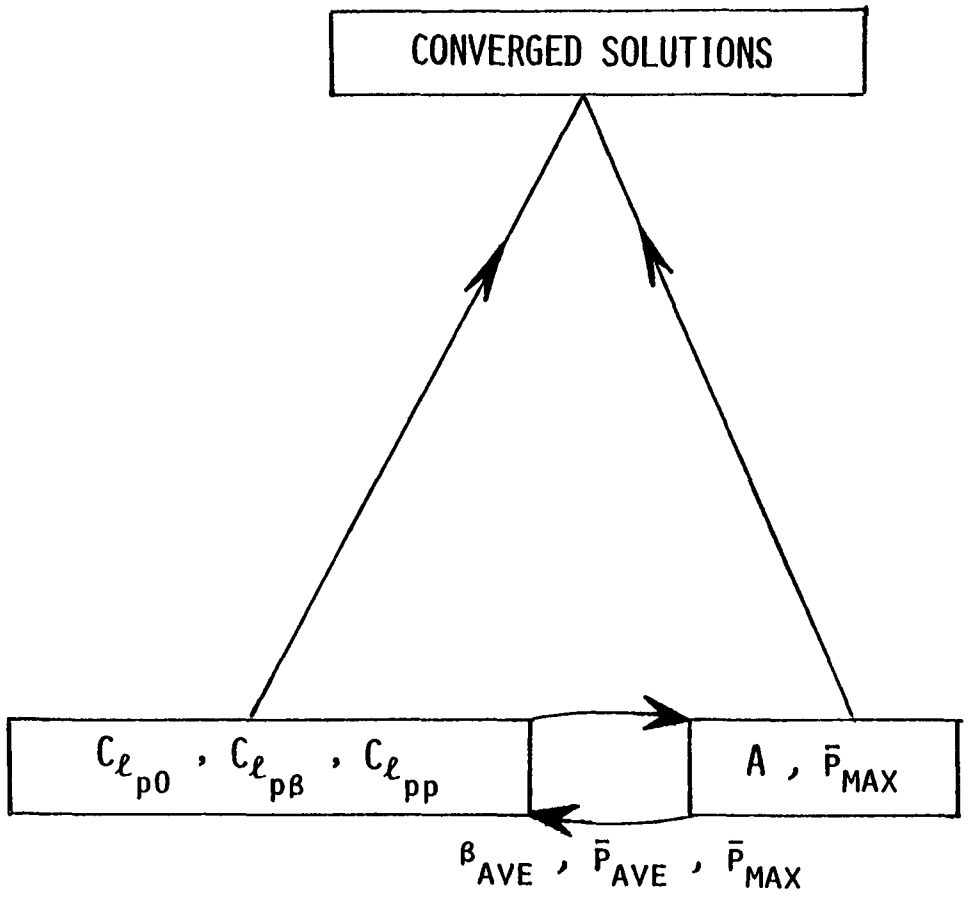

Figure C.2. A Sketch for an Iterative Scheme.

Appendix D. Energy Balance of a Steady-State Wing Rock for the One-Degree-of-Freedom Model

The total aerodynamic energy exchanged over a limit-cycle oscillation is given by

$$\Delta E = \bar{q}Sb \int_{C(t)} C_{\ell}(t)\, \dot{\phi}(t)\, dt \tag{D.1}$$

or

$$\Delta E = \bar{q}Sb \int_{C(\phi)} C_{\ell}(\phi)\, d\phi \tag{D.2}$$

where $C(t)$ and $C(\phi)$ are the contours obtained by plotting C_{ℓ} versus t and ϕ respectively. For a steady-state wing rock, $C(\phi)$ is a closed curve over one oscillation cycle. Since the contours for positive and negative bank angles are theoretically the same, equation (D.2) can be simplified to be

$$\Delta E = 2\bar{q}Sb \int_{ABCBD} C_{\ell}(\phi)\, d\phi \tag{D.3}$$

where the integration path ABCBD is shown in figure D.1. The arrows in figure D.1 indicate the direction of increasing time.

The total aerodynamic roll damping coefficient is defined as

$$C_{\ell_{pt}} = C_{\ell_{p0}} + C_{\ell_{p\beta}} |\beta| + C_{\ell_{pp}} |\bar{p}| \tag{D.4}$$

The total rolling moment coefficient C_{ℓ} can now be rewritten as

$$C_\ell = C_{\ell_0} + C_{\ell_\beta}\beta + C_{\ell_{pt}}\bar{p} \tag{D.5}$$

$\dot{\phi}$ derived in appendix C is given by

$$|\dot{\phi}| = \Omega\ (A^2 - \phi^2)^{1/2} \tag{D.6}$$

When ϕ is increasing, e.g. along the path ABC,

$$p = \dot{\phi} = \Omega(A^2 - \phi^2)^{1/2} \tag{D.7}$$

When ϕ is decreasing, e.g. along the path CBD,

$$p = \dot{\phi} = -\Omega(A^2 - \phi^2)^{1/2} \tag{D.8}$$

Thus equation (D.3) can be rewritten as

$$\Delta E = 2\bar{q}Sb \int_{ABCBD} (C_{\ell_{ABC}} + C_{\ell_{CBD}})\ d\phi \tag{D.9}$$

or

$$\Delta E = 2\bar{q}Sb \int_0^A (C_{\ell_{ABC}} - C_{\ell_{CBD}})\ d\phi \tag{D.10}$$

where

$$C_{\ell_{ABC}} = C_{\ell_0} + C_{\ell_\beta}\beta + C_{\ell_{pt}} \frac{b\Omega}{2V} (A^2 - \phi^2)^{1/2} \tag{D.11}$$

and

$$C_{\ell_{CBD}} = C_{\ell_0} + C_{\ell_\beta}\beta - C_{\ell_{pt}} \frac{b\Omega}{2V} (A^2 - \phi^2)^{1/2} \tag{D.12}$$

so that

$$\Delta E = 2\bar{q}Sb^2 \frac{\Omega}{V} \int_0^A C_{\ell_{pt}} (A^2 - \phi^2)^{1/2} \, d\phi \tag{D.13}$$

The physical mechanism of a steady-state wing rock shows that the dynamic system is undamped over small bank angles and damped over larger bank angles. This can be explained by the dynamic loops in figure D.1 with the help of equation (D.13). The loop ABD is clockwise and the area within this loop is positive. It results in a positive ΔE and implies that $C_{\ell_{pt}}$ is positive, or undamping. Thus, a clockwise loop is dynamically destabilizing because the aerodynamic energy is added to the dynamic system. On the other hand, a counterclockwise loop, say the loop BCB, is dynamically stabilizing due to a negative $C_{\ell_{pt}}$ so that the aerodynamic energy is consumed by the dynamic system.

Substituting equations (D.4) and (D.6) into (D.13) yields

$$\Delta E = 2\bar{q}Sb^2 \frac{\Omega}{V} \int_0^A \{[C_{\ell_{p0}} + \sin\alpha_s C_{\ell_{p\beta}} \phi + \frac{b\Omega}{2V} C_{\ell_{pp}} (A^2-\phi^2)^{1/2}](A^2-\phi^2)^{1/2}\} d\phi \tag{D.14}$$

where

$$\int_0^A C_{\ell_{p0}} (A^2-\phi^2)^{1/2} d\phi = \frac{1}{2} C_{\ell_{p0}} \{\phi(A^2-\phi^2)^{1/2} + A^2 \sin^{-1} \frac{\phi}{A}\}_0^A$$

$$= \frac{\pi}{4} C_{\ell_{p0}} A^2 \tag{D.15}$$

$$\int_0^A \sin\alpha_s C_{\ell_{p\beta}} \phi(A^2-\phi^2)^{1/2} d\phi = -\frac{1}{3} \sin\alpha_s C_{\ell_{p\beta}} \{[(A^2-\phi^2)^3]^{1/2}\}_0^A$$

$$= \frac{1}{3} \sin \alpha_s \, C_{\ell_{p\beta}} \, A^3 \tag{D.16}$$

$$\int_0^A \frac{b\Omega}{2V} C_{\ell_{pp}} (A^2-\phi^2) d\phi = \frac{b\Omega}{2V} C_{\ell_{pp}} \{A^2\phi - \frac{1}{3}\phi^3\}_0^A$$

$$= \frac{1}{3} \frac{b\Omega}{V} C_{\ell_{pp}} A^3 \tag{D.17}$$

Finally, the aerodynamic energy exchanged over an ideal limit cycle is

$$\Delta E = 2\bar{q}Sb^2 \frac{\Omega}{V}\{\frac{\pi}{4} C_{\ell_{p0}} A^2 + \frac{1}{3}\sin\alpha_s \, C_{\ell_{p\beta}} A^3 + \frac{1}{3} \frac{b\Omega}{V} C_{\ell_{pp}} A^3\}$$

$$= \frac{2}{3} \bar{q}Sb^2 \, A^2 \frac{\Omega}{V} \{\frac{3\pi}{4} C_{\ell_{p0}} + A \, (\sin\alpha_s \, C_{\ell_{p\beta}} + \frac{b\Omega}{V} C_{\ell_{pp}})\}$$

$$= \frac{2}{3} \bar{q}Sb^2 \, A^2 \frac{\Omega}{V} \{\frac{3\pi}{4} C_{\ell_{p0}} - \frac{3\pi}{4} C_{\ell_{p0}}\}$$

$$= 0 \tag{D.18}$$

The intersection of stabilizing and destabilizing areas, i.e. the point B in figure D.1 represents a turning point of roll damping because $C_{\ell_{pt}}$ is zero at that particular point. The critical bank and sideslip angles, ϕ_c and β_c, are defined as the angles of zero total aerodynamic roll damping. To find ϕ_c, $C_{\ell_{pt}}$ is set to zero to obtain

$$C_{\ell_{pt}} = C_{\ell_{p0}} + \sin\alpha_s \, C_{\ell_{p\beta}} |\phi_c| + \frac{b\Omega}{2V} C_{\ell_{pp}} (A^2 - \phi_c^2)^{1/2} \tag{D.19}$$

$$= 0$$

or

$$|\phi_c| = \frac{C_{\ell_{p0}} + \frac{b\Omega}{2V} C_{\ell_{pp}} (A^2 - \phi_c^2)^{1/2}}{-\sin \alpha_s \, C_{\ell_{p\beta}}} \tag{D.20}$$

Squaring both sides of equation (D.20) and rearranging give

$$r \, \phi_c^2 + s \, \phi_c + d = 0 \tag{D.21}$$

where

$$r = (\sin \alpha_s \, C_{\ell_{p\beta}})^2 + (\frac{b\Omega}{2V} C_{\ell_{pp}})^2$$

$$s = 2 \sin \alpha_s \, C_{\ell_{p0}} \, C_{\ell_{p\beta}} \tag{D.22}$$

$$d = C_{\ell_{p0}}^2 - (\frac{b\Omega}{2V} A \, C_{\ell_{pp}})^2$$

Solving the quadratic equation (D.21) and comparing its solutions with the numerical solutions obtained from equation (D.20), ϕ_c can be shown to be

$$|\phi_c| = \frac{1}{2r} (-s + (s^2 - 4rd)^{1/2}) \qquad \text{if } C_{\ell_{pp}} > 0$$

$$|\phi_c| = -\frac{s}{2r} = -\frac{C_{\ell_{p0}}}{\sin \alpha_s C_{\ell_{p\beta}}} \qquad \text{if } C_{\ell_{pp}} = 0 \tag{D.23}$$

$$|\phi_c| = \frac{1}{2r} (-s - (s^2 - 4rd)^{1/2}) \qquad \text{if } C_{\ell_{pp}} < 0$$

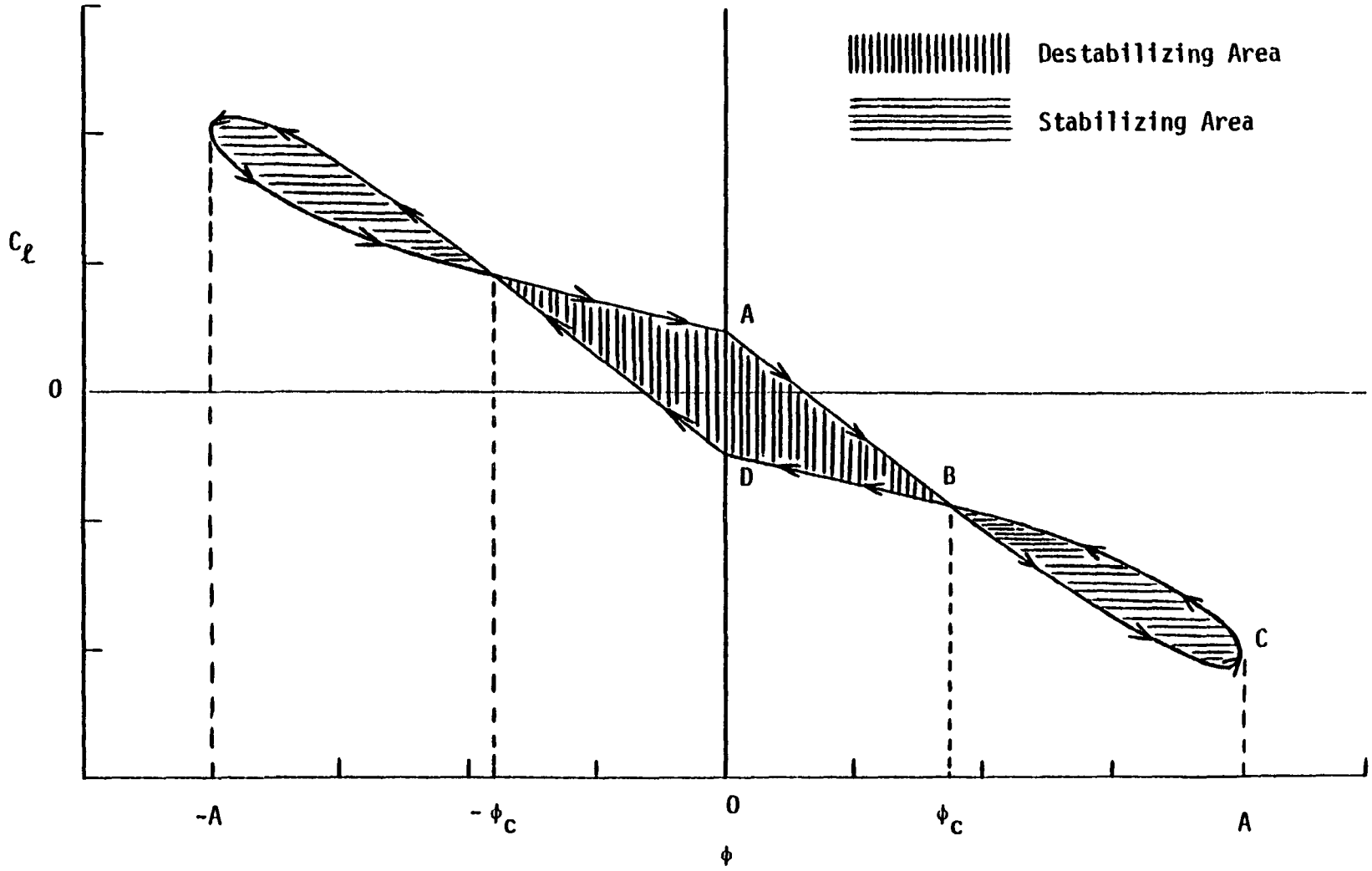

Figure D.1. A Typical Histogram of the Total Aerodynamic Rolling Moment Coefficient versus Bank Angle for One Limit Cycle of Wing Rock (The Arrows Indicate the Direction of Increasing Time).

Appendix E. Suppression of Wing Rock with a Roll Damper

A conventional roll damper is usually designed to quicken the roll response and augment roll damping. It is also a simple control device for suppressing wing rock. An ideal roll damper consists of a rate gyro which senses the airplane roll rate p and then feeds it back to actuate the lateral control unit δ_A in proportion to p but such as to oppose p. The lateral control deflection angle is then

$$\Delta\delta_A = Kp \tag{E.1}$$

where K is the system gain (control surface deflection per unit roll rate) of a roll damper. The corresponding increases in C_{Y_p}, C_{ℓ_p}, and C_{n_p} due to $\Delta\delta_A$ are expressed as

$$\Delta C_Y = C_{Y_{\delta_A}} \cdot \Delta\delta_A = \Delta C_{Y_p} \bar{p} \tag{E.2}$$

$$\Delta C_\ell = C_{\ell_{\delta_A}} \cdot \Delta\delta_A = \Delta C_{\ell_p} \bar{p} \tag{E.3}$$

$$\Delta C_n = C_{n_{\delta_A}} \cdot \Delta\delta_A = \Delta C_{n_p} \bar{p} \tag{E.4}$$

where

$$\bar{p} = p \frac{b}{2V} \tag{E.5}$$

$$\Delta C_{Y_p} = K \frac{C_{Y_{\delta A}}}{b/2V} \tag{E.6}$$

$$\Delta C_{\ell_p} = K \frac{C_{\ell_{\delta A}}}{b/2V} \tag{E.7}$$

$$\Delta C_{n_p} = K \frac{C_{n_{\delta A}}}{b/2V} \tag{E.8}$$

By replacing δ_A, C_{Y_p}, $C_{\ell_{p0}}$, and $C_{n_{p0}}$ in the equations of motion, equations (25) - (27), by $\Delta\delta_A$, $C_{Y_p} + \Delta C_{Y_p}$, $C_{\ell_{p0}} + \Delta C_{\ell_p}$, and $C_{n_{p0}} + \Delta C_{n_p}$, the modified solutions at limit-cycle conditions are obtained to be

$$A = -\frac{3\pi}{4} \frac{g(C_{\ell_{p0}} + \Delta C_{\ell_p}) + f(C_{n_{p0}} + \Delta C_{n_p})}{G(gC_{\ell_{p\beta}} + fC_{n_{p\beta}}) + \frac{\Omega b}{V}(gC_{\ell_{pp}} + fC_{n_{pp}})} \tag{E.9}$$

$$\Omega^2 = -G\bar{q}Sb \frac{I_{zz} C_{\ell_\beta} + I_{xz} C_{n_\beta}}{I_{xx} I_{zz} - I_{xz}^2} \tag{E.10}$$

$$G = \sin\alpha_s - H \cos^2\alpha_s + \frac{\bar{q}Sb}{2mV^2}(C_{Y_p} + \Delta C_{Y_p}) + H \frac{\bar{q}Sb}{2mV^2} C_{Y_r} \cos\alpha_s \tag{E.11}$$

$$H = -\frac{I_{xz}(C_{\ell_{p0}} + \Delta C_{\ell_p}) + I_{xx}(C_{n_{p0}} + \Delta C_{n_p}) + \frac{4}{3\pi}A[G(I_{xz}C_{\ell_{p\beta}} + I_{xx}C_{n_{p\beta}}) + \frac{b\Omega}{V}(I_{xz}C_{\ell_{pp}} + I_{xx}C_{n_{pp}})]}{(I_{xz}C_{\ell_r} + I_{xx}C_{n_r})\cos\alpha_s} \tag{E.12}$$

where

$$h = \frac{I_{zz} C_{\ell_r} + I_{xz} C_{n_r}}{I_{xz} C_{\ell_r} + I_{xx} C_{n_r}} \tag{E.13}$$

$$g = 1 - h \frac{I_{xz}}{I_{zz}} \tag{E.14}$$

$$f = \frac{I_{xx}}{I_{zz}} \left(\frac{I_{xz}}{I_{xx}} - h\right) \tag{E.15}$$

Equations (E.9) - (E.12) are then used to calculate the system gain needed to alleviate the limit-cycle amplitude. A delta wing of 76° sweep with a vertical tail (ref. 29) is chosen to demonstrate the concept. Without a roll damper, $C_{\ell_{p0}}$ and ΔC_{ℓ_p} and the limit-cycle amplitude are predicted respectively to be 0.0071 and -0.0410 and 50° at α of 20°. In contrast to that, the limit cycle can be eliminated completely by installing an ideal roll damper with K ($K = \frac{b}{2V} \frac{\Delta C_{\ell_p}}{C_{\ell_{\delta_A}}}$) less than -0.15°/rad/sec. Note that $C_{Y_{\delta_A}} \approx 0$, $C_{\ell_{\delta_A}} = 0.0046$ (per degree) and $C_{n_{\delta_A}} = 0.0008$ (per degree) calculated from wind tunnel data in reference 29 have been used in equations (E.6) - (E.8). The value of K seems small because the wing span of the wind-tunnel model is only 1.63 ft and the test velocity is 50.2 ft/sec. It is shown that the effect of ΔC_{Y_p} is negligible and augmenting roll damping via ΔC_{ℓ_p} is the most efficient. Therefore, wing rock can be suppressed by using a roll damper to artificially augment roll damping.

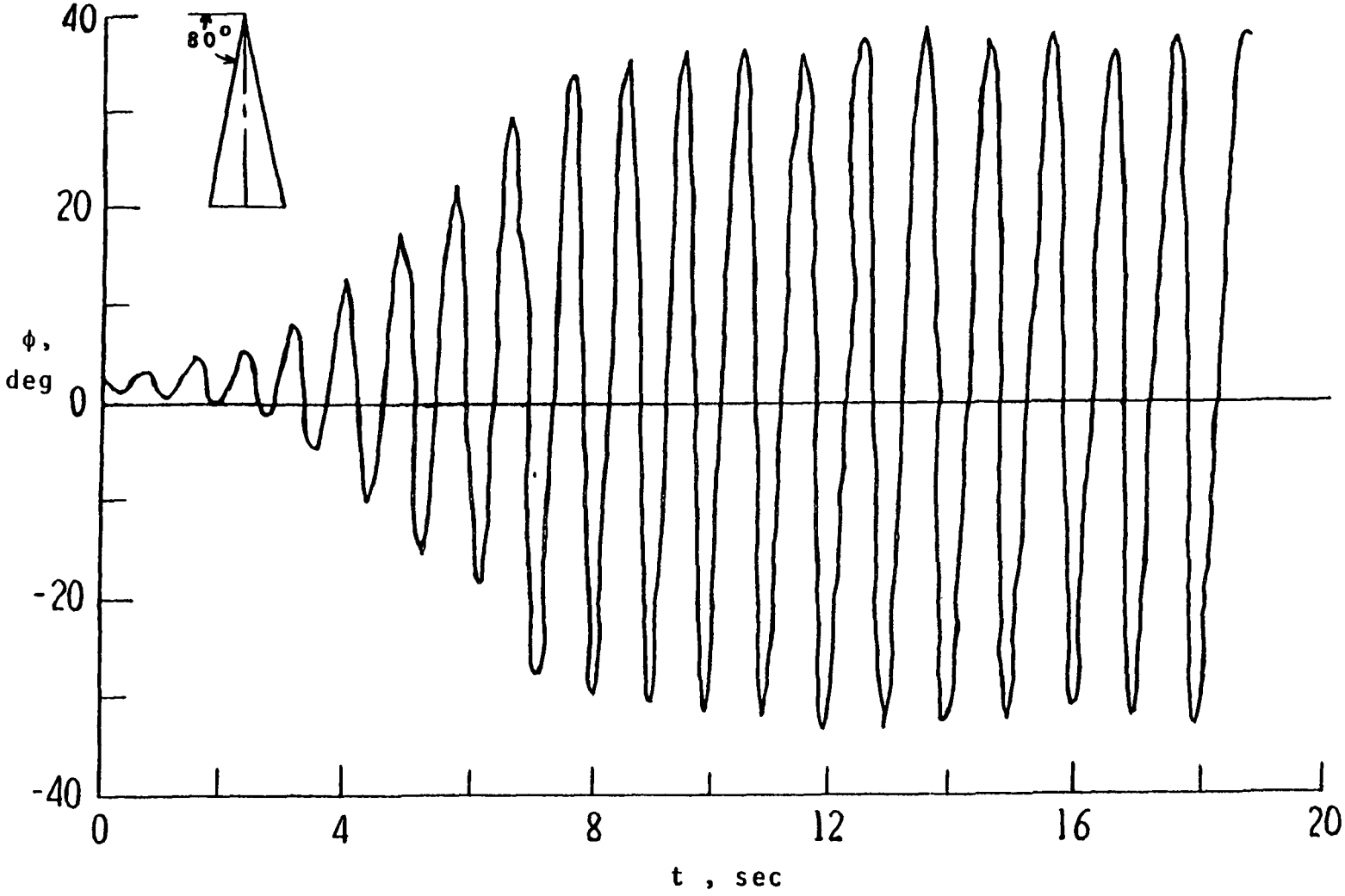

Figure 1. Wing-Rock Buildup of an 80^{o}-Delta Wing at $\alpha_s = 27^{o}$ (ref. 8).

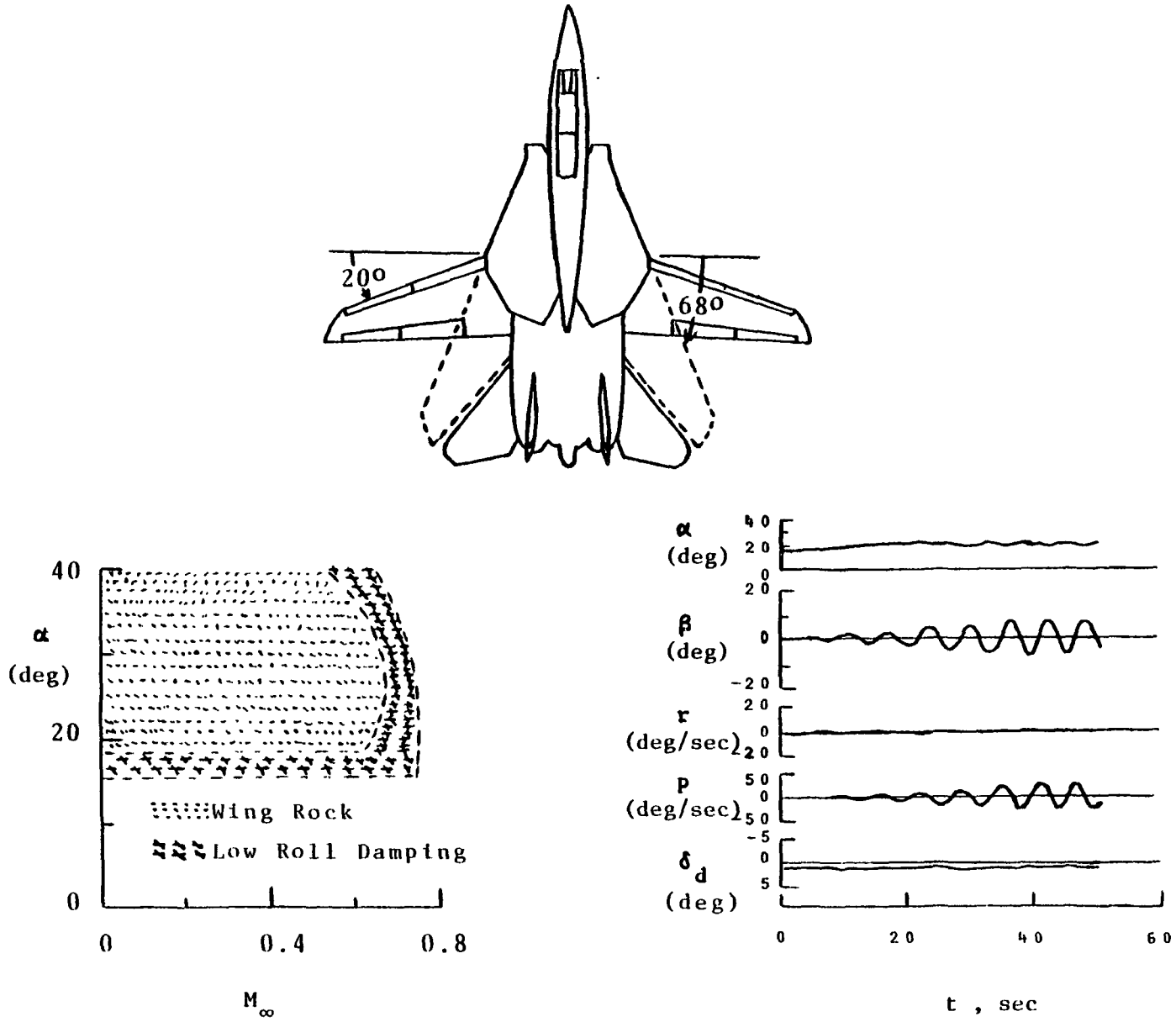

Figure 2. Wing-Rock of the F-14 (ref. 27).

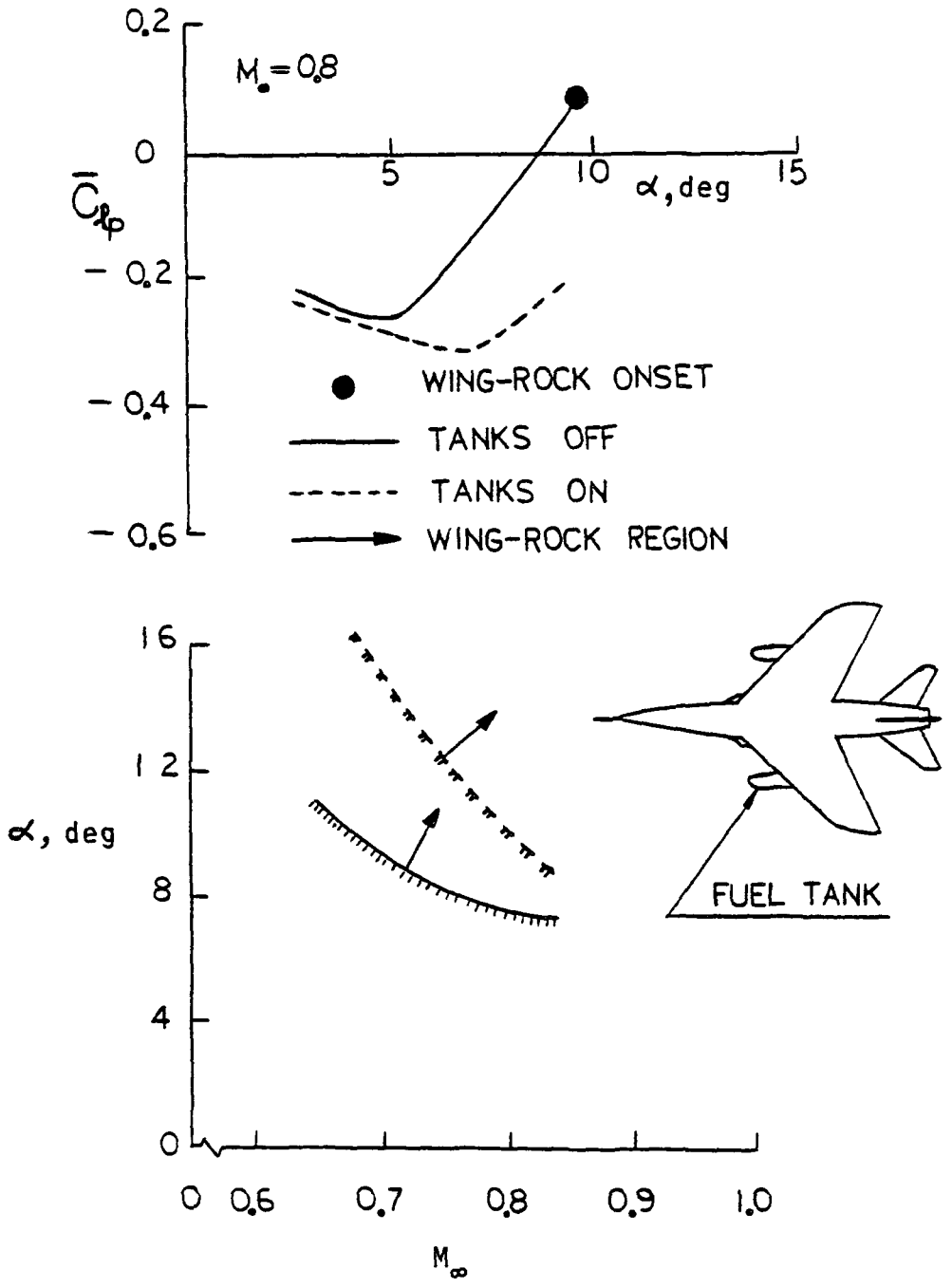

Figure 3. Wing Rock of the Gnat (ref. 10).

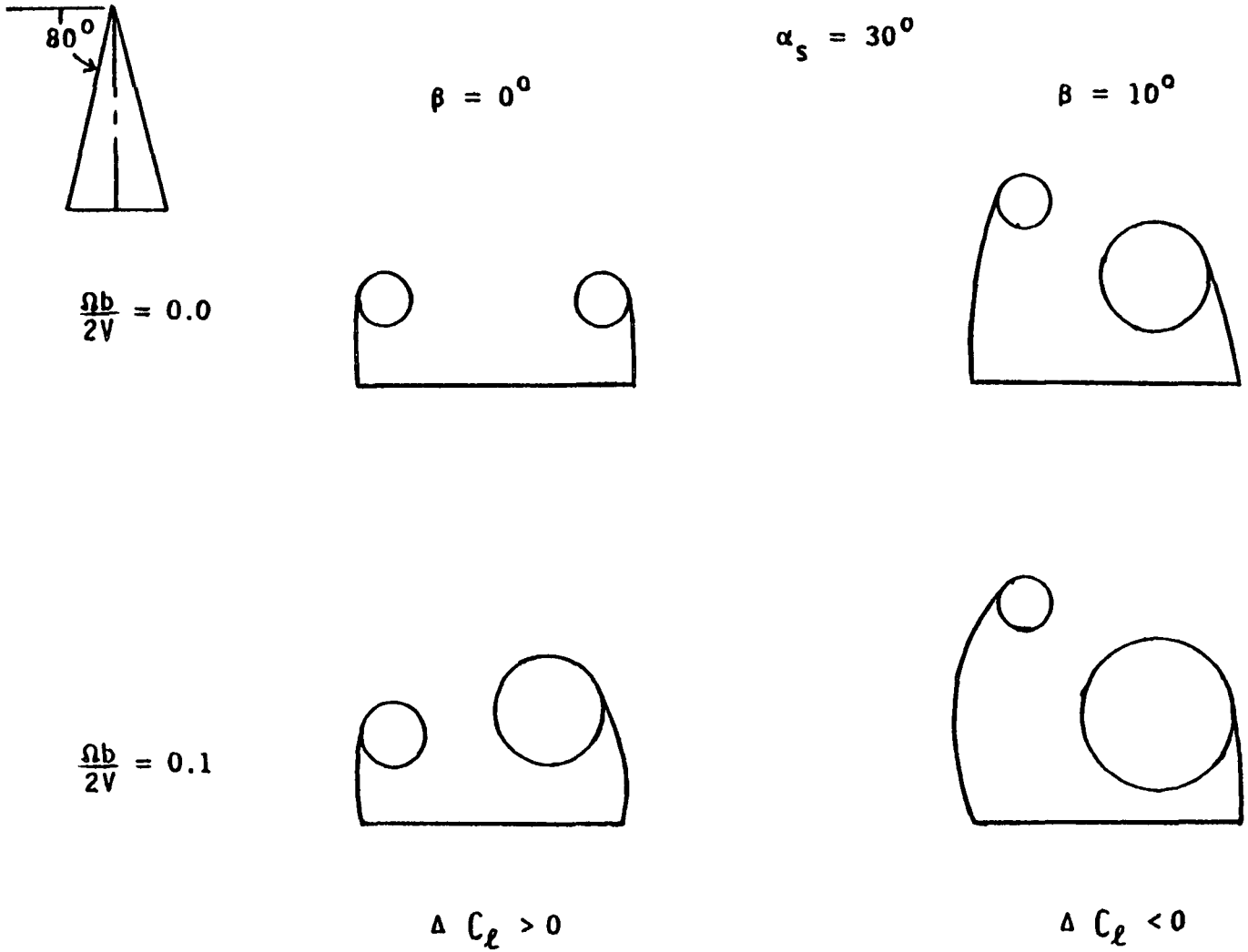

Figure 4. Asymmetric Leading-Edge Vortices for an 80^o-Delta Wing (ref. 8).

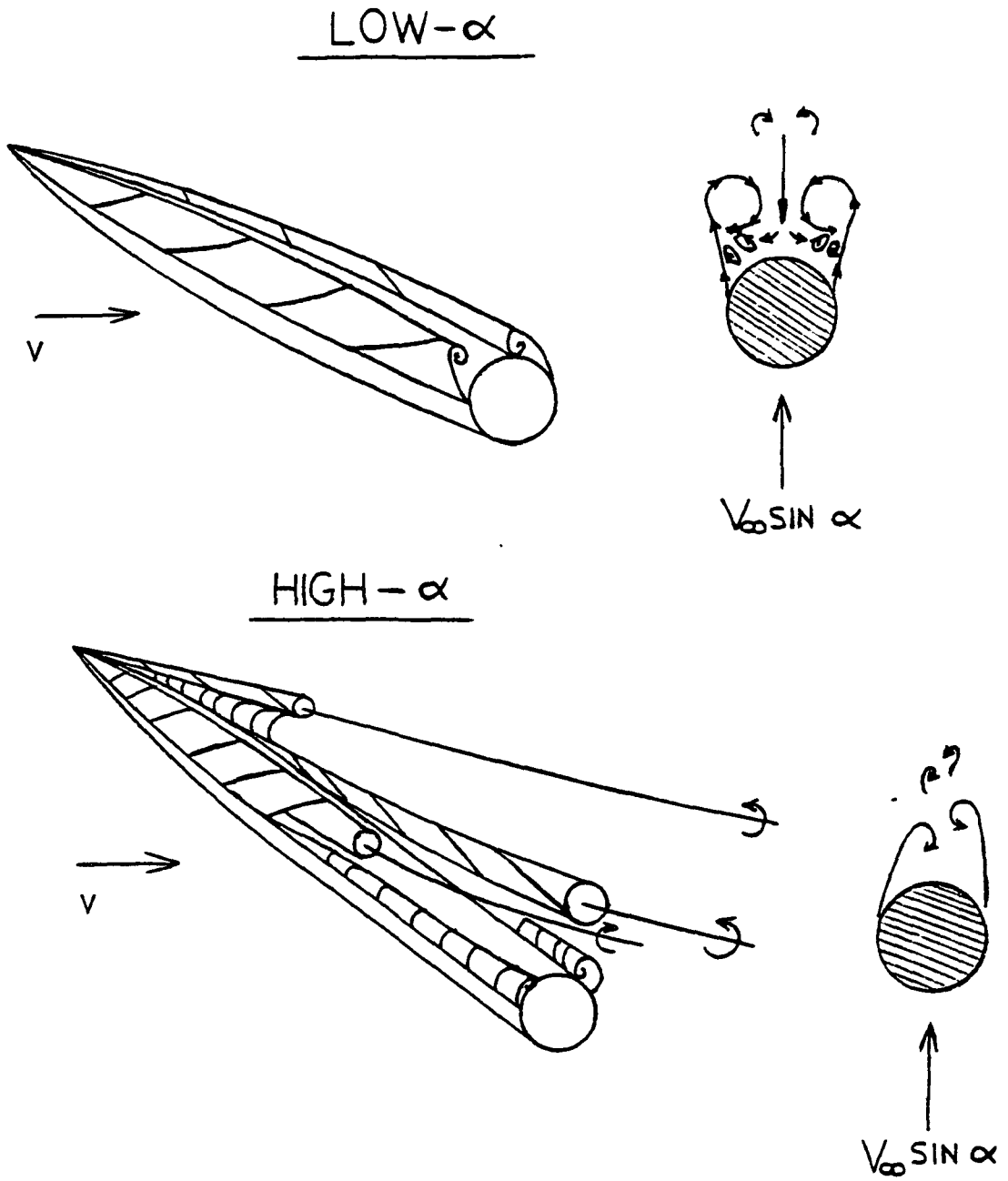

Figure 5. Asymmetric Forebody Vortices at High Angles of Attack (ref. 15).

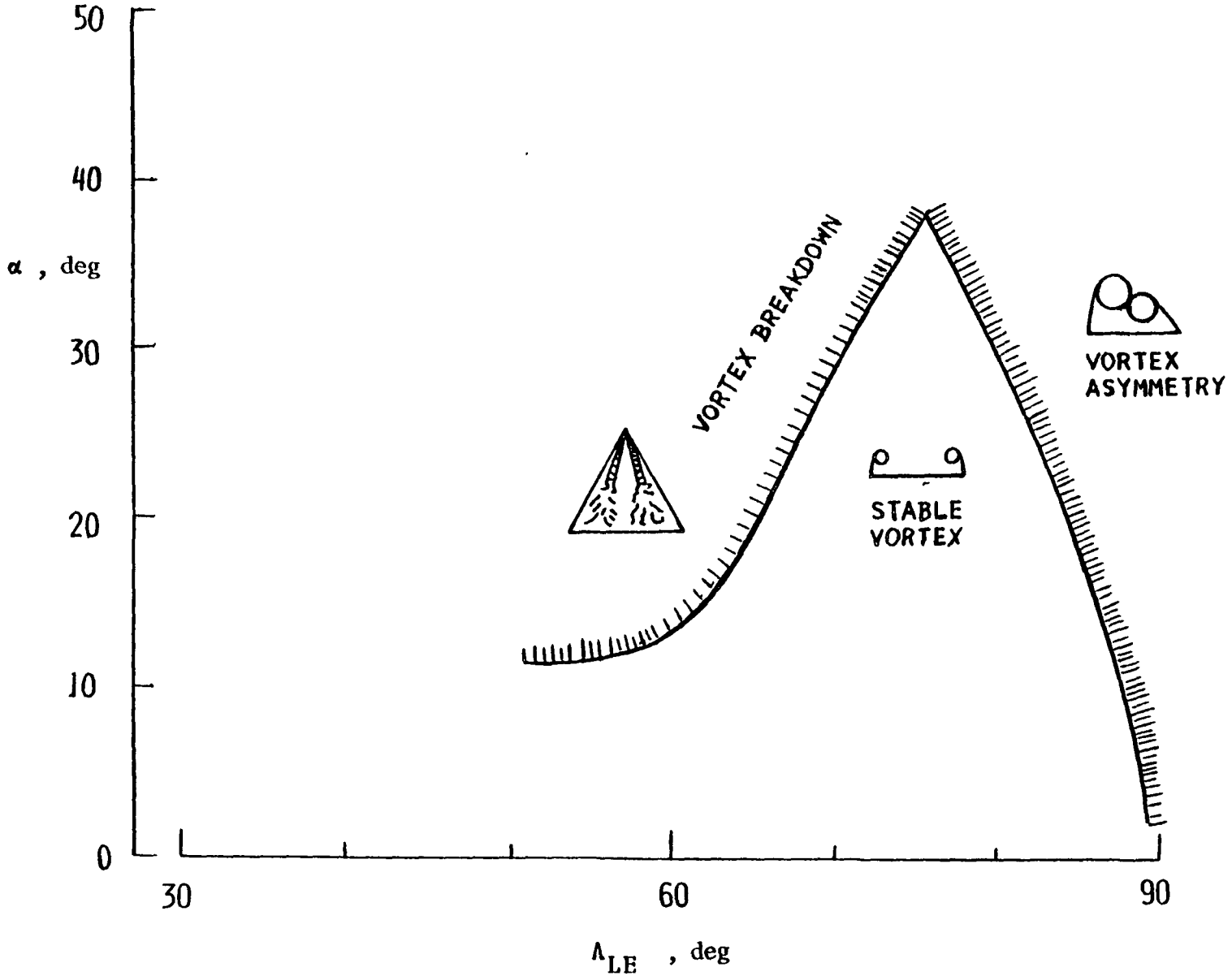

Figure 6. α-Λ_{LE} Boundaries for Vortex Asymmetry and Vortex Breakdown of Sharp-Edge Delta Wings at $M_\infty \approx 0$ (ref. 46).

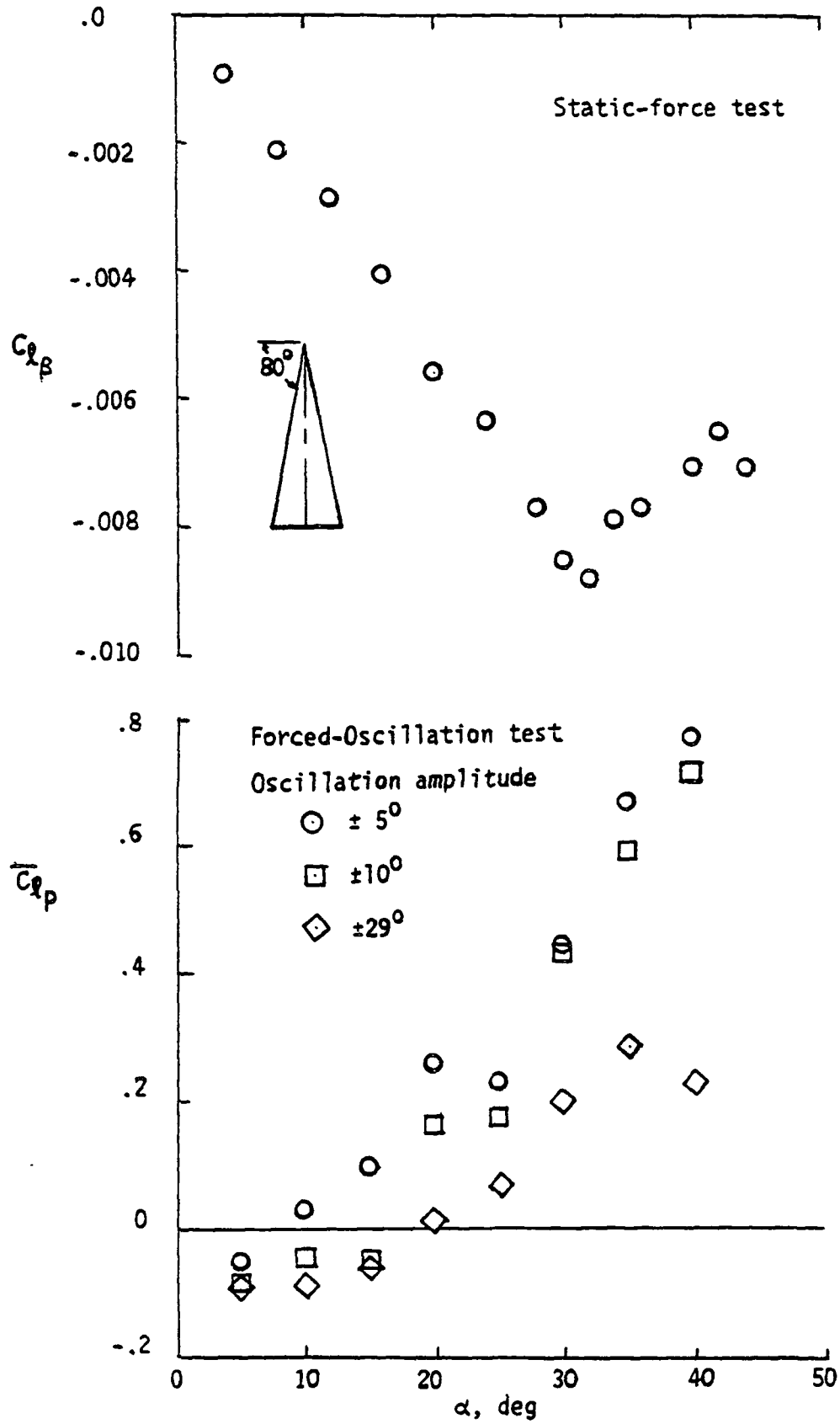

Figure 7. C_{ℓ_β} and $\bar{C}_{\ell_p}$ versus α for an 80°-Delta Wing (ref.8).

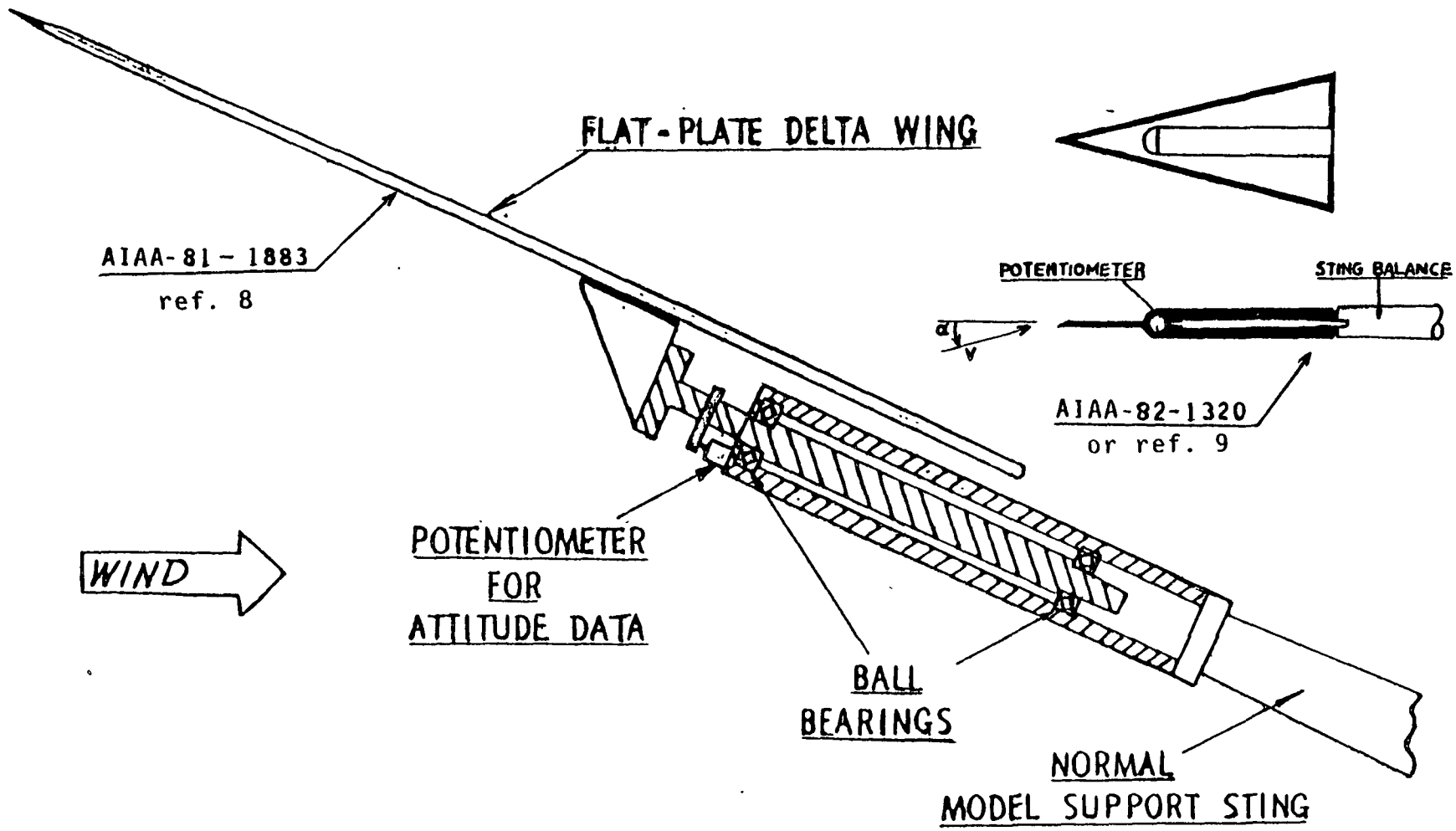

Figure 8. Two Free-to-Roll Rigs.

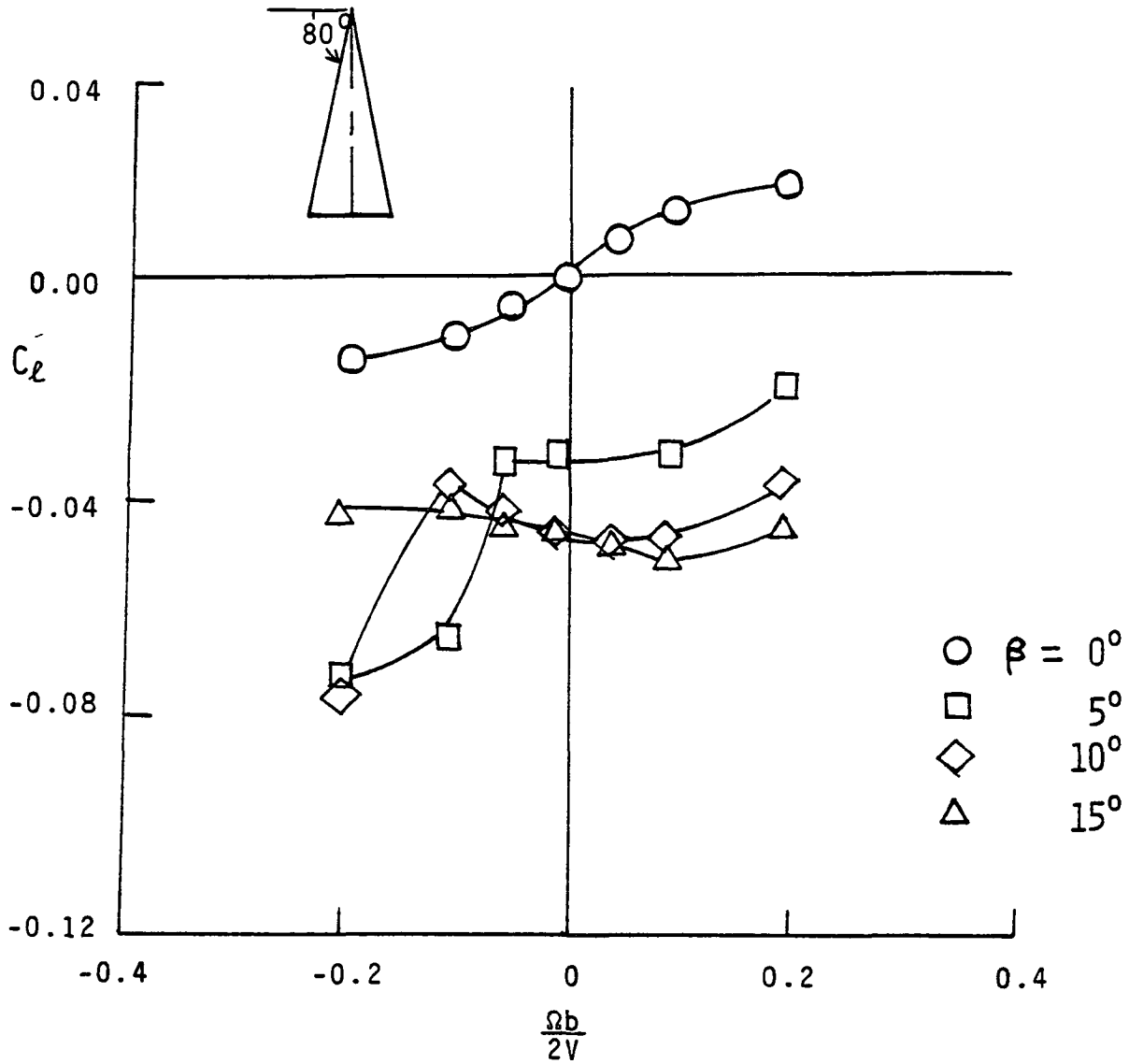

Figure 9. Rotary Data of an 80°-Delta Wing at α_s=30°(ref.8).

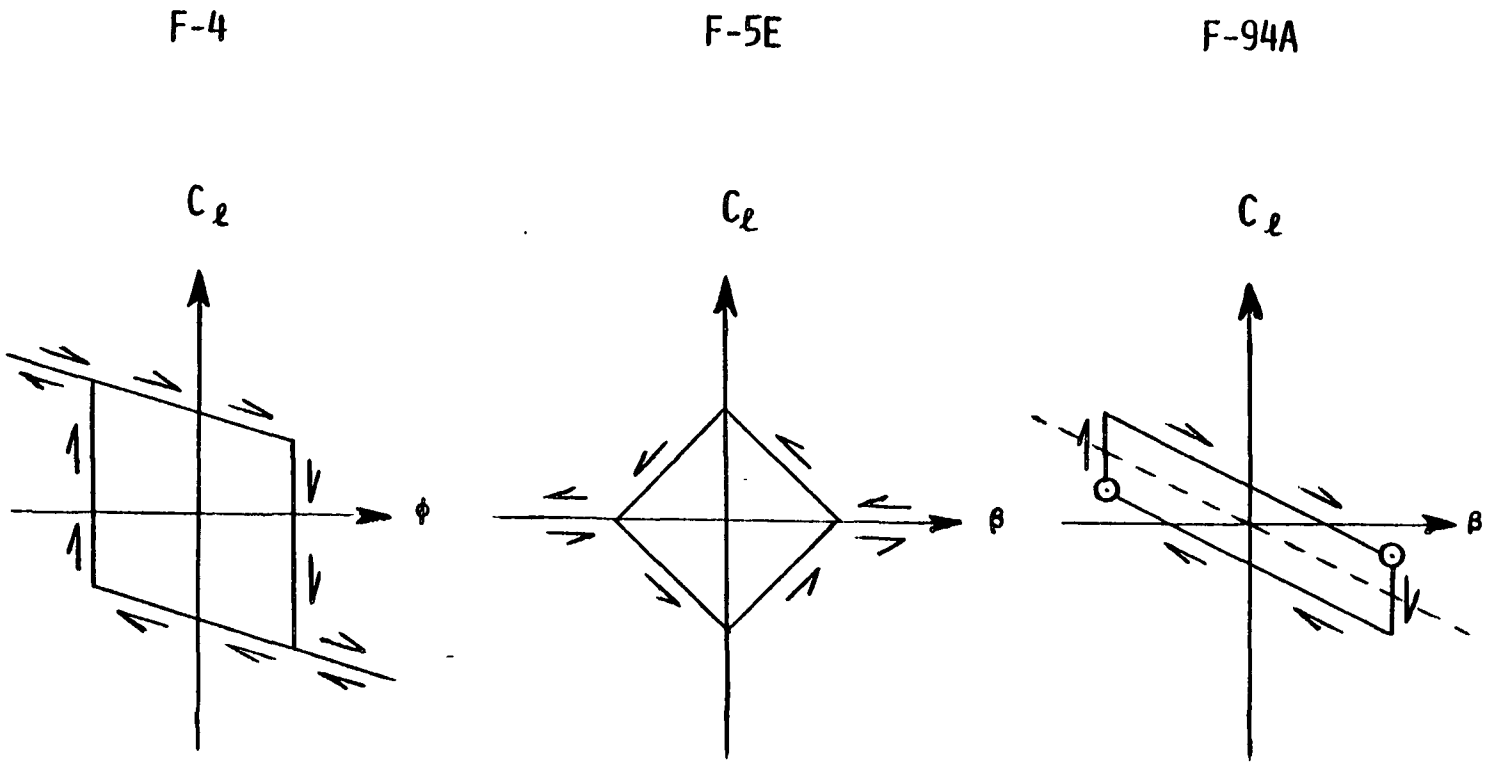

Figure 10. Rolling-Moment Hysteresis.

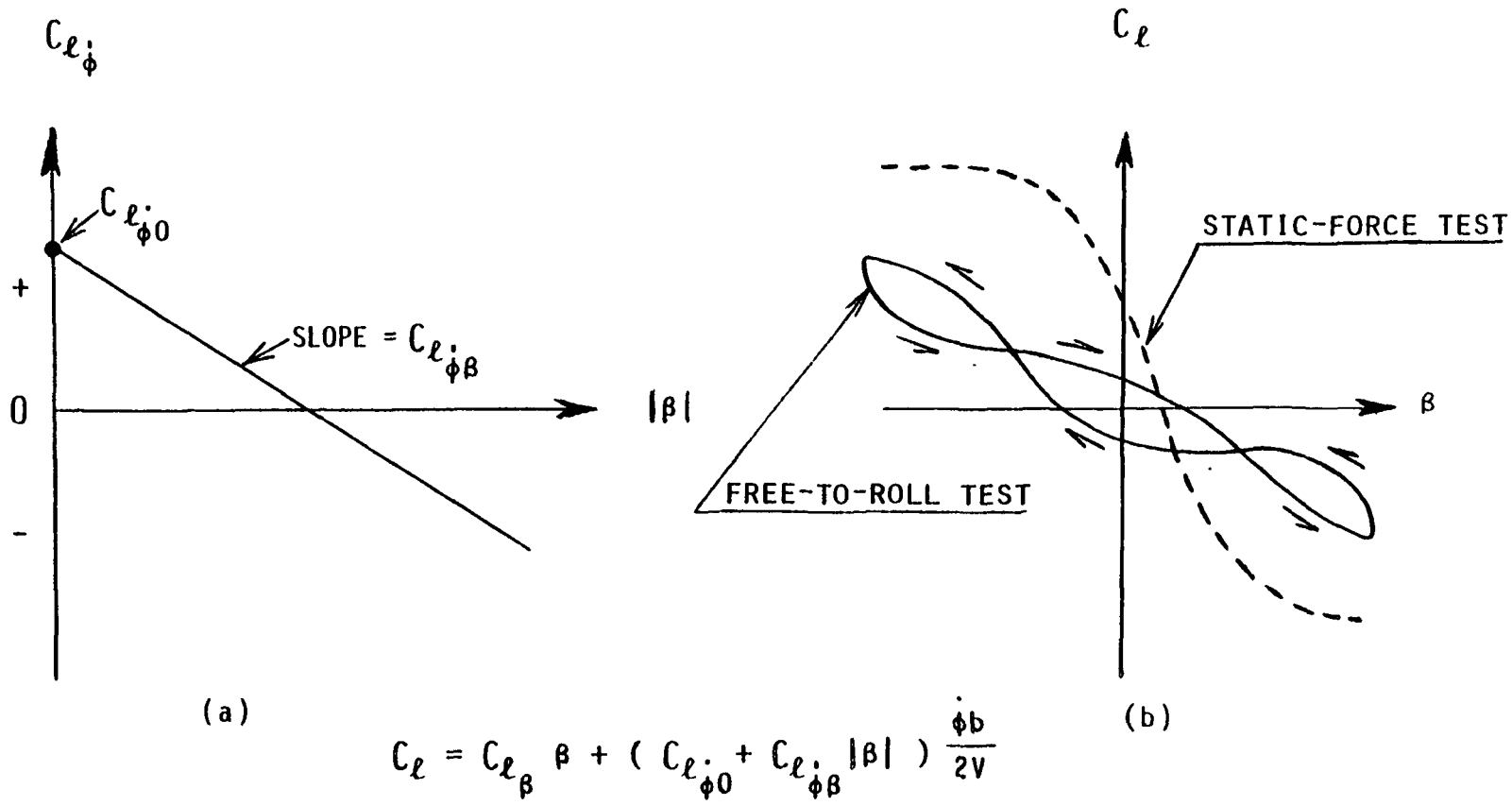

Figure 11. (a) Linear Variation of Roll Damping with Sideslip

(b) Rolling Moment versus Sideslip (ref. 8)

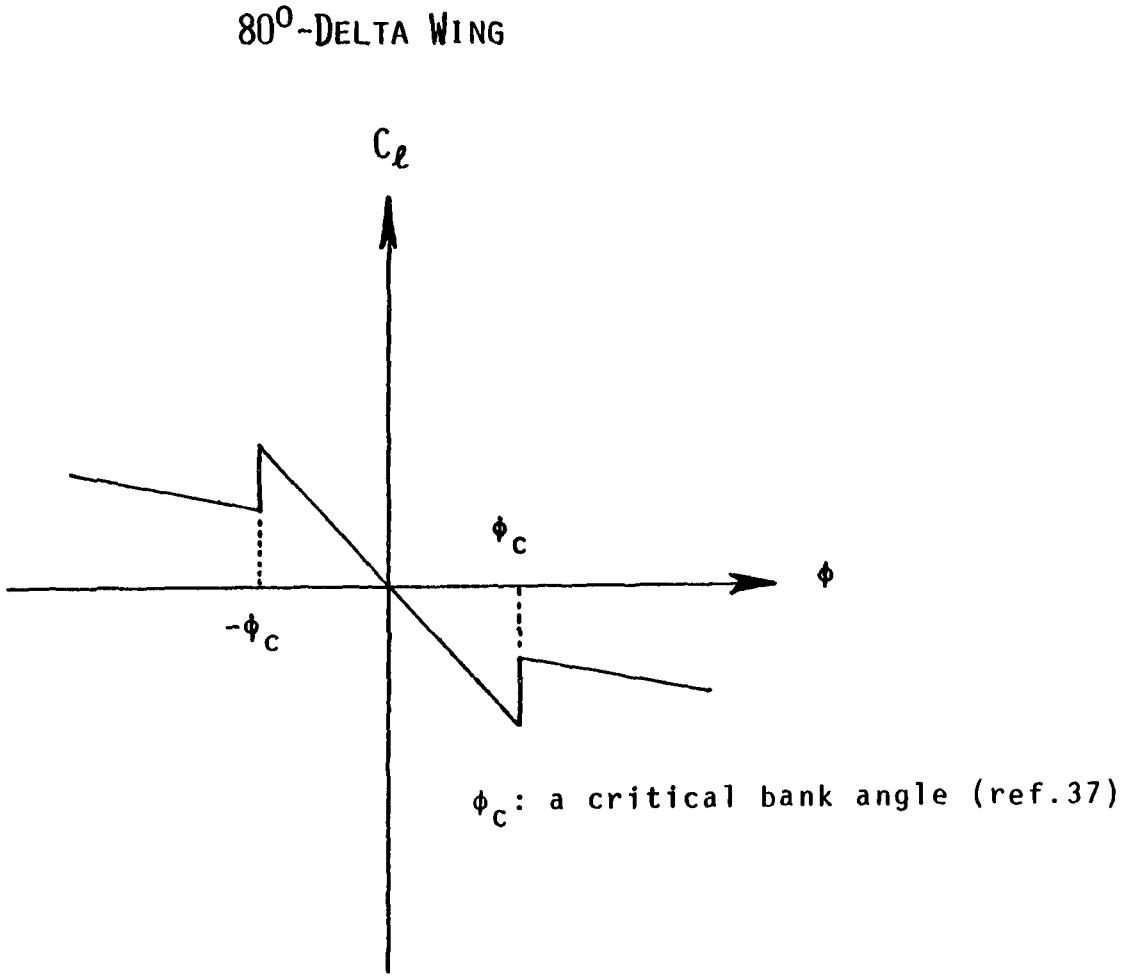

Figure 12. Discontinuous Aerodynamics with a Lumped-Time-Lag Concept (ref.37).

80^{o}-Delta Wing

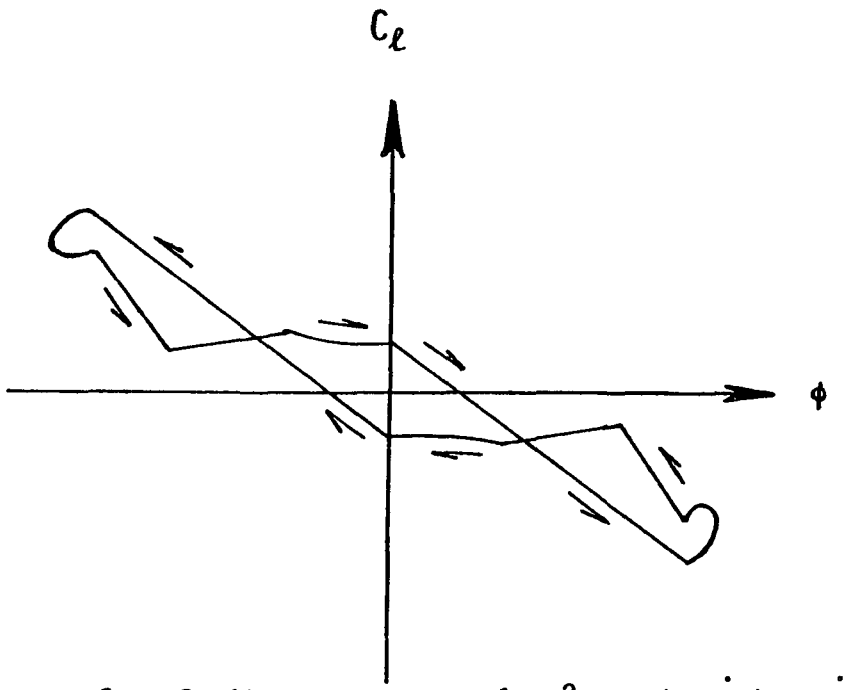

$$m\left(r^2 + d^2\right)\ddot{\phi} = mgd \sin\phi + \frac{1}{2}\rho V^2 \bar{c} S \cdot C_\ell(\phi, \dot{\phi}) - \mu\dot{\phi}$$

d : distance between the midchord and the axis of rotation for a free-to-roll test

μ : damping coefficient for the roll bearing of a free-to-roll test rig

Figure 13. Numerical Simulation of Wing Rock (ref.38).

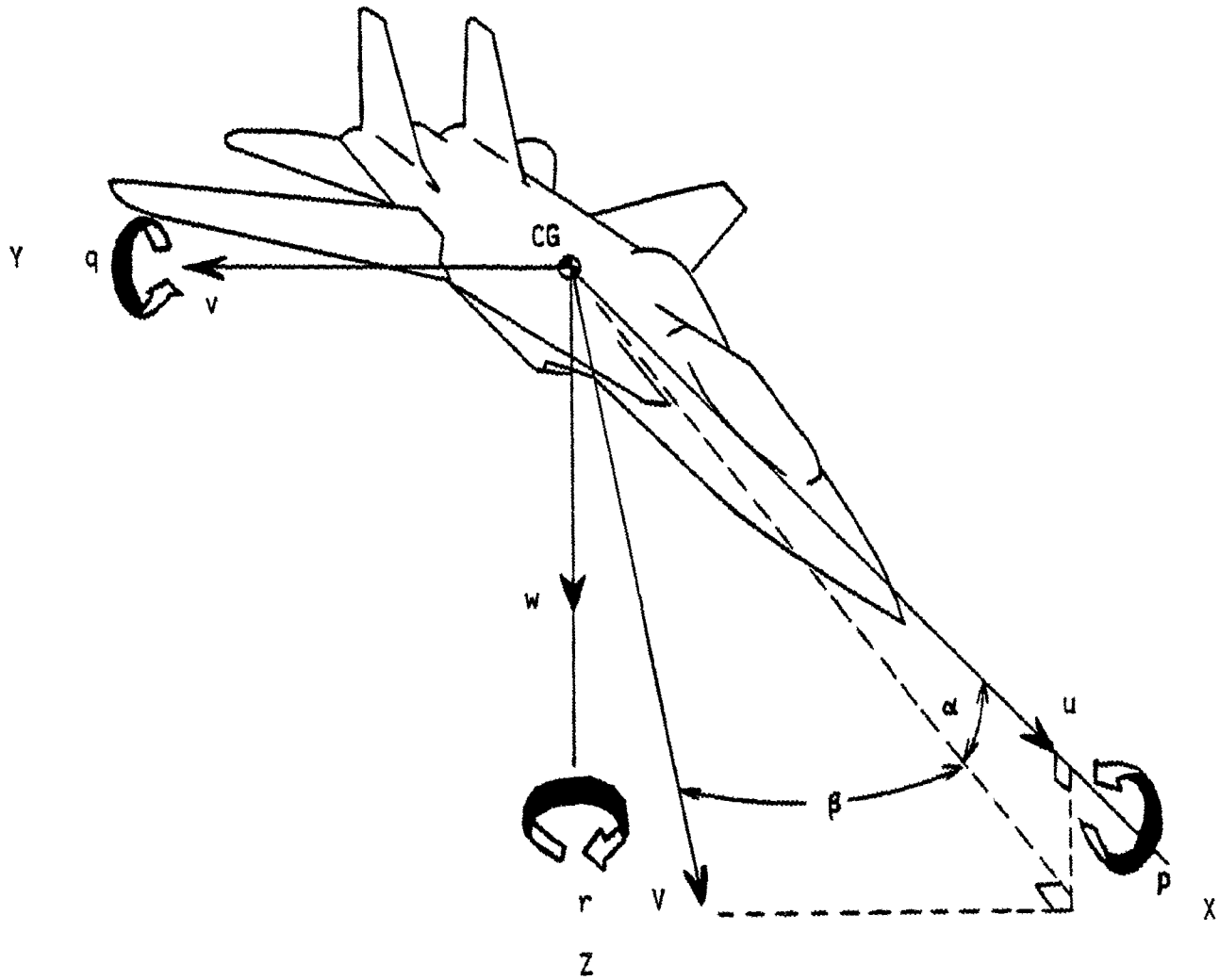

Figure 14.The Body System of Axes.

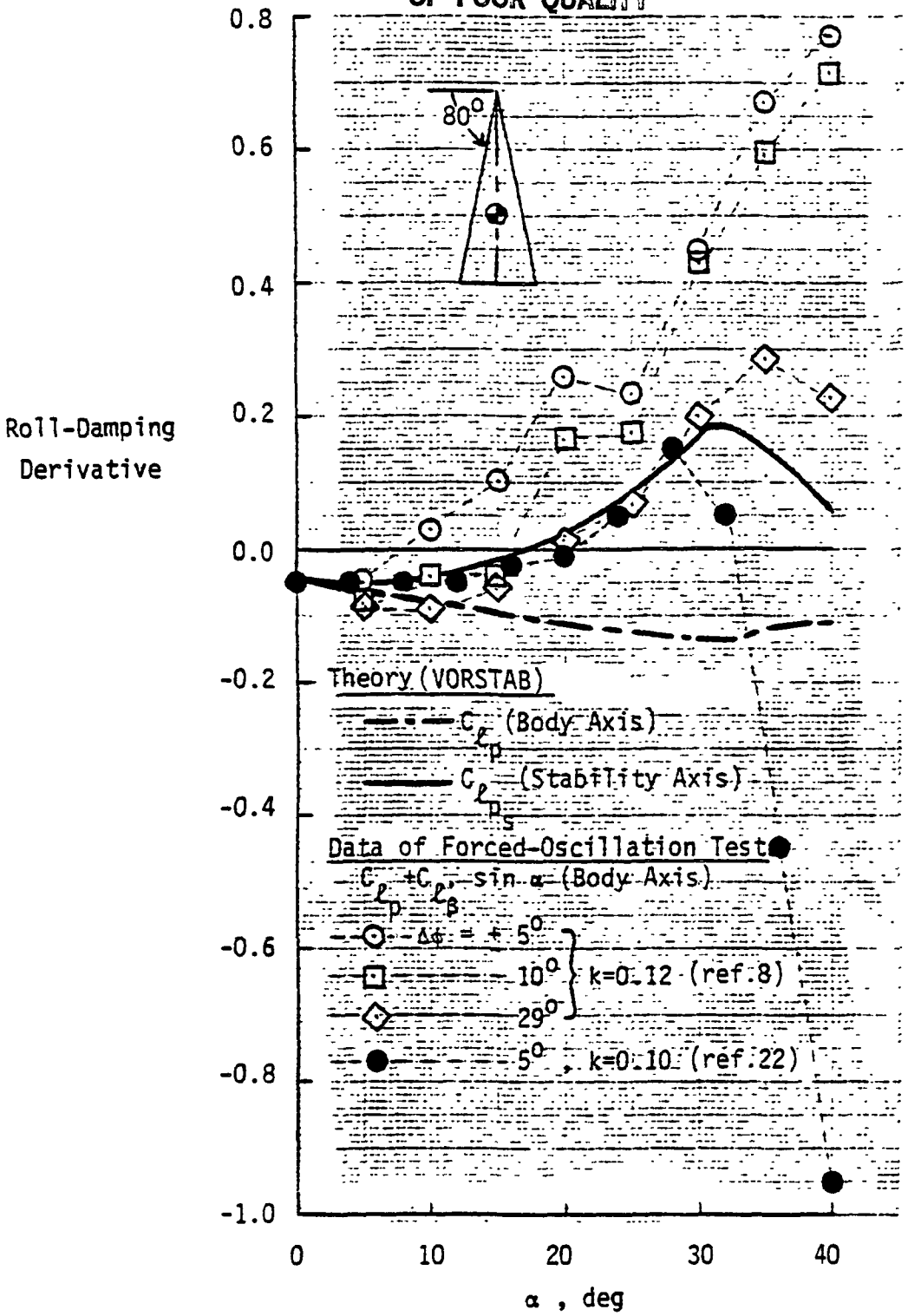

Figure 15.Damping-in-Roll Derivatives of a Delta Wing with 80-Degree Sweep (X_{CG}=0.4$\bar{c}$) at M_∞= 0.1.

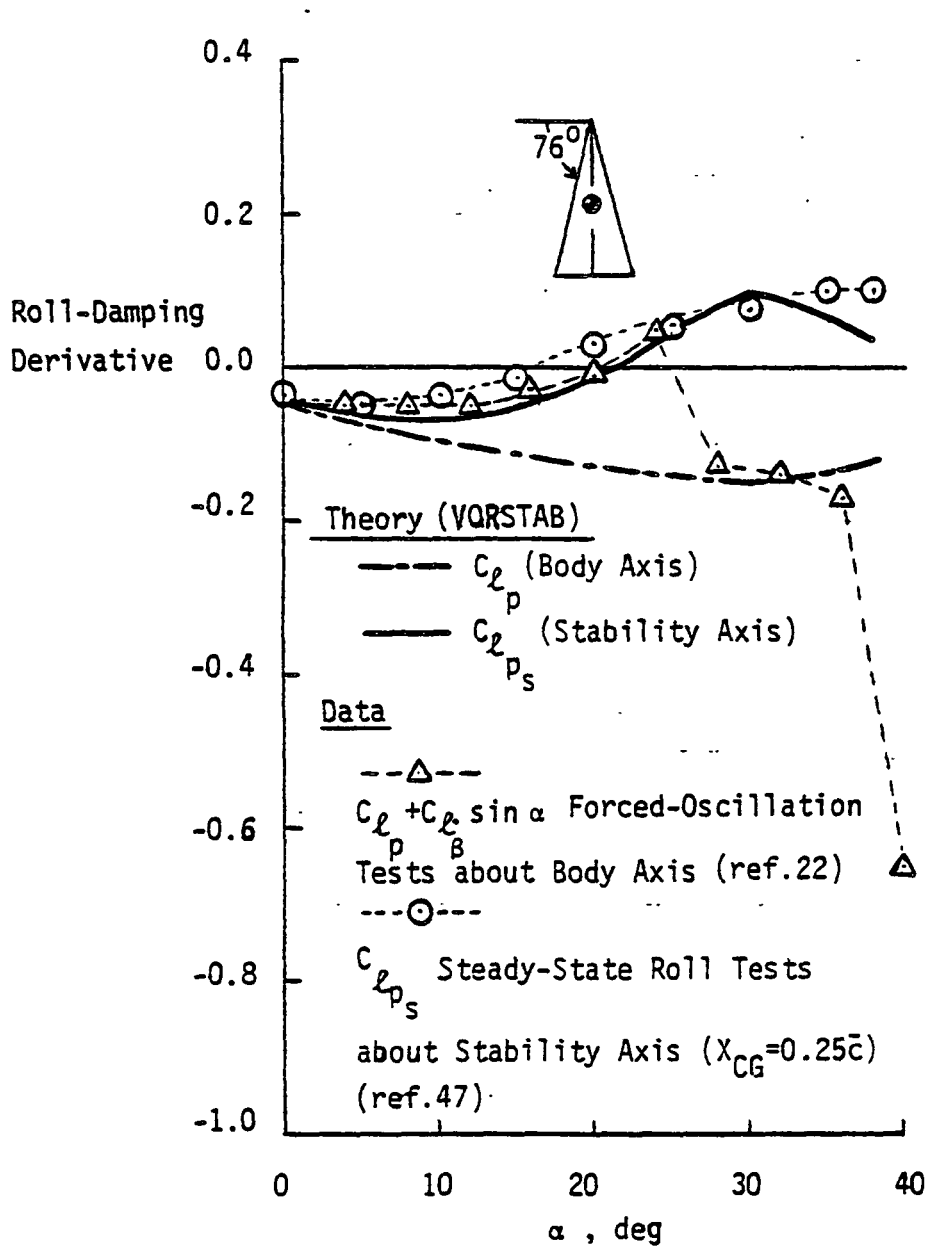

Figure 16. Damping-in-Roll Derivatives of a Delta Wing with 76-Degree Sweep ($X_{CG}=0.40\bar{c}$) at $M_\infty=0.1$.

C-2

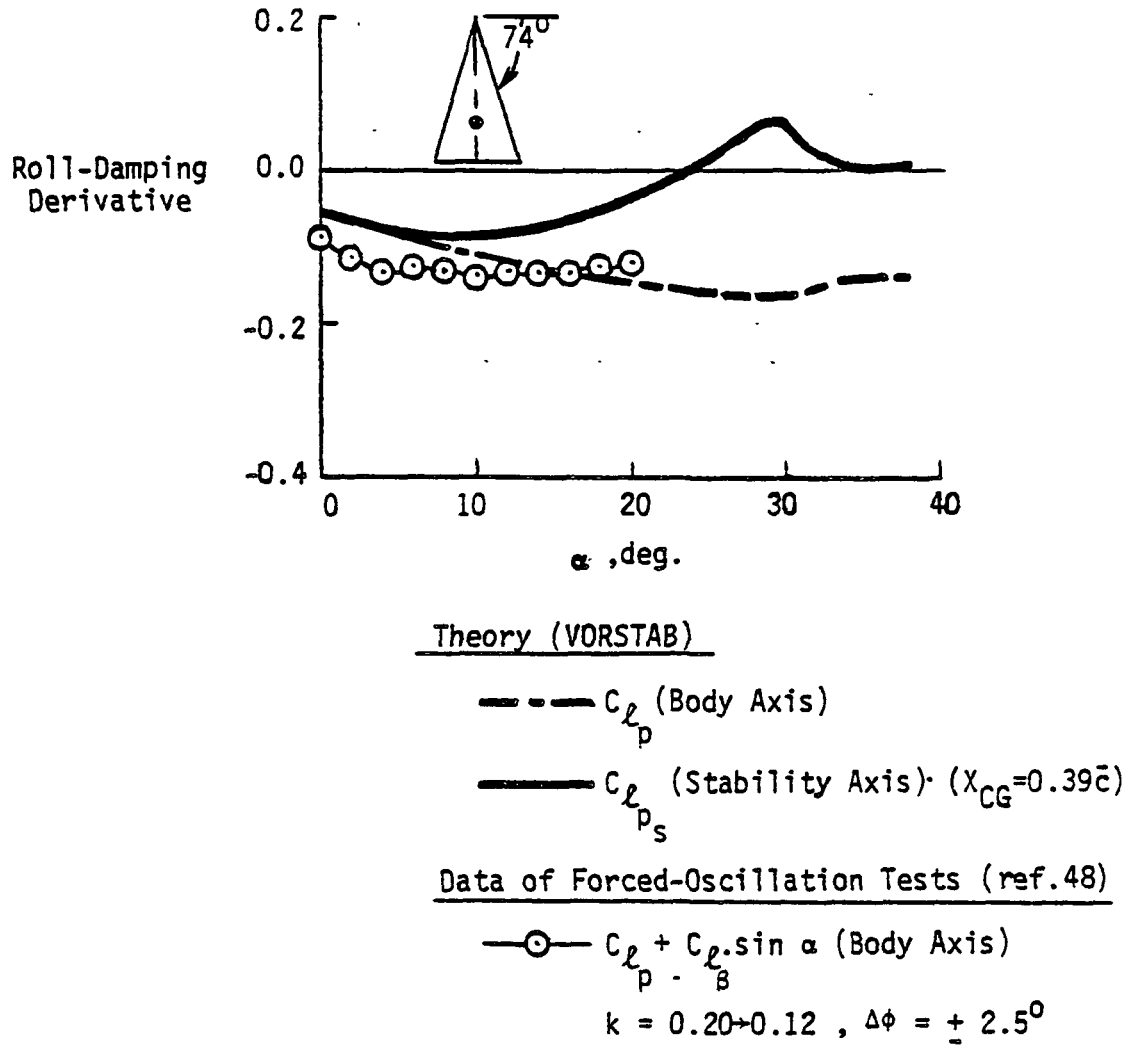

Figure 17. Damping-in-Roll Derivatives of a Delta Wing with 74-Degree Sweep at M_∞=0.2.

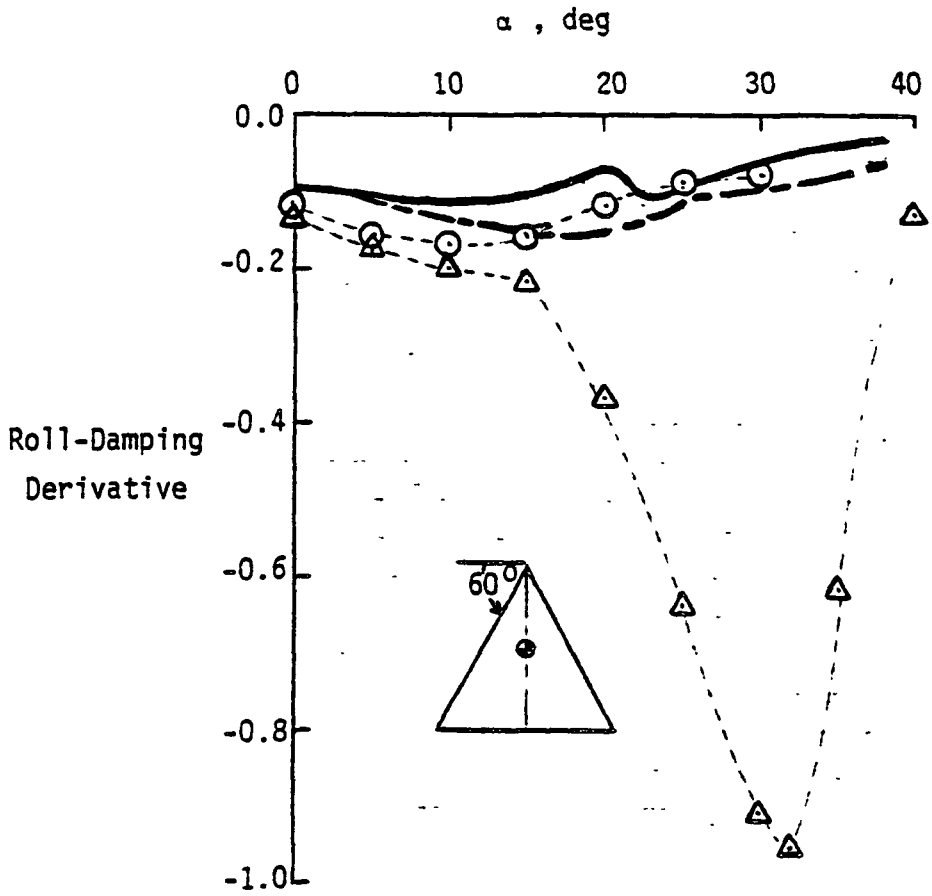

Theory (VORSTAB)

C_{ℓ_p} (Body Axis)

$C_{\ell_{p_s}}$ (Stability Axis) (X_{CG}=0.34$\bar{c}$)

Data of Free-to-Damp Oscillation Tests (ref. 49)

$C_{\ell_p} + C_{\ell_\beta} \sin \alpha$ (Body Axis)

$k = 0.13$, $\Delta\phi = \pm 30^\circ$

$C_{\ell_{p_s}}$ (Stability Axis) (X_{CG}=0.25$\bar{c}$)

$k = 0.14 \rightarrow 0.10$, $\Delta\phi = \pm 30^\circ$

Figure 18. Damping-in-Roll Derivatives of a Delta Wing with 60-Degree Sweep at M_∞=0.1.

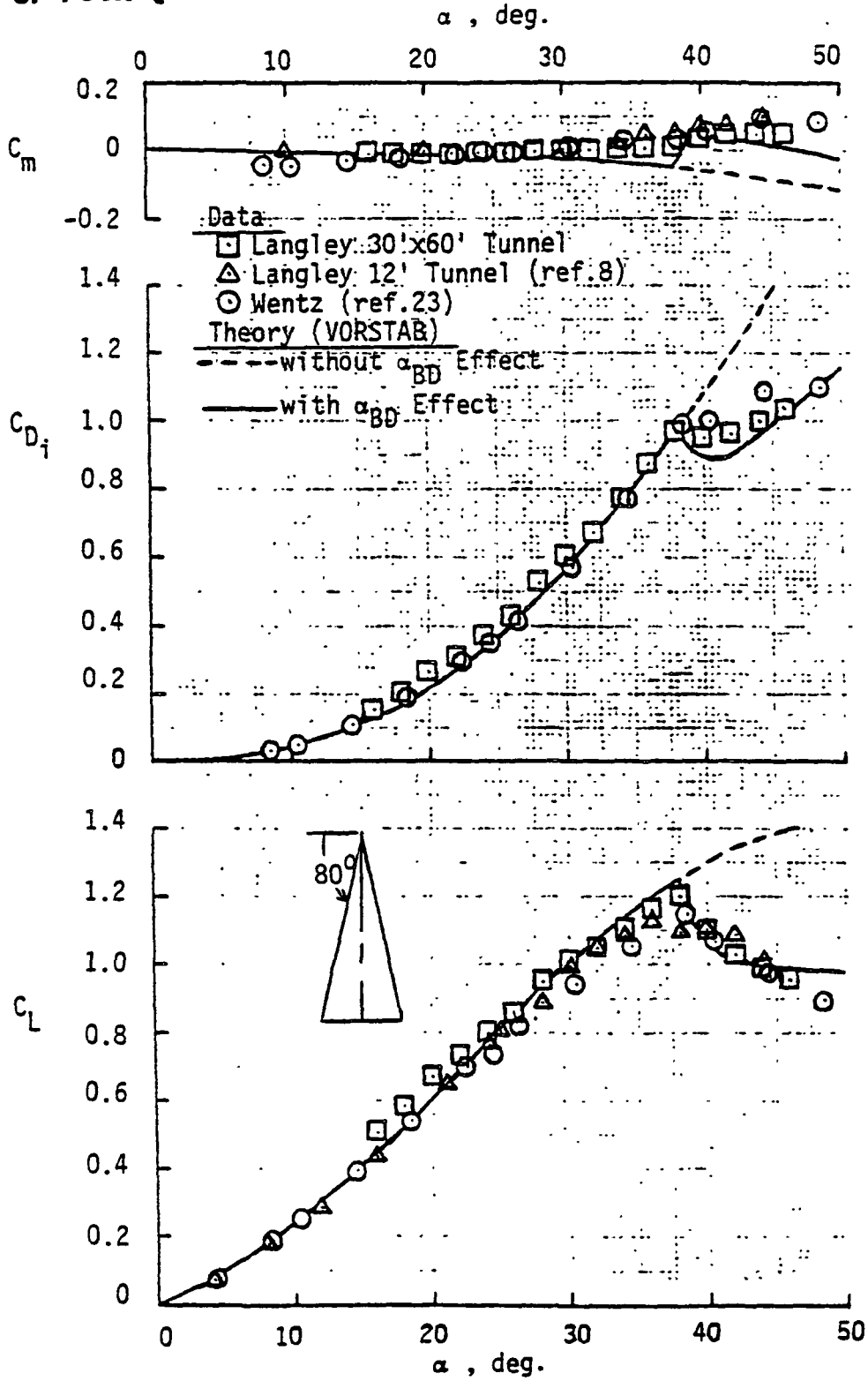

Figure 19. Longitudinal Aerodynamic Characteristics of a Delta Wing of AR=0.705 with Sharp Leading Edges at M_∞=0.1. X_{CG}=0.4$\bar{c}$; Re=1.4x10^6.

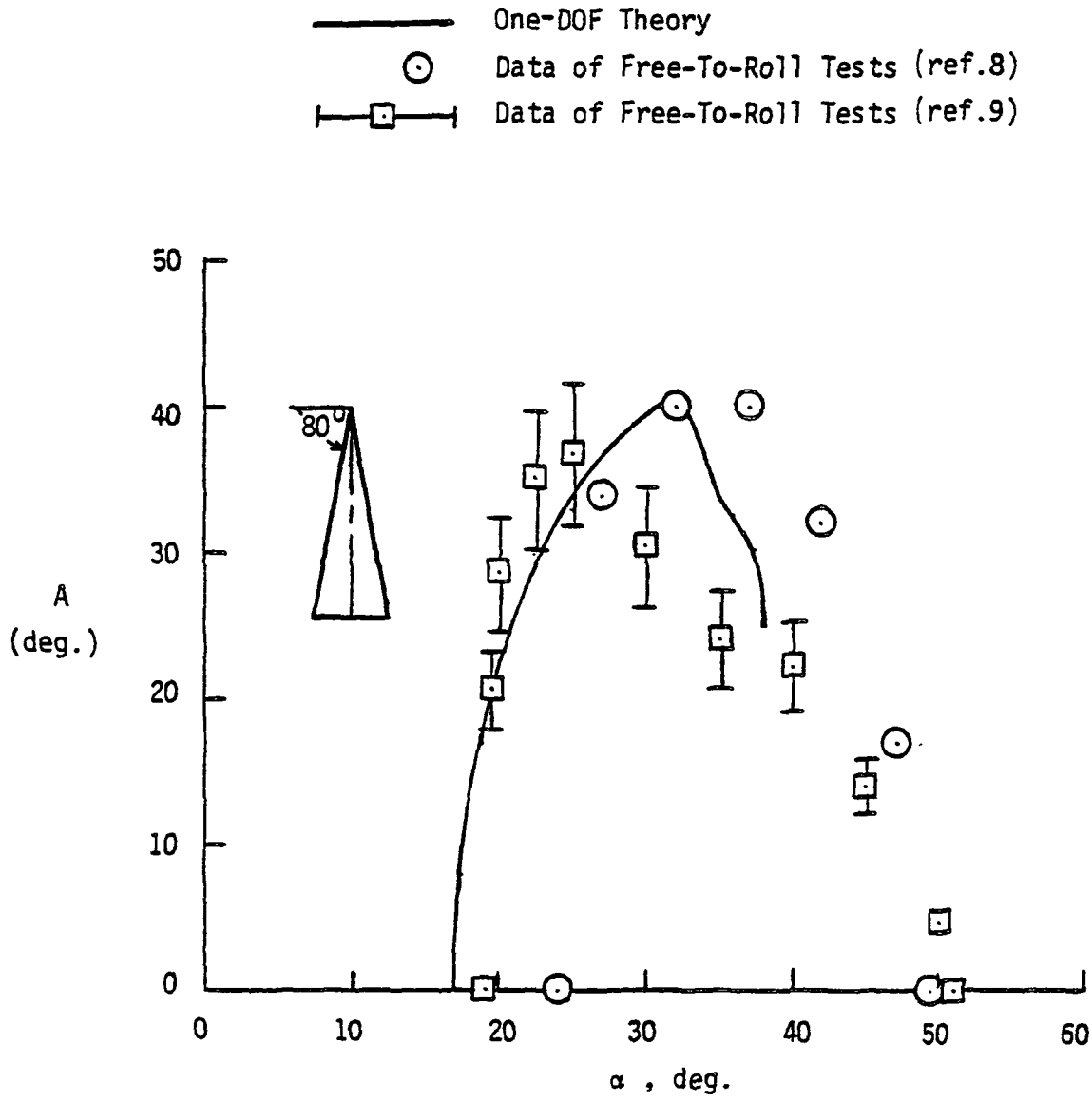

Figure 20.Steady-State Amplitudes of Wing Rock for a Delta Wing of 80-Degree Sweep (AR=0.71).

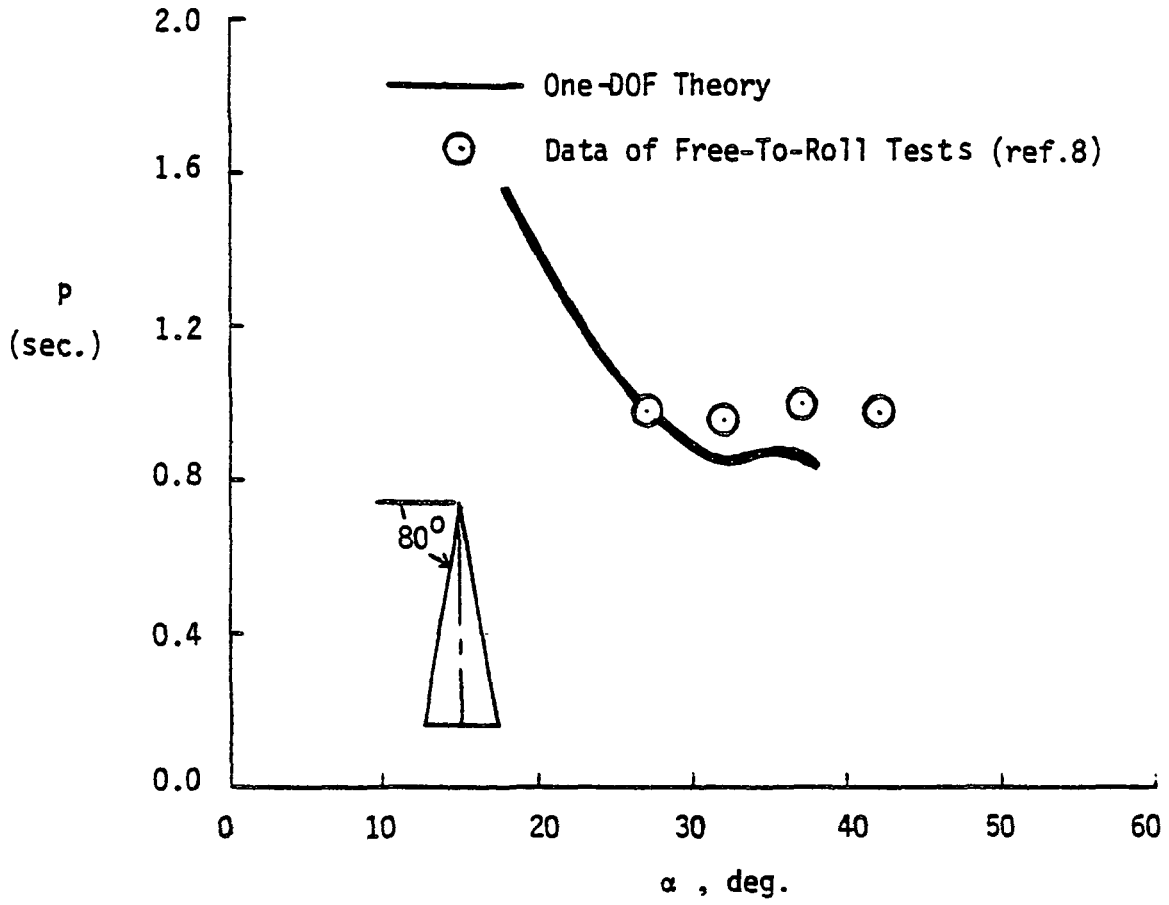

Figure 21. Steady-State Periods of Wing Rock for a Delta Wing of 80-Degree Sweep.

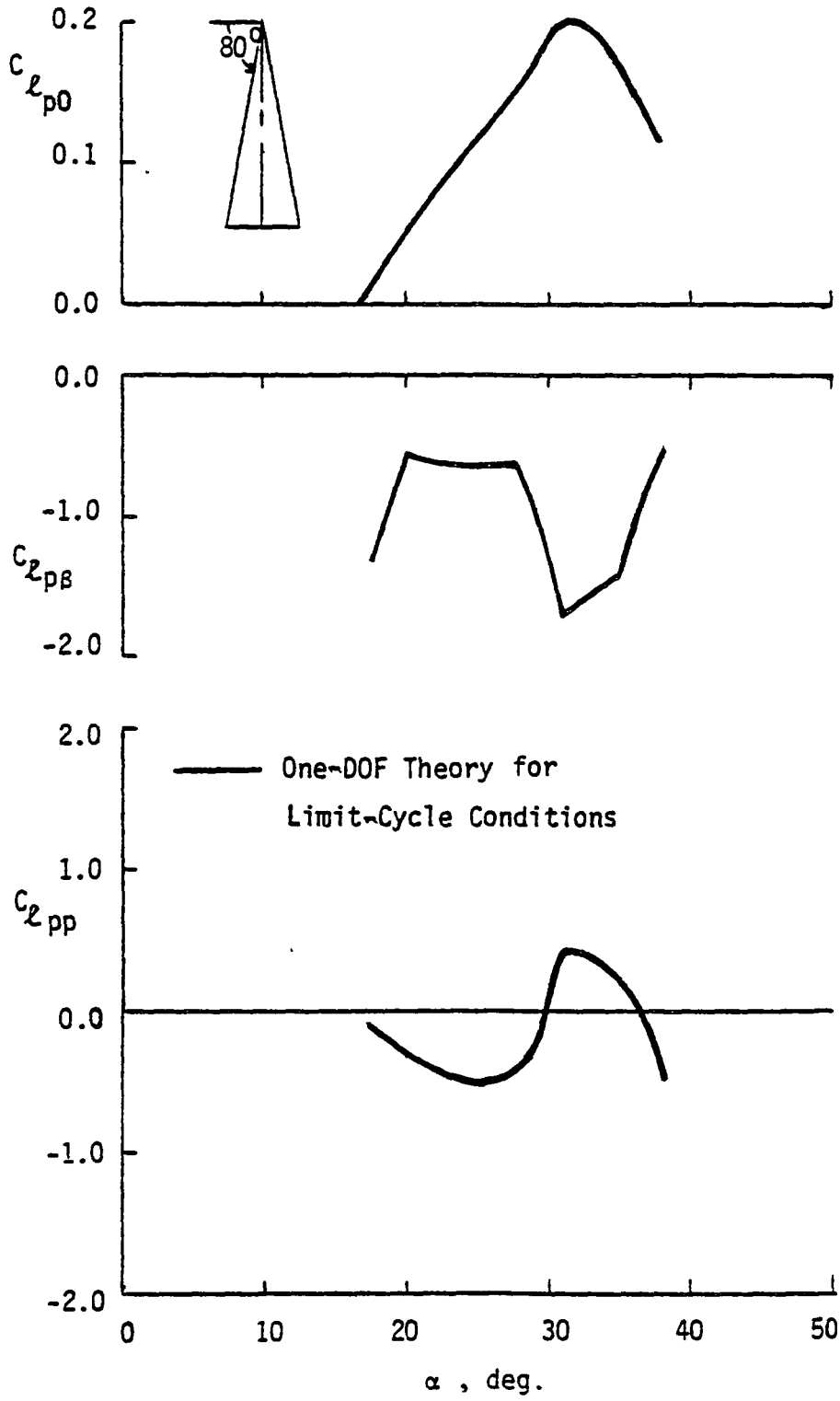

Figure 22. Theoretical Variations of $C_{\ell_{p0}}$ and $C_{\ell_{p\beta}}$ and $C_{\ell_{pp}}$ with Angle of Attack.

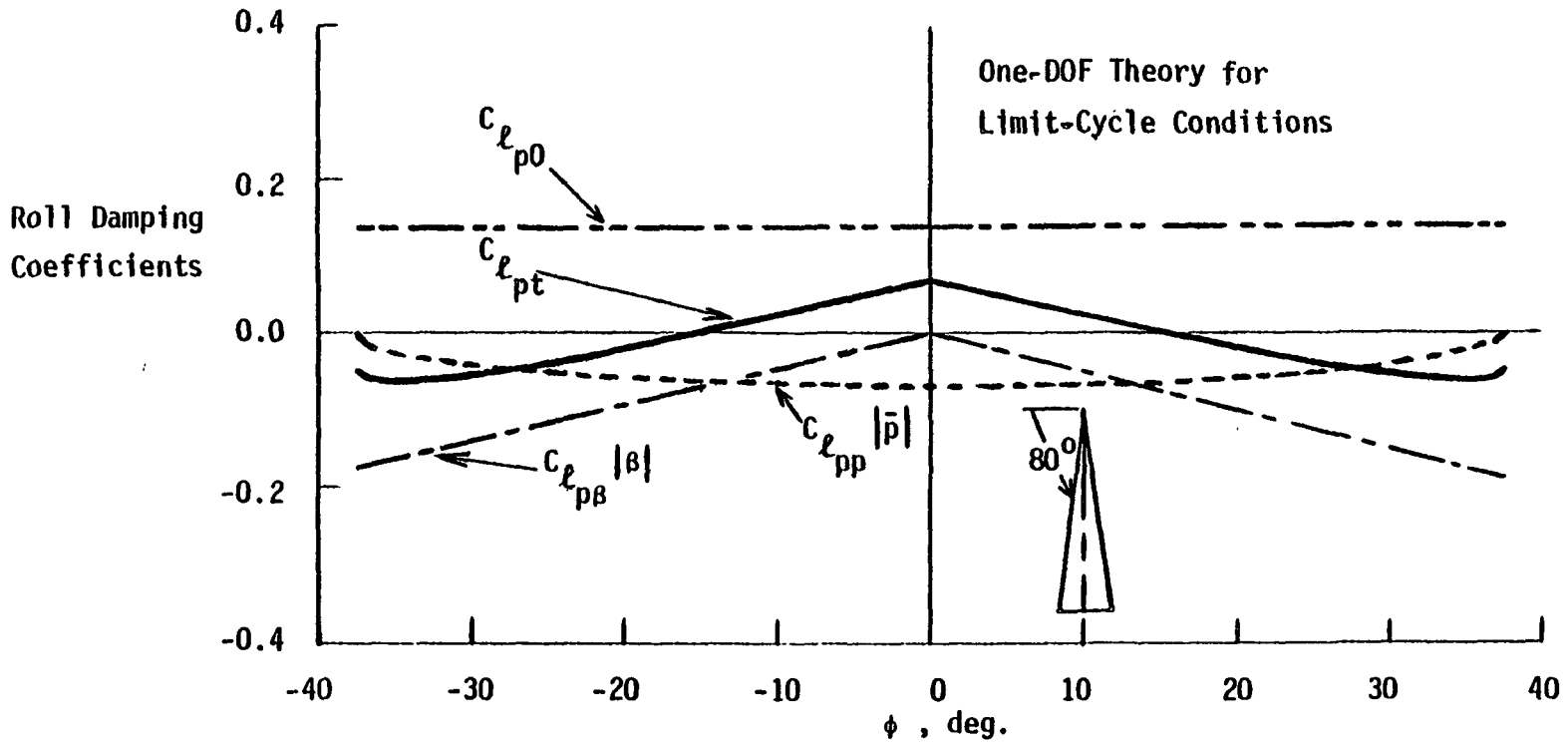

Figure 23. Nonlinear Roll Damping Coefficients for a Delta Wing of 80-Degree Sweep at $\alpha = 27^{o}$.

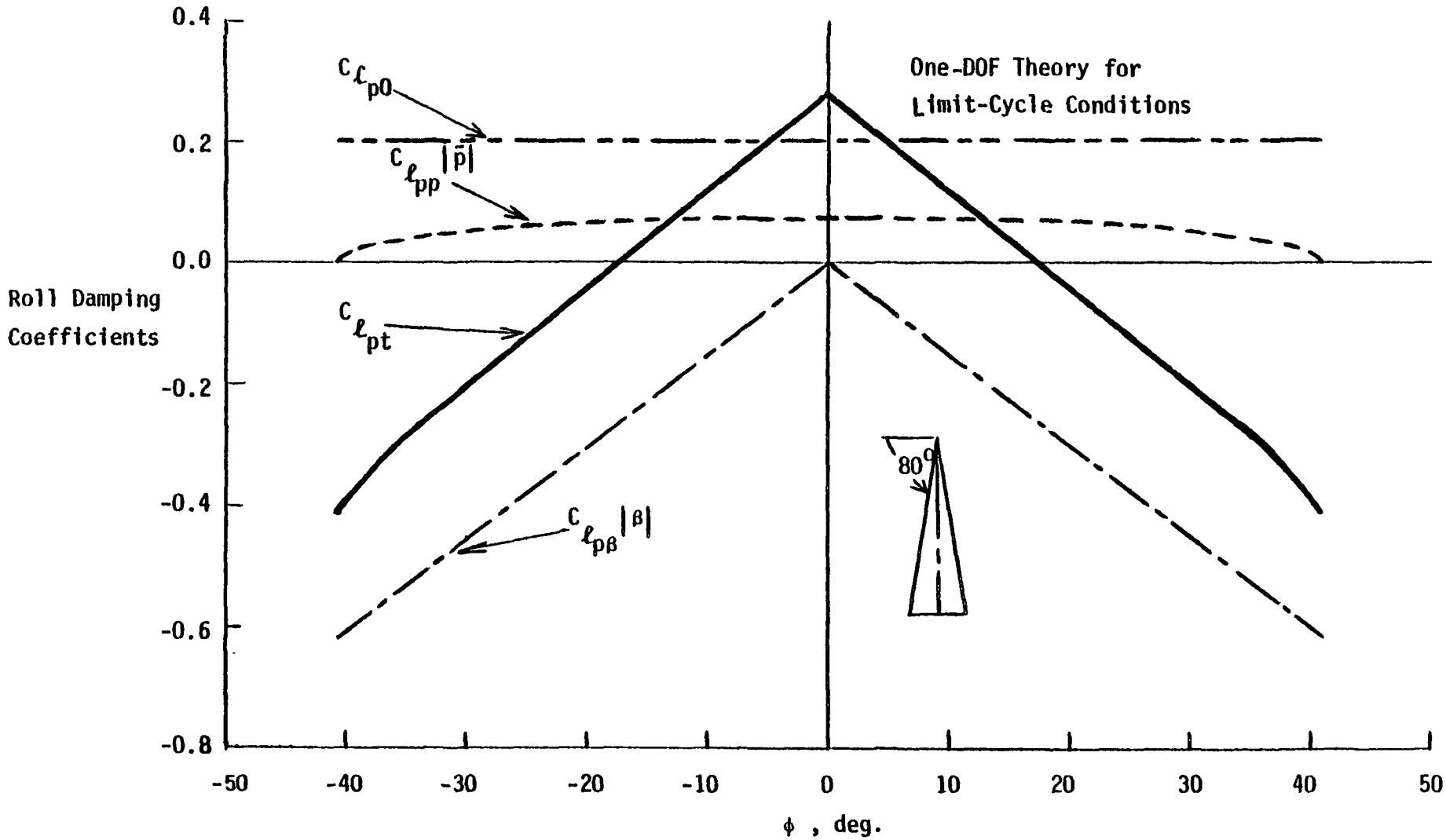

Figure 24. Nonlinear Roll Damping Coefficients for a Delta Wing of 80-Degree Sweep at $\alpha = 32^{o}$.

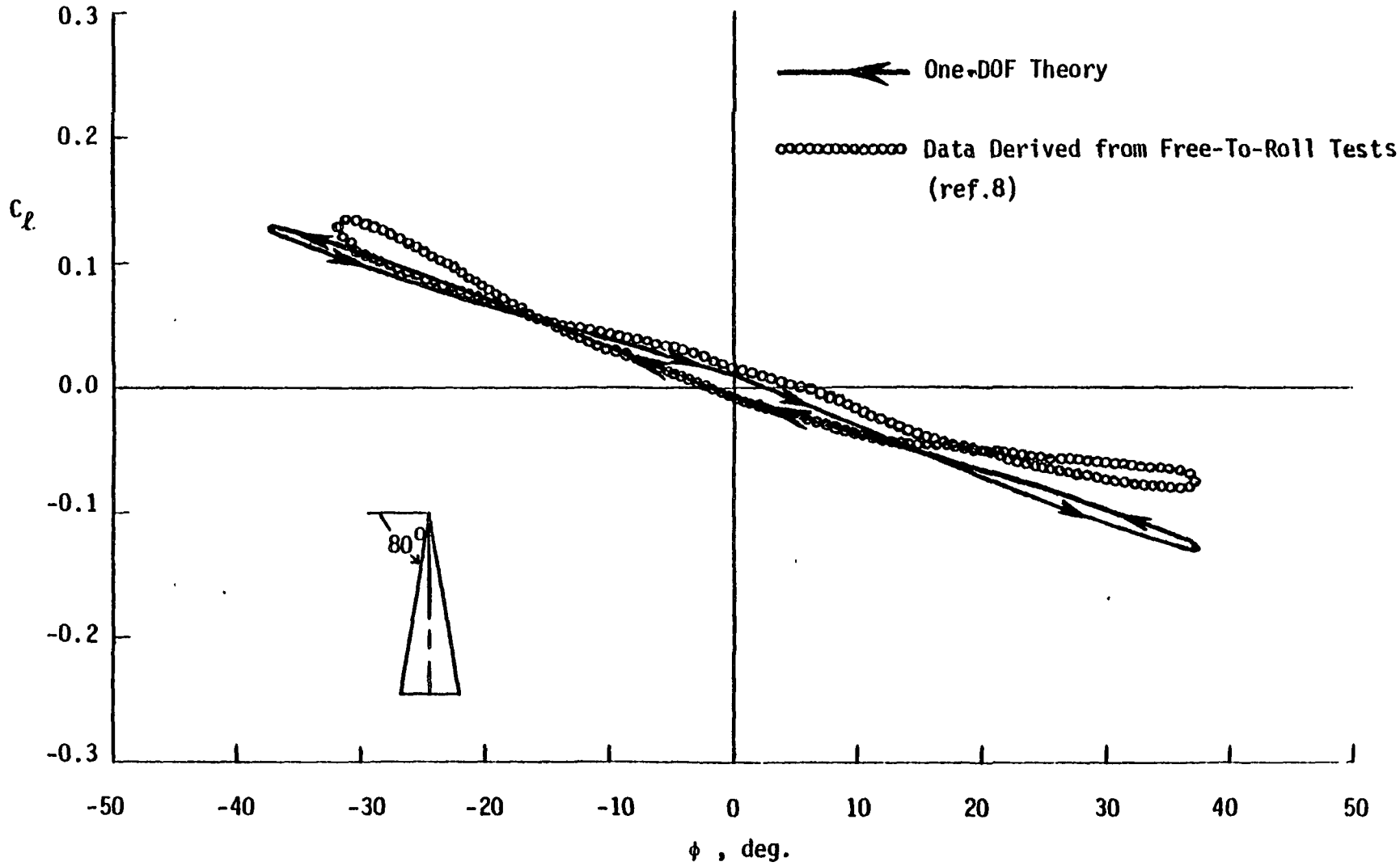

Figure 25.The Histogram of the Total Aerodynamic Rolling Moment Coefficient versus Bank Angle for One Limit Cycle of Wing Rock at Angle of Attack of 27 Degrees.

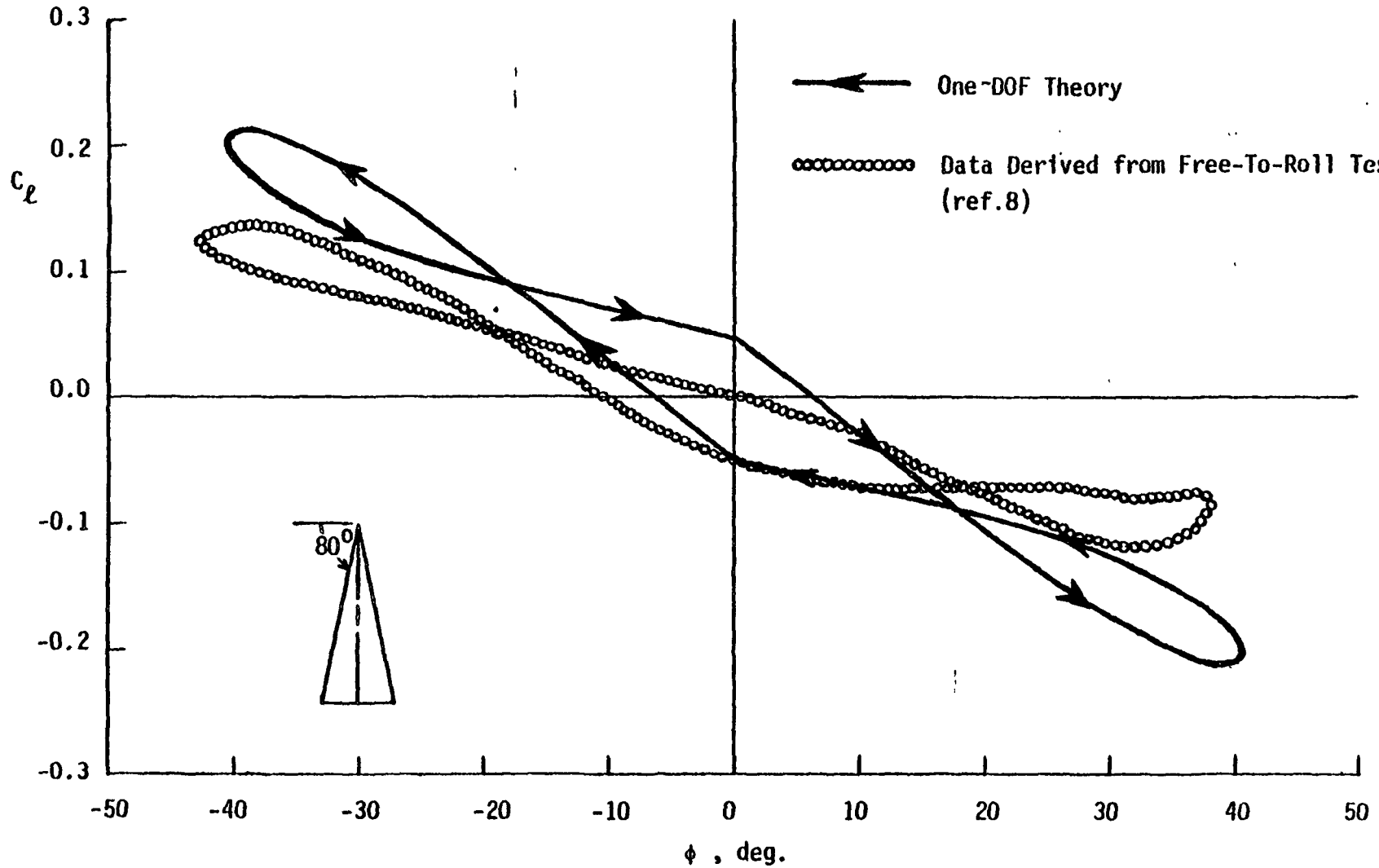

Figure 26. The Histogram of the Total Aerodynamic Rolling Moment Coefficient versus Bank Angle for One Limit Cycle of Wing Rock at Angle of Attack of 32 Degrees.

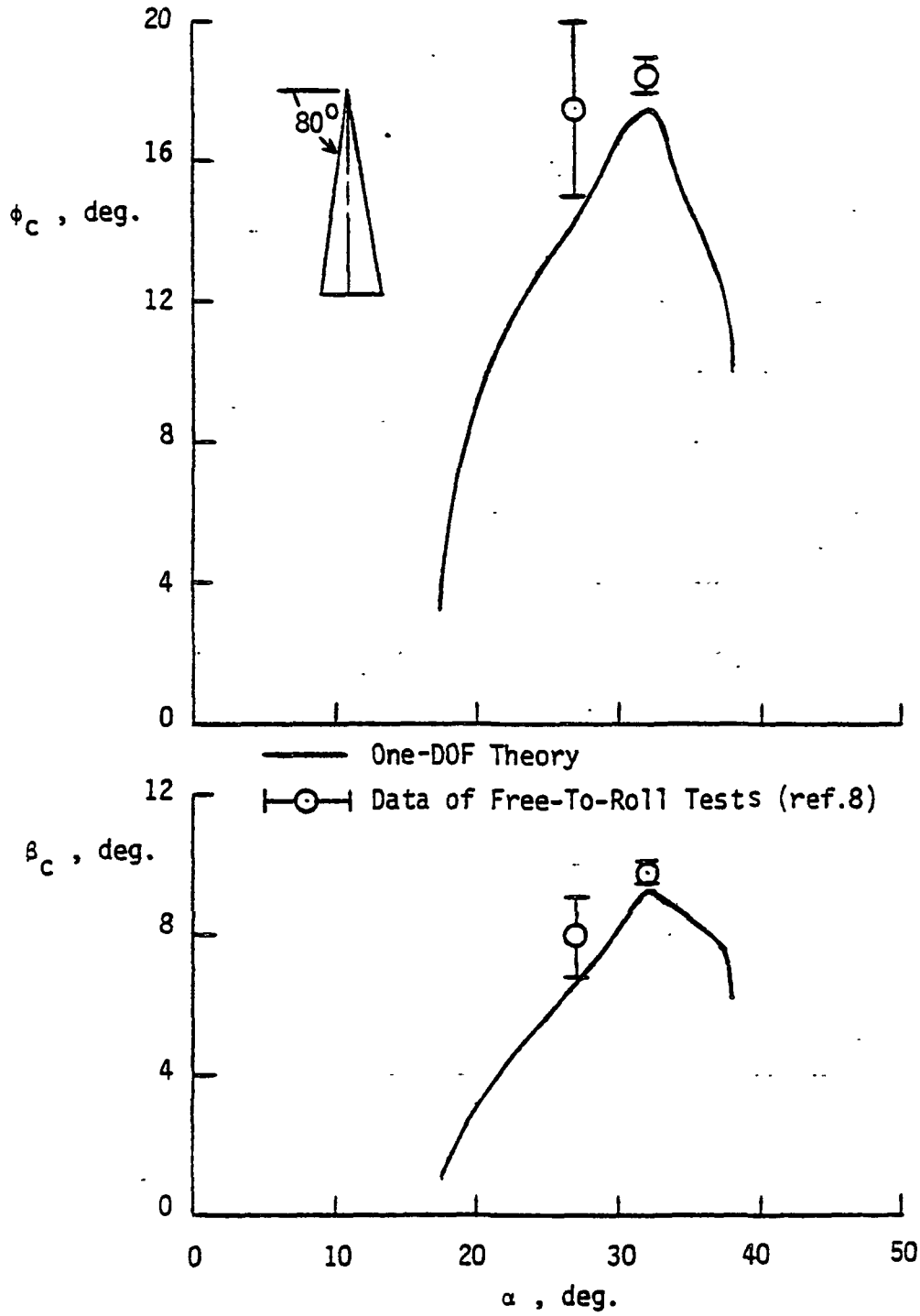

Figure 27.The Critical Bank and Sideslip Angles for a Delta Wing of 80-Degree Sweep during Steady-State Wing Rock.

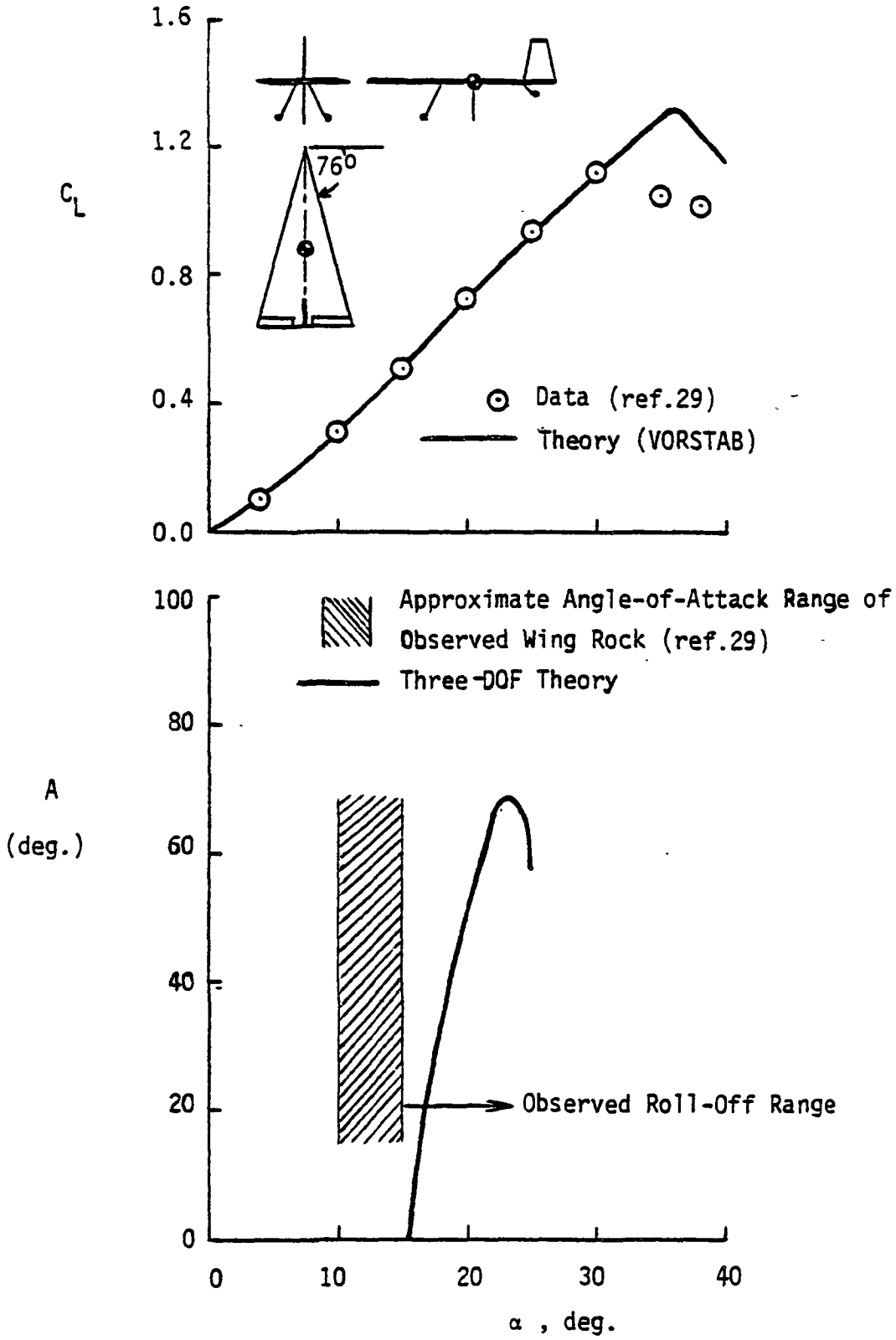

Figure 28. Lift Coefficient (Data Obtained at Re=696,000) and Steady-State Amplitude of Wing Rock for a Delta Wing (AR=1.0) with a Vertical Tail at M_∞=0.1. X_{CG}=0.30$\bar{c}$.

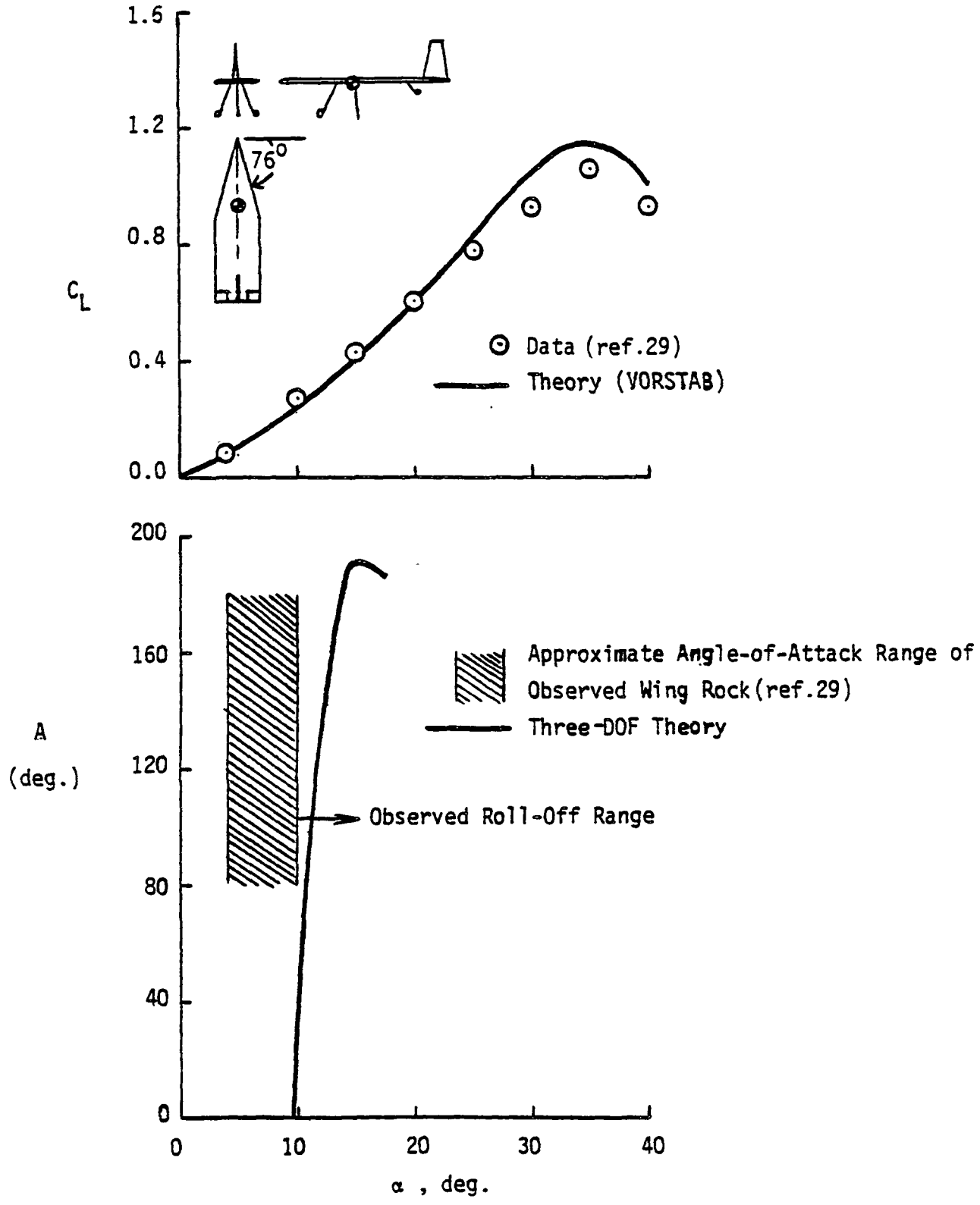

Figure 29. Lift Coefficient (Data Obtained at Re=812,000) and Steady-State Amplitude of Wing Rock for a Cropped Delta Wing of 76-Degree Sweep (AR=0.33)with a Vertical Tail at M_∞=0.1. X_{CG}=0.27$\bar{c}$.

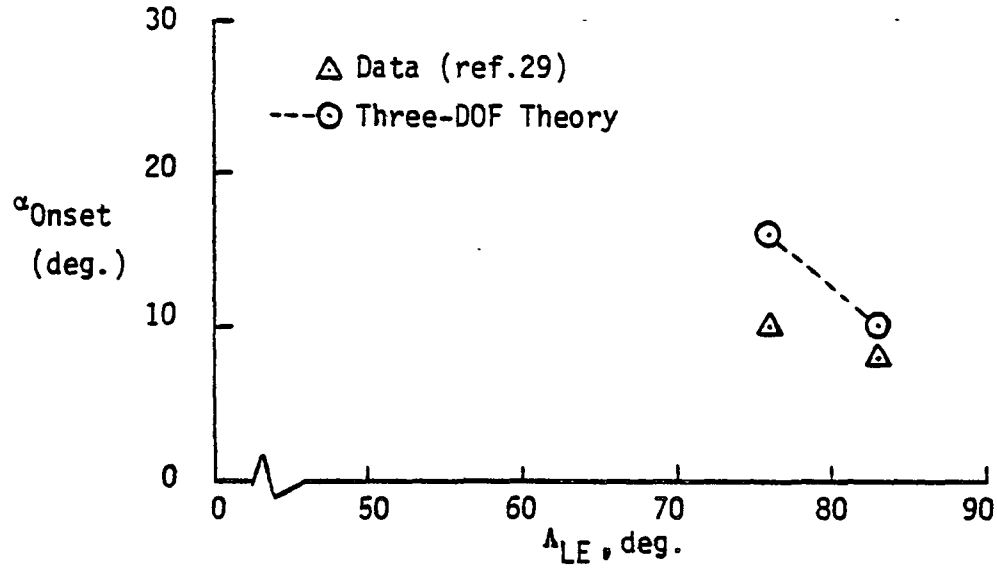

(a) Delta Wing with a Vertical Tail. $S_t/S=0.10$.

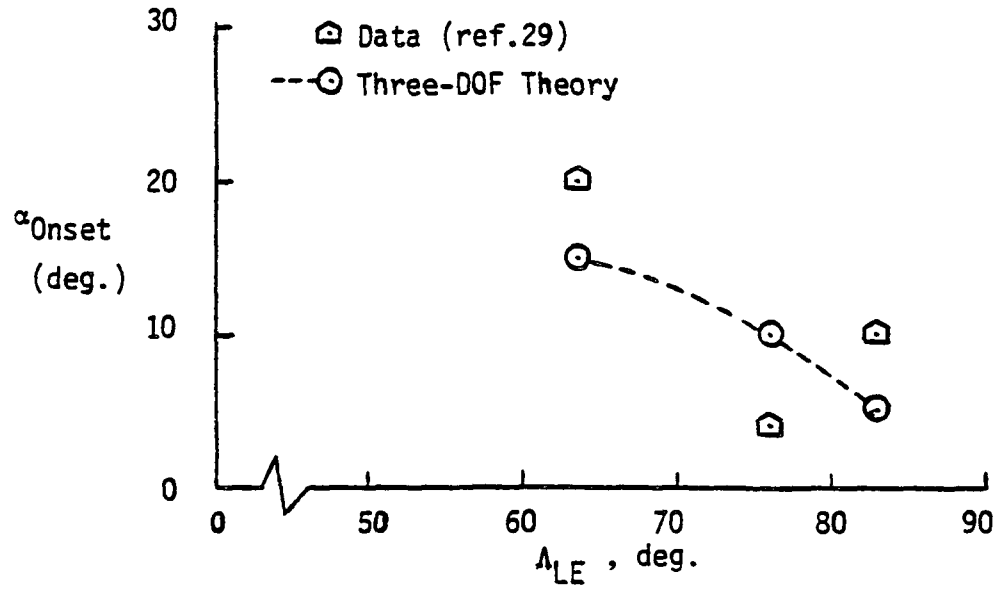

(b) Cropped Delta Wing with a Vertical Tail. $S_t/S=0.134$.

Figure 30. Comparison of the Onset α with Data at $M_\infty=0.1$. Moment-Center Location is at Forward Gravity-Center Position.